

MEASUREMENT OF LEADING AND TRAILING EDGE VORTEX
SHEDDING MECHANISM FOR FLAPPING AIRFOIL IN HOVER USING
PARTICLE IMAGE VELOCIMETRY TECHNIQUE

A THESIS SUBMITTED TO
THE GRADUATE SCHOOL OF NATURAL AND APPLIED SCIENCES
OF
MIDDLE EAST TECHNICAL UNIVERSITY

BY

AYBÜGE ÇEKİNMEZ

IN PARTIAL FULFILLMENT OF THE REQUIREMENTS
FOR
THE DEGREE OF MASTER OF SCIENCE
IN
AEROSPACE ENGINEERING

SEPTEMBER, 2013

Approval of the thesis:

**MEASUREMENT OF LEADING AND TRAILING EDGE VORTEX
SHEDDING MECHANISM FOR FLAPPING AIRFOIL IN HOVER USING
PARTICLE IMAGE VELOCIMETRY TECHNIQUE**

Submitted by **AYBÜGE ÇEKİNMEZ** in partial fulfillment of the requirements for
the degree of **Master of Science in Aerospace Engineering Department, Middle
East Technical University** by,

Prof. Dr. Canan Özgen
Dean, Graduate School of **Natural and Applied Sciences**

Prof. Dr. Ozan Tekinalp
Head of Department, **Aerospace Engineering**

Prof. Dr. Nafiz Alemdaroğlu
Supervisor, **Aerospace Engineering Dept., METU**

Examining Committee Members:

Prof. Dr. Serkan Özgen
Aerospace Engineering Dept., METU

Prof. Dr. Nafiz Alemdaroğlu
Aerospace Engineering Dept., METU

Prof. Dr. Yusuf Özyörük
Aerospace Engineering Dept., METU

Prof. Dr. Altan Kayran
Aerospace Engineering Dept., METU

Prof. Dr. Kahraman Albayrak
Mechanical Engineering Dept., METU

Date: _____04.09.2013_____

I hereby declare that all information in this document has been obtained and presented in accordance with academic rules and ethical conduct. I also declare that, as required by these rules and conduct, I have fully cited and referenced all material and results that are not original to this work.

Name, Surname: AYBÜGE ÇEKİNMEZ

Signature:

ABSTRACT

MEASUREMENT OF LEADING AND TRAILING EDGE VORTEX SHEDDING MECHANISM FOR FLAPPING AIRFOIL IN HOVER USING PARTICLE IMAGE VELOCIMETRY TECHNIQUE

ÇEKİNMEZ, Aybüge

M.Sc., Department of Aerospace Engineering

Supervisor: Prof Dr. Nafiz ALEMDAROĞLU

September 2013, 95 Pages

In this thesis, the vortex shedding formation/mechanism for flapping airfoil making the figure of eight motion in hover is investigated experimentally using Particle Image Velocimetry (PIV) technique and numerically for some parameters determined. For this investigation, a new flapping mechanism is designed and implemented to the existing water tank, where the airfoil is traversed laterally, such that the motion depicts a figure of eight. The traversing system is moved both in x (horizontal) and y (vertical) directions such that the figure of eight is drawn. This is the type of flapping motion for some of the birds in nature. The amplitude and the frequency of oscillations can easily be adjusted. The PIV technique is used to put into evidence the vortex shedding mechanism from the leading and trailing edges of the airfoil. Experiments are performed to investigate the effects of the parameters which are the amplitude of the figure of eight flapping motion, initial angle of attack, and the shape of the airfoil. From these experiments, the unsteady behavior of the vortices shed from the airfoil is analyzed and their effect on the generation of lift and drag is investigated. Also, the numerical study performed for the some parameters in present and previously done by Başkan [10] is supported and completed by this experimental study.

Keywords: Flapping motion, Particle Image Velocimetry (PIV)

ÖZ

HAVADA ASILI KONUMDAKİ ÇIRPAN KANAT HAREKETİNİN GİRDAP OLUŞUM MEKANİZMASININ PARÇACIK GÖRÜNTÜLEMELİ HIZ ÖLÇÜM TEKNİĞİ İLE İNCELENMESİ

ÇEKİNMEZ, Aybüge

Yüksek Lisans, Havacılık ve Uzay Mühendisliği Bölümü

Tez Yöneticisi: Prof Dr. Nafiz ALEMDAROĞLU

Eylül 2013, 95 Sayfa

Bu tezde, havada asılı durumda kalan ve sekiz şekli çizen çirpan kanat hareketinin girdap oluşum mekanizmaları; deneysel olarak, Parçacık Görüntülemeli Hız Ölçüm (PGHÖ) tekniği ile, ve belirlenen bazı parametreler için numerik olarak incelenmiştir. İlgili inceleme için, kanatın yanal hareketini sağlayıp sekiz çizebilen yeni bir kanat çarpma hareket mekanizması, mevcut su tankının üzerine monte edilmiştir. Hem dikey (aşağı yukarı) hem de yatay (sağa ve sola) yönler olmak üzere her iki eksen üzerinde de hareket ettirilebilen bu mekanizma ile kanat çarpma hareketinin sekiz çizebilmesi sağlanmaktadır. Doğadaki bazı kuşların kanat çarpma hareketi bu türdedir. Kullanılan hareket mekanizması, istenilen genlik ve frekansa kolaylıkla programlanabilmektedir ve söz konusu sekiz hareketini çok hassas bir şekilde çizebilmektedir. Kanadın firar ve hücum kenarlarının girdap oluşum mekanizmaları, Parçacık Görüntülemeli Hız Ölçüm (PGHÖ) tekniği ile görüntülenmiştir. Deneyler, çeşitli parametrelerin etkisini görmek amacıyla; farklı y yönündeki sekiz şekli çizen çirpan kanat hareket genliklerinde, farklı hücum açılarında ve farklı kanat profillerinde (simetrik ve kamburlu) yapılmıştır. Yapılan deneysel çalışmalar ile elde edilen düzensiz davranışlı girdap yapıları incelenmiş, kaldırma ve sürüklenme kuvvetlerine etkileri değerlendirilmiştir. Bununla birlikte, Başkan [10] tarafından yapılan nümerik çalışmalar, deney çalışmalarıyla desteklenmiş ve tamamlanmıştır.

Anahtar Kelimeler: Çirpan kanat hareketi, Parçacık Görüntülemeli Hız Ölçüm (PGHÖ)

To my family

ACKNOWLEDGEMENTS

I would like to express my deepest thanks and gratitude to my supervisor Prof. Dr. Nafiz Alemdarođlu for his encouragement, guidance, advice and support throughout this study.

I would like to thank to my team-mates and dearest friends N. Ođuz Erkmn and İrem Ersöz for their friendship, help, encouragement, patience and effort. If they had not been with me at all weekends (from the date of Jan. 15, 2012 to June 16, 2013) for performing the experiments, I could not complete this thesis. Also special thanks to Hasan Hızlı for being with me in numerical studies and sharing his knowledge about CFD modeling and analysis, very clearly in a very brief time.

I also wish to thank to all my colleagues at ROKETSAN-TFS-STDM-DDTB, especially Yasin Polat, Halise Irak, Özer Güvenç, Sadi Başođlu, Anıl Güçlü, Yasin Genç and Ö. Serhat Büyükçolak for their support, understanding and motivation.

I wish to give my special thanks to my friends, Aysegül Afal and Berat Aytaç. The first sentence of this thesis is written in Nanolab (METE) in METU with Ayşegül Afal and all my sentences in this thesis are read by Berat Aytaç. Thanks them for their friendship, infinite support, help and kindness.

I would like to thank to my friends Gizem Yücel, Seda Gürün, Selma Es, Tayfun Aytaç, Yađmur Atay and all my friends for their friendship, encouragements and support.

My special appreciation goes to my mother Şengül, my father Orhan, my brother M. Ziya and my sister Büşra for their love, support, persistent confidence on me and understanding at all stages of my life. Without their presence, this thesis would not have been possible.

Last, but definitely not the least, I am very grateful to E. Ersin Yıldırım for his love, patience, understanding during this study, always believing in me and supporting in any case. Thank you for everything, thank you for always being there for me.

TABLE OF CONTENTS

ABSTRACT	v
ÖZ	vi
ACKNOWLEDGEMENTS.....	viii
TABLE OF CONTENTS	ix
LIST OF FIGURES	x
LIST OF TABLES	xiii
LIST OF SYMBOLS	xiv
CHAPTERS	
1 INTRODUCTION.....	1
1.1 INTRODUCTION	1
1.2 FLAPPING MOTION.....	4
1.3 OBJECTIVE AND OUTLINE OF THE PRESENT STUDY.....	8
2 LITERATURE SURVEY.....	11
3 EXPERIMENTAL STUDY.....	31
3.1 EXPERIMENTAL SETUP	31
3.2 EXPERIMENTAL METHOD	34
3.2.1 Particle Image Velocimetry Technique (PIV)	35
3.2.2 PIV Measurement Principle.....	36
3.2.3 Experimental Conditions	49
4 NUMERICAL RESULTS	53
4.1 EFFECTS OF VERTICAL AMPLITUDE OF MOTION	57
4.2 EFFECTS OF INITIAL ANGLE OF ATTACK	63
4.3 EFFECTS OF AIRFOIL PROFILE SHAPE.....	65
5 EXPERIMENTAL RESULTS.....	67
5.1 NACA 0012 AIRFOIL IN FIGURE OF EIGHT PATTERN IN HOVER	68
5.2 NACA 0012 AIRFOIL IN FIGURE OF EIGHT PATTERN IN HOVER	73
6 CONCLUSION.....	77
REFERENCES	79
APPENDICES	
A. Experimental Results	87
B. Numerical Results.....	93
C. Numerical results previously done [10]	95

LIST OF FIGURES

FIGURES

Fig 1 Re ranges for flight vehicles [1]	2
Fig 2 The AeroVironment Black Widow [5].....	3
Fig 3 MICOR (Micro Coaxial Rotorcraft) [4].....	3
Fig 4 The AeroVironment Microbat [6].....	4
Fig 5 Asymmetric hovering or avian stroke [8].....	5
Fig 6 Symmetric hovering [8]	5
Fig 7 Illustration of a hummingbird in hovering flight [7]	6
Fig 8 The figure of eight pattern of hummingbird [8].....	6
Fig 9 The definition of flapping motion determined by Kurtuluş [9]	7
Fig 10 Lissajous curve used for figure-of-eight motion [10].....	8
Fig 11 An example of the experimental results on the Lissajous curve	8
Fig 12 A drawing from Codex on Flight of Birds [15]	12
Fig 13 Small Wing-flapping (1893-1896) [16].....	12
Fig 14 First flight of the Wright brothers [17].....	13
Fig 15 The reverse von Karman vortex street and asymmetric wake [21]	14
Fig 16 Tethered locust flying [27]	14
Fig 17 The examples of the instantaneous vorticity contours of Freymuth [37].....	16
Fig 18 Experimental Setup used by Dickinson and Götz [38].....	16
Fig 19 The experimental method carried out for measuring wing-beat kinematics in real time [39].	17
Fig 20 Hawkmoth and the scaled-wing model [41]	17
Fig 21 Flow visualization of the LEV over a wing of the “flapper” during the downstroke [42]	18
Fig 22 The experimental apparatus used for filming [43]	19
Fig 23 Drosophila Melanogaster and the robofly taken from the Dickinson lab (used in 2012) [46]- [47].....	19
Fig 24 The Robofly experimental setup [45].....	20
Fig 25 Smoke flow over hawkmoth wings at $\alpha=0^\circ$ (A) and $\alpha=35^\circ$ (B) [50]	21
Fig 26 Vanessa atalanta [55]	22
Fig 27 Experimental setup [56]	22
Fig 28 The experimental setup used for DPIV analysis [61].....	23
Fig 29 The rufous hummingbird [65]	24
Fig 30 Encarsia Formosa [69]	25
Fig 31 Bumblebee [71]	25
Fig 32 Dragonfly [73]	26
Fig 33 The experimental setup to measure thrust and lift of flapping wing MAVs [77].....	27
Fig 34 The experimental setup used in this study [79].....	27
Fig 35 Rhinoceros Beetle, Trypoxylus Dichotomus [82].....	28
Fig 36 Experimental setup used for linear motion [10].....	29
Fig 37 Experimental Setup.....	31
Fig 38 Flapping motion mechanism	32

Fig 39 The motion control program.....	33
Fig 40 Two wing models (NACA0012 and NACA6412).....	33
Fig 41 Flow velocity measurement techniques [83]	34
Fig 42 Inhomogeneous and homogeneous seeding [84].....	35
Fig 43 Determination of approximately particle displacement and its relationship to actual fluid velocity [84].....	36
Fig 44 Basic Principle of PIV [86]	37
Fig 45 Interrogation areas [86]	37
Fig 46 Image analysis (simply) [86]	38
Fig 47 Flowchart of the PIV measurement and analysis process (Reprinted from Westerweel) [84]	38
Fig 48 S-HGS [88] and image density of the particle taken from this study	40
Fig 49 New Wave Solo PIV II-15, Laser Nd:YAG	41
Fig 50 Laser head layout-532nm [89].....	42
Fig 51 Schematic illustration of light-sensitive pixels and storage cells of the CCD cameras [86] ...	43
Fig 52 HiSense MkII (cameras used in present study)	44
Fig 53 AF-MICRO-NIKKOR of 60 mm f/2.8mm and optical filter [91].....	44
Fig 54 Cross-correlation technique [92].....	45
Fig 55 Numerical processing flowchart of cross-correlation technique [86].....	46
Fig 56 The illustration of how velocity information is extracted from an image pair [92].....	47
Fig 57 Auto-correlation analysis of multiple images [83].....	48
Fig 58 2-D grid domain and its distribution around the NACA0012 airfoil.....	54
Fig 59 Time histories of lift and drag coefficients with different grids (top) and with different time-steps for NACA0012 airfoil over three periods of motion [96].....	55
Fig 60 The flow schema.....	56
Fig 61 Time histories of the aerodynamic lift and drag coefficients versus the vertical amplitude of the figure of eight flapping motion for NACA 0012 with $\alpha=30^\circ$ and $B=c$, $B=2c$	57
Fig 62 Time histories of the aerodynamic lift and drag coefficients versus the vertical amplitude of the figure of eight flapping motion for NACA 6412 with $\alpha=30^\circ$ and $B=c$, $B=2c$	58
Fig 63 Lift and drag versus the the vertical amplitude of the figure of eight flapping motion for NACA0012 (top) and NACA6412 (bottom) with $\alpha=30^\circ$ and $B=c$, $B=2c$	59
Fig 64 L/D ratio versus the the vertical amplitude of the figure of eight flapping motion for NACA 0012 (right) and NACA6412 (left) with $\alpha=30^\circ$ and $B=c$, $B=2c$	60
Fig 65 Instantaneous vorticity contours of NACA 0012 during the 7th period for $\alpha=30^\circ$, $B=c$, $B=2c$ and $Re=1052$	61
Fig 66 Instantaneous vorticity contours of NACA 6412 during the 7th period for $\alpha=30^\circ$, $B=c$, $B=2c$ and $Re=1052$	62
Fig 67 Time histories of the aerodynamic lift and drag coefficients versus the initial angle of attack ($\alpha=30^\circ$, $\alpha=60^\circ$.) for NACA 0012 and $B=c$	63
Fig 68 Instantaneous vorticity contours of NACA 0012 during the 7th period for $\alpha=30^\circ$, $\alpha=60^\circ$ and $B=c$, $Re=1052$	64
Fig 69 Time histories of the aerodynamic lift and drag coefficients for NACA 0012& NACA 6412 airfoil profiles for $B=2c$, $\alpha=60^\circ$	65
Fig 70 The flow schema of NACA0012 for $\alpha=30^\circ$, $B=c$ and $Re=1052$	68
Fig 71 Instantaneous vorticity contours of NACA 0012 during the 7 th period for $\alpha=30^\circ$, $B=c$, $B=2c$ and $Re=1052$	69
Fig 72 Instantaneous vorticity contours of NACA 0012 during the 7 th period for $\alpha=45^\circ$, $B=c$, $B=2c$ and $Re=1052$	70
Fig 73 Instantaneous vorticity contours of NACA 0012 during the 7th period for	72
Fig 74 The flow schema of NACA6412 for $\alpha=30^\circ$, $B=c$ and $Re=1052$	73

Fig 75 Instantaneous vorticity contours of NACA 6412 during the 7th period for $\alpha=30^\circ$, $B=c$, $B=2c$ and $Re=1052$ 74

Fig 76 Instantaneous vorticity contours of NACA6412 during the 7th period for..... 76

LIST OF TABLES

TABLES

Table 1 The basis of flapping motion investigation	11
Table 2 Specification of S-HGS [87]	39
Table 3 Specification of Solo PIV II-15 [89]	42
Table 4 Specifications of HiSense MkII [90]	44
Table 5 Auto-correlation vs Cross-correlation [94]	48
Table 6 The experimental conditions of this present study	51
Table 7 The cases for numerical studies	56
Table 8 Test cases for the airfoil.....	67

LIST OF SYMBOLS

DARPA	: Defense Advanced Research Project Agency
LEV	: Leading Edge Vortex
MAV	: Micro Air Vehicle
PIV	: Particle Image Velocimetry
Re	: Reynolds number
TEV	: Trailing Edge Vortex

CHAPTER 1

INTRODUCTION

1.1 Introduction

In this thesis, the flow field around flapping airfoils making the figure of eight in hover (no free stream velocity) is investigated experimentally and the cases determined for comparing the experimental results, the numerical study is performed. The aim of this experimental study is to support and complete the numerical study previously done by Başkan [10] and the present numerical study. The Particle Image Velocimetry (PIV) technique is performed to analyze the vortex shedding mechanism from the leading and trailing edges of the airfoil. Experiments are carried out to investigate the effects of different parameters such as the amplitude of motion in y-direction, angle of attack and camber on the vortex formation. Both symmetric and cambered airfoil, NACA0012 and NACA6412, are analyzed at three different angles of attack (30°, 45°, and 60°) for two different amplitudes of motion in y-direction at Reynolds number, 1052. Then, numerical results obtained from previous work [10] and present work are compared to vorticity contours obtained from the experiments.

To start with Micro Air Vehicles (MAVs), MAVs have been an interest research area for the aerodynamicists in the past decade since these vehicles are small, inexpensive and functional for some applications, such as surveillance and reconnaissance, where the use of larger vehicles is not practical. MAVs are defined as a flying vehicle to a size less than 15 centimeters (about 6 inches) in length, width or height by the Defense Advanced Research Project Agency (DARPA). This small size scale and low velocities result in a very sensitive Reynolds number (Re) regime 10^3 - 10^5 , where the flow separation around an airfoil can cause in sudden increases in drag and loss of efficiency. The gross mass of MAVs and other flight vehicles vs. Re is shown in Fig 1. Being in this flight regime, MAVs differ with conventional aircraft.

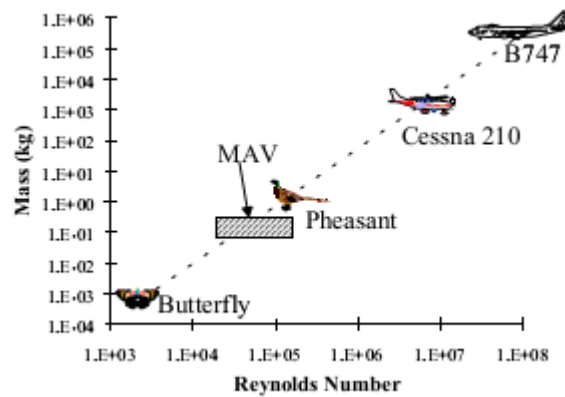


Fig 1 Re ranges for flight vehicles [1]

Also, with this limitation of 15 cm, MAVs have some advantages, these are:

- MAVs are more reasonable to a faster, better and cheaper approach to their development and obtainment,
- They are practically undetectable,
- They can explore places and terrain that were previously not explorable, etc.

MAVs have a variety of applications, and these applications can be summarized as: [2]

- Reconnaissance for military,
- Surveillance,
- Defense applications,
- Weather forecast,
- Wildlife study and photography,
- Crowd control,
- Targeting,
- Border surveillance,
- Traffic monitoring,
- Tracking criminals and illegal activities,
- Biochemical and hazardous material sensing, and
- Inspection of pipes.

MAVs can be divided into three groups which are performing different aerodynamic characteristics: rotary wing, fixed wing and flapping wing. There are lots of studies about the steady aerodynamics of airfoils, and since it is easy to be implemented, the design of small fixed wing air vehicles is simple and the most common type, compared to the other characteristics of MAVs. Fig 2 shows the one of the first true MAVs (fixed wing), as envisioned by DARPA.



Fig 2 The AeroVironment Black Widow [5]

However, in low Reynolds number regime (10^3 - 10^5) where viscous forces are more significant, the boundary layer thickness and viscous drag increase which means the aerodynamic performance of fixed wing MAVs drops. Like fixed wing MAVs and the rotorcrafts, rotary wing MAVs use the conventional steady state aerodynamic principles for generating thrust and lift. An example of rotary wing MAVs is given in Fig 3.



Fig 3 MICOR (Micro Coaxial Rotorcraft) [4]

The most significant advantage of rotary wing MAVs compared to fixed wing is the hovering capability. However, they cannot provide long endurance. And the final group of MAVs, flapping wing MAVs, differs from both fixed and rotary wing MAVs in the case of lift generation mechanism. Flapping wing flight uses unsteady aerodynamics, which is different from conventional steady aerodynamic principles, relied on by fixed and rotary wing MAVs. An example of flapping wing MAVs can be seen in Fig 4.

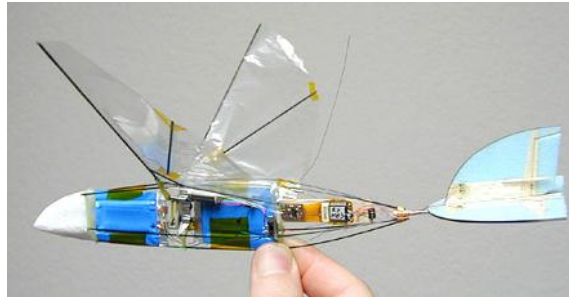


Fig 4 The AeroVironment Microbat [6]

Flapping wing micro air vehicles (MAVs) can provide important advantages over fixed wing and rotary wing MAVs due to the better aerodynamic performance, maneuverability and hover capabilities.

1.2 Flapping motion

Flapping motion is different from flight with fixed wing since the structural movement and the resulting unsteady aerodynamic mechanisms are different as mentioned before. While the lift is produced by the forward motion relative to air of wings in conventional airplanes with fixed wings, the wings move forward relative to the air in flapping flight, also they flap down and up, sweep and plunge. Birds systematically twist their wings to produce aerodynamic effects in ways that the ailerons on the wings of conventional airplanes operate while flapping. Specifically, when one wing is pronated which results in reducing the angle of attack and corresponding lift, the other wing is supinated for an increase in lift [7]. Among the types of flapping motion, hovering flight in a figure of eight pattern is discussed in this subsection.

Hovering flight is defined as a specific mode of flight where the body is fixed in space with zero free stream velocity. The types of hovering:

- Symmetric hovering, and
- Asymmetric hovering.

For an example of asymmetric hovering, large birds cannot rotate their wings between the forward and backward stroke so that the wings are extended to provide more lift during downstroke, whereas during the upstroke the wings are extended backward to reduce drag, called avian stroke (Fig 5) [8].

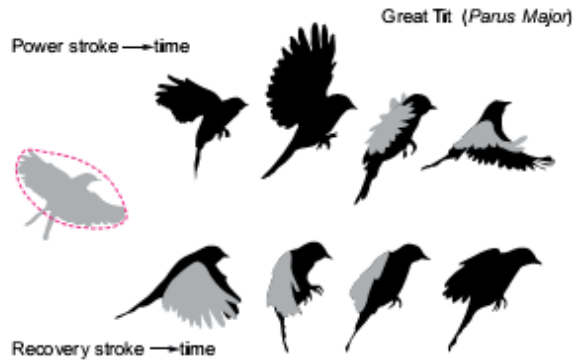


Fig 5 Asymmetric hovering or avian stroke [8]

And symmetric hovering (Fig 6) is carried out by insects or hummingbirds that remains in hover with fully extended wings through the all wing beat cycle. Lift is generated through the entire wing stroke, except at the reversal points.

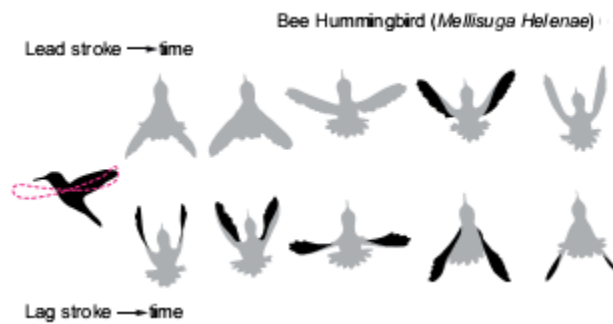


Fig 6 Symmetric hovering [8]

During the backstroke, the wings are rotated and twisted thus the leading edge of the wing remains the same during the cycle, however the upper surface of the wing throughout the forward stroke becomes the lower surface during the backward stroke. The illustration of the wing motion during downstroke and upstroke of the hummingbird is shown in Fig 7.

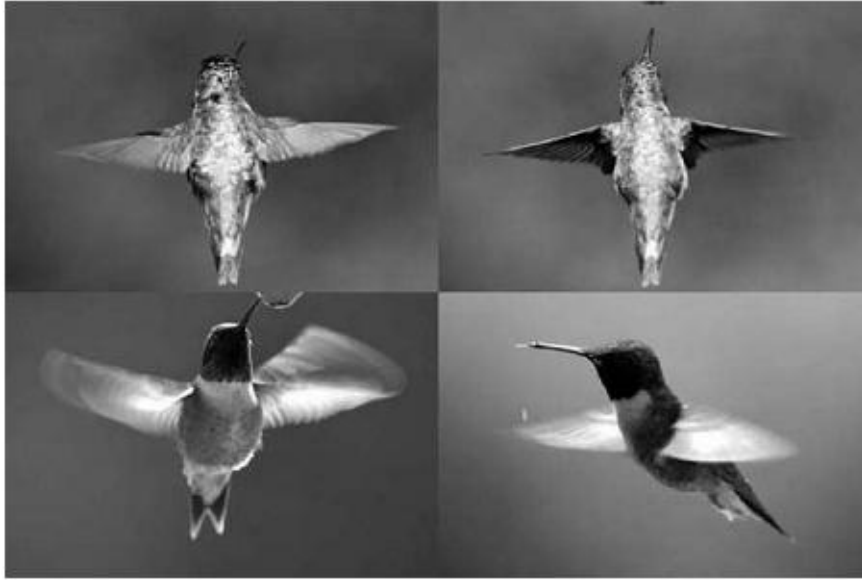


Fig 7 Illustration of a hummingbird in hovering flight [7]

And as seen in Fig 8, the body axis is inclined at a desirable angle and the wings are flapped in a figure of eight pattern during hover.

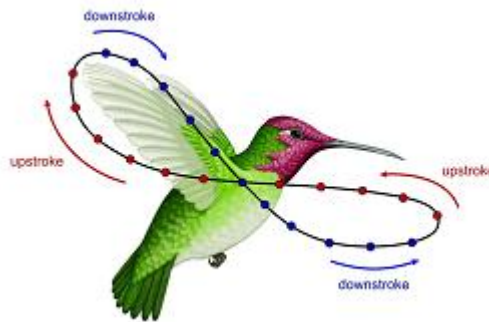


Fig 8 The figure of eight pattern of hummingbird [8]

In this present study, the flapping motion in hover making figure of eight pattern is investigated. To summarize the flapping motion in hover: there are two translational phases (downstroke and upstroke) where the translation of wings occur at high angles of attack and two rotational phases (supination and pronation) where the direction of motion of the wings is reversed.

The definition of linear flapping motion determined by Kurtuluş is given in Fig 9. According to this definition, the linear flapping motion is divided into 4 regions. While the first region shows the half of the downstroke, the second region shows the half of the

upstroke. The third and fourth regions are the mirror images of these two regions, gives the second half of upstroke and downstroke, respectively [9].

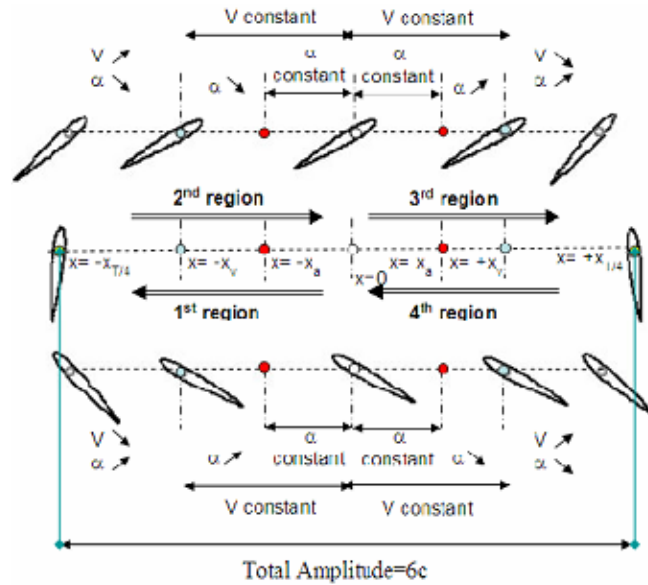


Fig 9 The definition of flapping motion determined by Kurtuluş [9]

Each region includes a rotational phase and a translational phase. In the translational phase, the airfoil moves with a constant velocity until the time t_v and position x_v , at which the velocity starts to decrease as seen in Fig 9. In rotational phase, a rotational motion around a point on the chord line from leading edge is superimposed on the translational motion at a predefined time t_a and position x_a . Each stroke starts from rest and comes to a stop [79].

T is the period of the flapping motion. The airfoil moves with a constant velocity from the origin ($x=0$) to the position of x_v at time t_v . After the position of x_v , the airfoil starts to decelerate and the velocity becomes zero at the quarter period and the airfoil also rotates around the center of rotation where it reaches 90° angle of attack at $t=T/4$.

While the linear flapping motion given in Fig 9 is described by Kurtuluş [9]; in this study, the flapping motion making figure-of-eight pattern given in Fig 10 is analyzed. For analyzing this motion, the Lissajous curve which is the graph of a system of parametric equations describing a complex harmonic motion is used and the airfoil moves on this continuous trajectory (Fig 10).

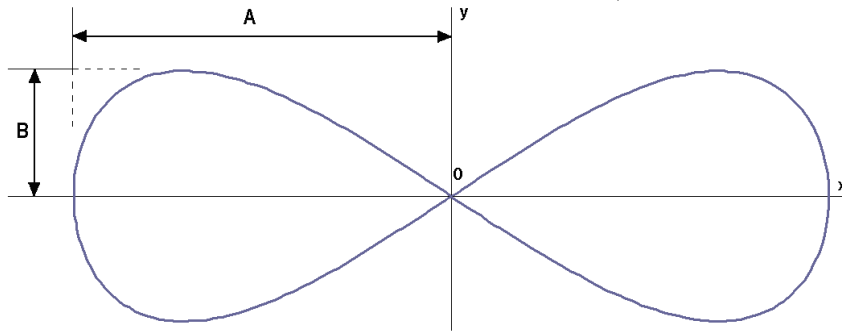


Fig 10 Lissajous curve used for figure-of-eight motion [10]

The parametric equations are given as follows:

$$x = A \sin (at + \delta) \quad \text{Eqn1}$$

$$y = B \sin (bt) \quad \text{Eqn 2}$$

where, $t \in [0, 2\pi]$, $\delta = \frac{\pi}{2}$, $a = 1$ and $b = 2$ values correspond to the horizontal figure-of-eight shown in Fig 10.

Using Eqn1 and Eqn2, the example of the experimental results on the Lissajous curve is given in Fig 11.

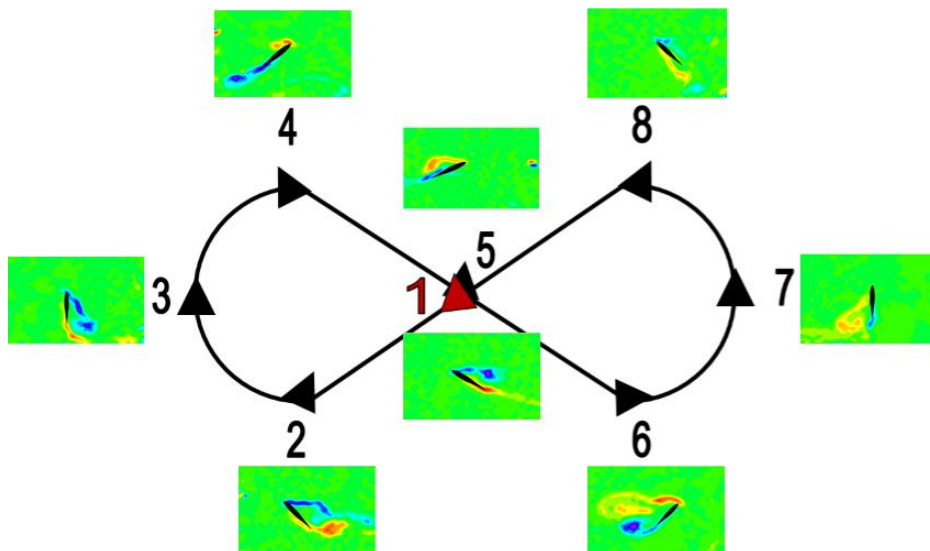


Fig 11 An example of the experimental results on the Lissajous curve

1.3 Objective and Outline of the Present Study

The aim of this thesis is to investigate and understand the vortex shedding mechanism from the leading and trailing edges of the airfoil which are responsible for the formation of aerodynamic forces in flapping motion making figure of eight in hover and validate the previous numerical work done by Başkan [10]. This investigation and validation is performed by experimental studies using PIV technique and numerical studies. The experimental studies are carried out at different angles of attack and amplitude of motion in y-direction for symmetric and cambered airfoil profiles. The unsteady behavior of the vortices shed from the airfoil is analyzed and the results are compared with the previous numerical studies.

This thesis is composed of 5 chapters. In Chapter 1, the Micro Air Vehicles, applications of MAVs and types of MAVs are explained briefly. After this brief information, flapping motion and the unsteady aerodynamics of flapping wings are explained and the outline of the present study is given in this chapter.

The literature about flapping motion which starts from the year of 1500s to the recent years is reviewed in Chapter 2.

The third chapter, Chapter 3, reviews the experimental setup and experimental method (PIV) that are used in this present study. In addition, the principles of Particle Image Velocimetry and experimental cases are given in this chapter.

In Chapter 4, the experimental results and the numerical results which include different cases are analyzed. The effects of parameters such as angle of attack, the amplitude of motion for symmetric and cambered NACA airfoils at Reynolds number, 1052, are investigated and the results are compared with previous numerical studies.

Chapter 5 gives the conclusion of the study. Some recommendations for the future studies are also given in this last chapter.

CHAPTER 2

LITERATURE SURVEY

Flapping motion has always been an intriguing research area for biologists and aerodynamicists from past to present. While biologists aim to investigate the aerodynamic mechanisms (nature) of birds and insects, aerodynamicists intend to comprehend the principles of flapping motion for the applications of MAVs such as military missions, search and rescue operations and commercial applications. Although the aims seem different, the main purpose for two researchers is same to investigate the flapping motion. Therefore, these studies carried out by biologists and aerodynamicists are combined to understand the flapping motion phenomena. The investigation of flapping wing motion is based on either the real insect/bird wing geometries or different airfoil profiles. Also, these studies can be divided into three groups: analytical, numerical and experimental studies. This chapter includes these three studies accomplished from the year of 1500s to the recent years. In Table 1, the basis summary of this flapping motion investigation can be seen. In analytical studies, the flapping wing aerodynamic phenomena is divided in two facts, unsteady models and quasi-steady models. While in the quasi-steady model, it is assumed that flapping frequencies are slow enough so that the shed wake effects are negligible, the unsteady approach tries to model the wake. In numerical studies, the complex unsteady aerodynamics associated with flapping wings can be solved. And finally, in experimental studies where the most significant information of the flapping flight field of investigation can be provided, actual aerodynamic performance is measured and the motion of wing and the fluid dynamic reaction to the motion is explained.

Table 1 The basis of flapping motion investigation

	Real wing geometry of birds/insects	Airfoil profiles
Analytical Studies	√	√
Numerical Studies	√	√
Experimental Studies	√	√

As mentioned before, this research area is almost as old as humanity. In 1505, Leonardo da Vinci wrote a manuscript about the flight behavior of birds and the flying machines with this mechanism called “Sul volo degli Uccelli (Codex on the Flight of Birds)” [14]. Many

sketches of bird's wings (Fig 12), artificial wings and several designs for flying machines were included in that manuscript.



Fig 12 A drawing from Codex on Flight of Birds [15]

The purpose of his flapping wing study was to understand how the birds exploit the air currents and wind. Although the efforts, about trying to launch the flight of the machines constructed, of Leonardo resulted in failure, the fact that the center of gravity of a flying bird did not coincide with its center pressure was noted for the first time.

Until the mid-1800s, the little progress was made. In 1867, Otto Lilienthal started his flight experiences with his brother Gustav Lilienthal after observing the flight of birds and Lilienthal understood that flight stability can be achieved with a cambered airfoil wing [16]. In 1889, the book about the theory of bird flight, experiments performed for different shape of the wings and the details of his predictions for the energy required for flapping wing flight called “Der Vogelflug als der Grundlage Fliegekunst (Bird flight as the basis of aviation)” was published by Lilienthal. In 1891, the first successful manned aircraft in history was achieved with a distance of about 80 feet. Between 1891 and 1896, over 2000 experiments have been performed (One of them is seen in Fig 13).



Fig 13 Small Wing-flapping (1893-1896) [16]

Lilienthal explained that the results were not presented as final since the equipment still required improvement. However, experimentation with different shape of wings and

observation of birds presented by Lilienthal has become an inspiration for Wright brothers for developing a controllable, self-propelled flying machine and achieving the first powered and maintained heavier than air human flight in 1903 (Fig 14) [17].



Fig 14 First flight of the Wright brothers [17]

After the success of flight with fixed wing, the fixed wing has become an interest research area for researchers and the development of flapping wing has been discouraged.

The earliest scientific history related to flapping wing was based on independent studies by Knoller and Betz in 1909 and 1912. They observed that a flapping wing creates an effective angle of attack, causing a normal force vector with both lift and thrust components. Therefore, it can be said that Knoller and Betz are the first ones to explain the ability of birds to produce a forward thrust by flapping wing. This phenomenon is referred to as the Knoller-Betz effect. In 1922, this effect was validated experimentally by oscillating the freestream velocity sinusoidally not flapping airfoil in wind tunnel tests at the Technical University of Vienna by Katzmayr [18]. The resulting measurements showed that an airfoil mounted in an oscillating wind stream generated thrust force. In the following years, in 1924, solutions for an incompressible flow passing flapping airfoil was developed by Birnbaum and the conditions resulted in thrust generation were analyzed.

In 1935, an analytical approach for evaluating the unsteady lift and moment on harmonically oscillating airfoils was published by Theodorsen [19]. The flow was assumed inviscid and incompressible while deriving this method. Also, since Theodorsen used the assumption of small amplitude oscillations, the flow was assumed to remain fully attached to the airfoil during the flapping cycle (the Kutta condition is applied at the trailing edge of the airfoil). The theory of Theodorsen has become standard mechanism while analyzing the flutter, aerodynamics of rotorcraft and flapping flight.

In the mid 1930s, the first theoretical explanation of drag and thrust generation was undertaken by von Karman and Burgers [20]. This explanation was based on the observed placement and orientation of the wake vortices. The Fig 15 illustrates that the flapping motion produces a typical example of a reverse von Karman vortex street and an asymmetric wake is established, respectively.

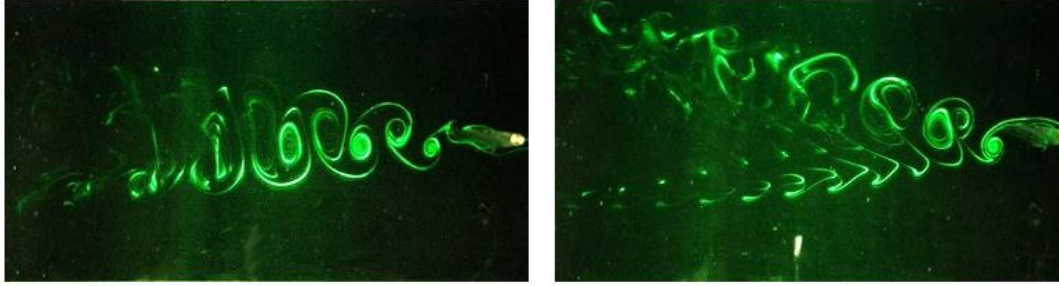


Fig 15 The reverse von Karman vortex street and asymmetric wake [21]

In this study, von Karman and Burgers investigated that a wake including two rows of counter-rotating vortices can get thrust force on an airfoil in an incompressible flow. In 1936, Garrick [22] applied the theory of Theodorsen which was inviscid, incompressible, oscillatory, flat plate theory as explained above to determine the thrust force. This study revealed that while flapping airfoils generate thrust over the whole frequency range considered, pitching airfoils generate thrust only with frequencies above a certain critical value. The result of the study of Garrick was verified experimentally by Silverstein and Joyner in 1939 [23].

In 1942, Schmidt recognized the fact that some of the flapping energy is lost in the form of vorticity shed in the wake, and he showed that a stationary wing placed in the oscillatory wake of a flapping wing results in increasing of propulsive efficiency, the aft wing thus is exposed to an oscillatory flow which generates thrust by the Katzmayr effect. As a result of his studies about flapping foils, the wave propeller performed a plunging or flapping motion which was perpendicular to the airflow was developed.

In 1950, observations of von Karman and Burgers were performed with flow visualization experiments by Bratt [28]. The experimental results included several cases where a non-symmetrical, deflected wake pattern was observed, but no explanation was made about these deflected wakes.

In 1957, Weis-Fogh and Jensen [26] showed that the flow affected by the motion of bird and insect wings are highly unsteady and vertical by using high-speed motion-picture cameras and tethered locusts [27]. Therefore, the quasi-steady theory used as a first estimate of the forces acting on flapping wings failed.



Fig 16 Tethered locust flying [27]

The replacement of thin airfoil theory of Theodorsen by an approach that enables the computation of incompressible potential flow past oscillating airfoils of arbitrary shape was achieved by the placement of sources and vortices on the airfoil surface rather than along the chord line in 1968. This was called panel method by Giesing [25]. This method was formed by Platzer and Jones. They studied the flow over single foils using a time-dependent, 2-D panel code coupled with a boundary layer algorithm. The result was that propulsive efficiency can be increased by reducing the frequency, raising the amplitude of the motion and retaining the Strouhal number constant.

And later in 1970s, Lighthill [24] performed a very similar analysis to that of Garrick. In addition to the study of Garrick, Lighthill made an assumption of pitching motion leading plunging motion by 90 degrees. He expressed thrust and propulsive efficiency identical to those of Garrick using an energy method by converting into similar terms.

The flapping motions of insects in forward flight and in hover conditions were observed by Maxworthy in 1981 [29]. The hovering motion was investigated for four categories: normal hovering, the clap-fling mechanism named by Weis-Fogh, inclined wing stroke plane and vertical wing stroke plane.

Ellington [30-35] published a series of papers called “The aerodynamics of hovering insect flight” which includes the quasi-steady analysis, morphological parameters, kinematics, aerodynamic mechanism, a vortex theory and lift and power requirements in 1984. His study provided very significant information about hovering insect flight and includes both experimental and computational methods. By analyzing the data from papers, the answer for the question posed by Weis-Fogh: “to what extent do hovering animals rely on quasi-steady aerodynamics?” was provided that animals using an inclined stroke plane must employ unsteady aerodynamics because the lift required of the wings exceeds that expected under quasi-steady conditions. To conclude, the results showed that the aerodynamics of hovering animals does not depend on quasi-steady approach. And it is understood that the aerodynamics of hovering animals is based on rotational lift mechanisms. When it was resulted in that rotational structures highly affect the flow characteristics around flapping wings, experiments and numerical simulations for biological flight and simplified modeling were conducted. In simplified modeling studies, the different airfoil profiles were used instead of insect/bird wing geometries used in biological studies.

In 1990, a thin flat plate with rounded edges in the pitch-plunge motion in hover was studied experimentally by Freymuth [36]. The experiments were carried out by a flow field visualization method named titanium-tetra-chloride method. The thrust generation mechanism of this unsteady motion for Reynolds numbers of between 340 and 1700 was investigated. The examples of the instantaneous vorticity contours from this experiment (experiment conditions: $\alpha_a=66^\circ$, $h_a/c=1.5$, $R_f=340$, $f=1\text{Hz.}$, $\Delta t=1/16\text{s}$) is shown in Fig 17. The experiment results showed that reverse Karman Vortex Street investigated in normal hover modes was more powerful than other two hovering modes causing the generation of larger thrust coefficient.

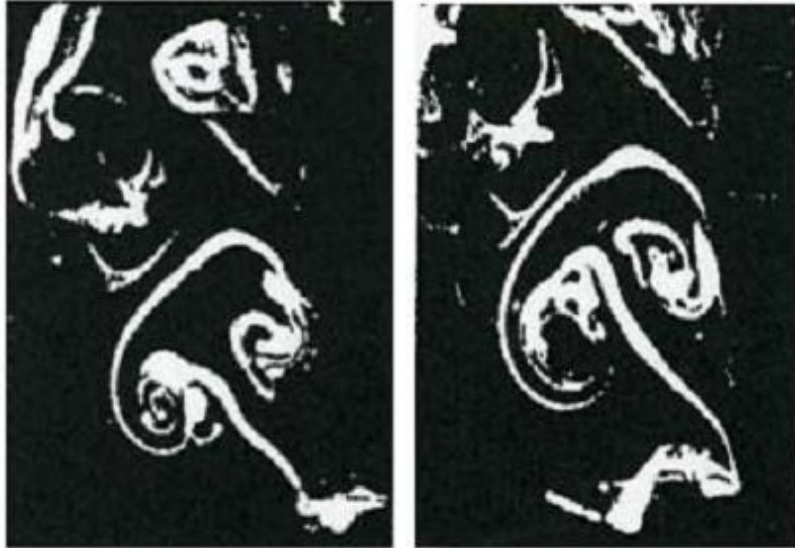


Fig 17 The examples of the instantaneous vorticity contours of Freymuth [37]

In 1993, Dickinson and Götzt [38] investigated the unsteady aerodynamic characteristics of model wings at low Reynolds numbers. The purpose of this study was to characterize the time-dependence of forces produced by impulsively moved wings. Then, the knowledge of unsteady mechanisms might be concerned by insects during flight. In the experiments, the experimental setup used for measurement of aerodynamic forces during acceleration of a wing to constant velocity starting from rest, (as shown in Fig 18) was used. The test chamber consists of a 100 cm x 340 cm x 360 cm glass aquarium filled with 54 % sucrose solution within a scaled aluminum wing model with a thickness of 2%, a span of 0.15 m and a chord of 0.05 m. The flow was seeded with aluminum particles and illuminated by a sheet of red light intersecting the model wing at its mid-section and recorded by a video tape.

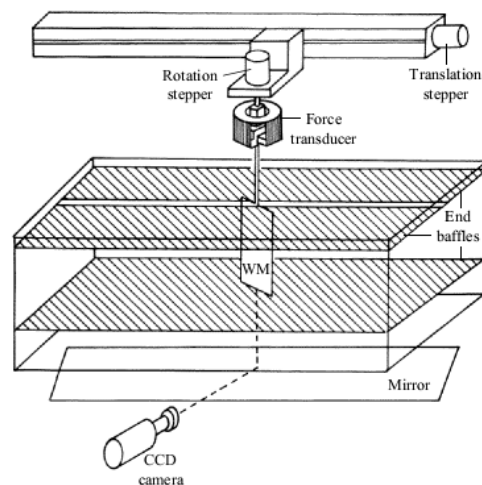


Fig 18 Experimental Setup used by Dickinson and Götzt [38]

Throughout the translation from downstroke to upstroke, the temporal control of a fast wing rotation in flies, the ventral flip, was investigated by Dickinson et al. [39] in 1993. For this investigation, several dozen flies (*Drosophila melanogaster*, in Fig 23) were used. The experimental method for determining wing-beat amplitude and ventral-flip timing in real time is shown in Fig 19. In the experiments, to track the movement of the shadow cast by the wing while it moves through light from an infrared emitter (IE) above the fly, an infrared detector (ID) and lens (L) were used. And the width of the grating (G) increased monotonically so that maximum occlusion took place during the downstroke. As a result, the independent control of flip timing and wing-beat amplitude by direct flight musculature responsible for steering movements and the interaction of these behaviors in production of aerodynamic force were explained.

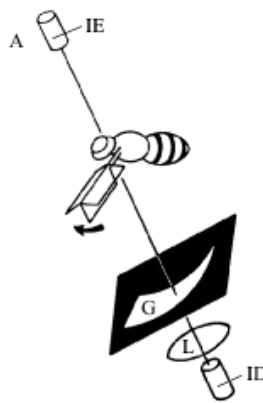


Fig 19 The experimental method carried out for measuring wing-beat kinematics in real time [39]

The airflow around the wings of the hawkmoth *Manduca sexta* and a hovering large mechanical model, “the flapper” was visualized by Ellington et al. in 1996 [40]. In Fig 20, the real hawkmoth and the flapper with scaled wing can be seen. The result was that an intense leading edge vortex (LEV) spiral out toward the wingtip was investigated and this result provided a qualitative explanation of one particular high-lift mechanism.

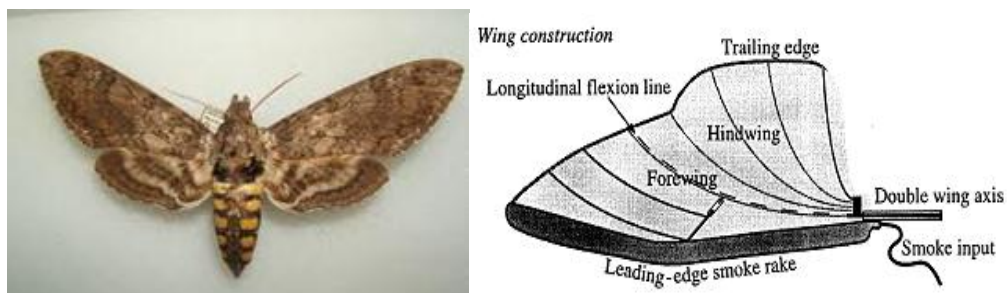


Fig 20 Hawkmoth and the scaled-wing model [41]

The three-dimensional leading-edge vortex of a ‘hovering’ model hawkmoth and the vortex wake of a ‘hovering’ model hawkmoth were investigated by Van den Berg and Ellington in 1997 [42]. In the experiments, smoke visualization mechanism for the scaled wing of hawkmoth *Manduca sexta* was used. Smoke was distributed from the leading edge and the camera was parallel to the wing surface (Fig 21). It is confirmed that the existence of a small, strong and stable leading-edge vortex, resulting in size increment from wingbase to wingtip.

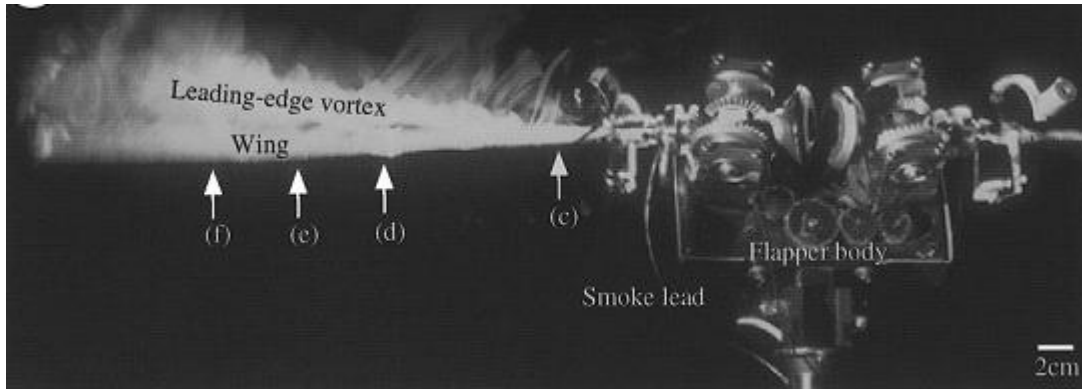


Fig 21 Flow visualization of the LEV over a wing of the “flapper” during the downstroke [42]

Also, Van den Berg and Ellington showed that “the leading-edge vortex have a strong axial flow velocity which stabilizes it and reduces its diameter and the vortex separated from the wing at approximately 75% of the wing length and thus feeds vorticity into a large, tangled tip vortex” [42].

The mechanics of flight in the hawkmoth *Manduca sexta* about kinematics of forward and hovering flight and also aerodynamic consequences of morphological and kinematic variation were evaluated by Willmott and Ellington in 1997 [43]. The experimental setup (Fig 22) used for this study consists of a large L-shaped cage suspended around a streamlined feeder positioned at the mouth of an open-jet wind tunnel. Small openings in the net allowed moths flying near the feeder to be filmed simultaneously from two cameras connected to a high-speed video system. The system was able to record the sequences of individual hawkmoths in free flight over a range of speeds from free stream velocity to 5 m/s. The results showed that aerodynamic importance of the kinematic changes that accompanies variations in forward velocity by calculating the mean lift coefficients at a range of speeds.

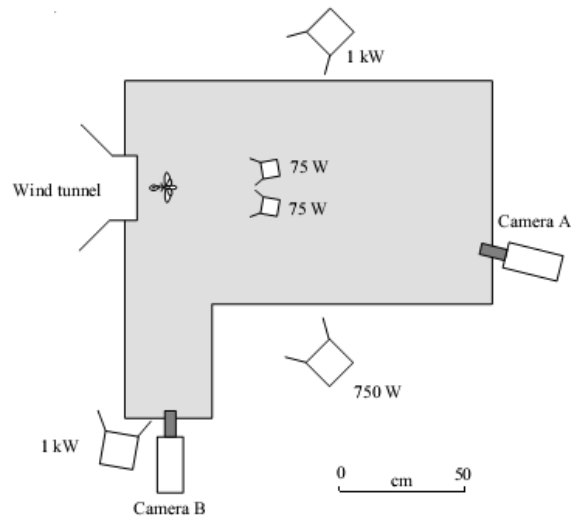


Fig 22 The experimental apparatus used for filming [43]

In 1999, Dickinson et al. [45] used a robotic system with a scaled-up wing of *Drosophila Melanogaster* called “Robofly” in their study (Fig 23). To measure forces and visualize the flow patterns on a robot fly at low Reynolds number regime (from 8 to 150), the Robofly experimental setup was used.

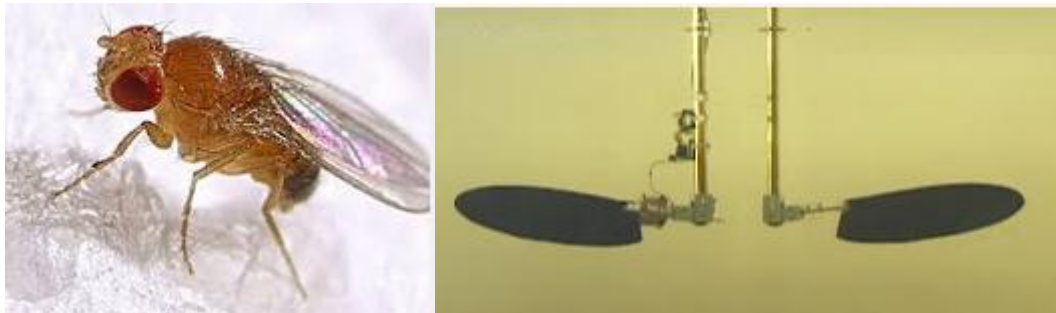


Fig 23 *Drosophila Melanogaster* and the robofly taken from the Dickinson lab (used in 2012) [46]-[47]

The robofly experimental setup which consists of a tank with mineral oil, six computer-controlled stepper motors connected to the wing gearbox via coaxial drive shafts and timing belts and the wing model is shown in Fig 24. They investigated the interaction of rotational circulation, delayed stall and wake capture at Re of about 136 and resulted that wake capture and rotational circulation are resulting from the airfoil and vortical flow interaction.

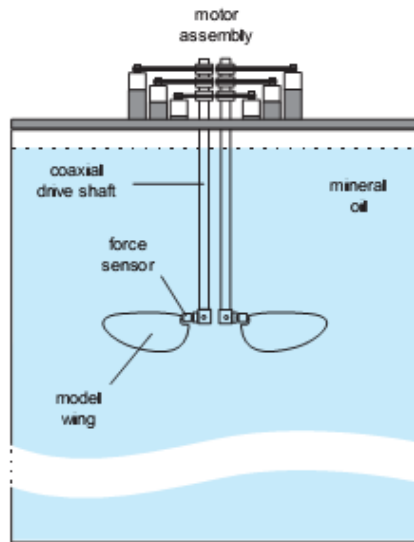


Fig 24 The Robofly experimental setup [45]

In 2000, Wang [49] showed that a 2D hovering motion can produce enough lift to support a typical insect weight. And that observation was obtained by computation of 2D insect in hover mode. This result suggested that the two-dimensional computations provide to guide the more detailed 3D simulations, and gives the basis for comparison between 2D and 3D effects.

For the investigation of the impact of the scaling parameters, the observation of different flow patterns around the model used above (Fig 24) were carried out by Birch and Dickinson in 2001 [48]. The Digital Particle Image Velocimetry (DPIV) technique was used for the flow visualization around the flapping wing of a dynamically scaled model insect for a series of reciprocating strokes starting from rest and the pattern of fluid motion was directly compared with the time history of force production. They showed that a spiral vortex similar to that generated by delta-wing aircraft at low Reynolds number is not produced by flapping wings and limiting spanwise flow with fences and edge baffles does not cause detachment of the leading edge vortex.

To measure the rotational forces generated by a flapping insect wing, Sane and Dickinson [51] performed their studies with a dynamically scaled model insect in 2002 (January). A steadily translating wing was rotated at constant angular velocities, and the resulting aerodynamic forces were calculated by the help of a sensor binded to the base of the wing. These forces measured were compared with quasi-steady estimates based on translational force coefficients. The rotational force coefficients for a range of angular velocities and different axes of rotation were determined and then the comparison of these coefficients with a mathematical model for 2D motions was performed in inviscid fluids. The results showed the effect of wing rotation on the production of aerodynamic forces by a flapping airfoil and the agreement of the measured rotational force coefficients with the theoretically estimated values.

In 2002 (March), Usherwood and Ellington [50] studied with flapping hawkmoth model and showed the significance of a spiral LEV formed by dynamic stall and maintained by some aspect of spanwise flow, to generate the lift required during flight. Also, they

investigated that steadily revolving model hawkmoth wings generate high lift and drag force coefficients because of the presence of LEV. The illustration of the experiment carried out by them can be seen in Fig 25. As seen in Fig 25, at very low angles of attack, the smoke describes an approximately circular path as the wing revolves underneath while at higher angles of attack, a spiral LEV and strong spanwise flow are observed.

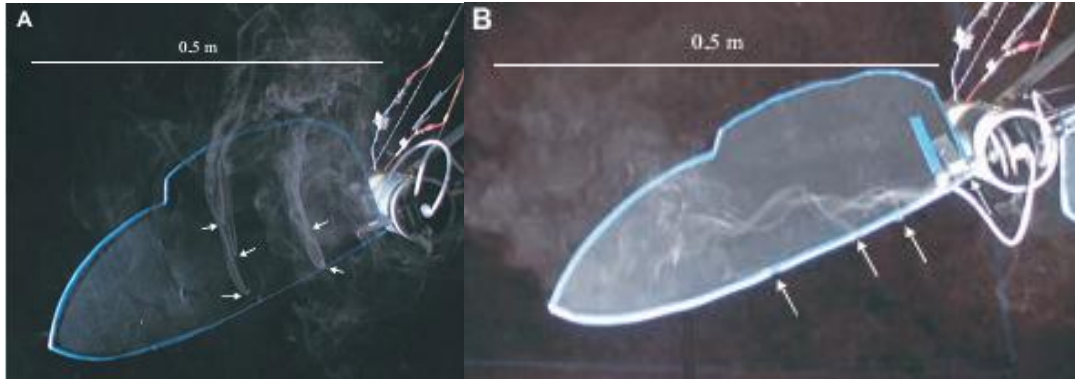


Fig 25 Smoke flow over hawkmoth wings at $\alpha=0^\circ$ (A) and $\alpha=35^\circ$ (B) [50]

A 3D computational study of the aerodynamic characteristics of insect flight was carried out by Ramamurti and Sandberg in 2002 (March) [52]. The unsteady flow past a 3D *Drosophila* wing facing flapping motion was computed by a finite element flow solver. The viscous effect and the phasing effect between the rotational and translational mechanism were investigated. The results revealed that as the wing rotation is advanced with respect to the stroke reversal, higher thrust forces are obtained and the thrust is decreased because of the delay of the wing rotation.

In 2002 (May), the study of the power and lift requirements for hovering flight in *Drosophila virilis* was performed by Sun and Tang [53]. Computational fluid dynamics was used for method and the Navier –Stokes equations were solved. From these solutions, the pressure fields and the flow velocity, that mean moments and unsteady aerodynamic forces, were provided. The results showed that comparing with symmetrical rotation, while larger lift is produced with advanced rotation; much less lift is generated with delayed rotation. And considering the power required, for balanced, long-duration flight symmetrical rotation should be utilized, but for flight control and maneuvering delayed and advanced rotation should be utilized.

To explain the unconventional force generation of free flying insects, Srygley and Thomas [54] performed experiments with free-flying butterflies, *Vanessa atalanta*, in 2002 (December) (Fig 26). High-resolution smoke-wire flow visualizations were used to provide qualitative, high-speed digital images of the air flow around the wings. The experiments showed that the unconventional aerodynamic characteristics are used to produce force by freeflying butterflies.



Fig 26 Vanessa atalanta [55]

To investigate the aerodynamics of free-flight maneuvers in *Drosophila*, 3D infrared high speed video and a robotic model were used by Fry et.al [56] in 2003 (April). Experimental setup used to film flight maneuvers is given in Fig 27. The results showed that the generation of rapid turns for wing motion occurs by a fly and the flight dynamics of flies is dominated by inertia.

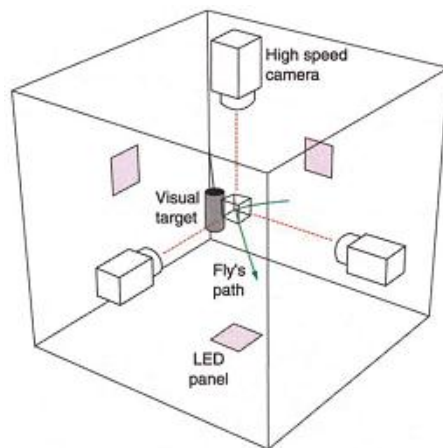


Fig 27 Experimental setup [56]

The unsteady aerodynamic forces of a model fruit fly (*Drosophila*) wing in flapping motion were analyzed by solving the Navier–Stokes equations numerically in 2004 (January) by Wu and Sun [60]. They showed that aerodynamic force coefficients are dependent only on five non-dimensional parameters: These were Re , midstroke angle of attack, stroke amplitude, non-dimensional duration of wing rotation and rotation timing. Then, they investigated the effects by changing these parameters on the force coefficients.

In 2004 (October), Wang et al. [57] compared experimental, computational and quasi-steady forces in a simple hovering wing with sinusoidal motion along a horizontal stroke plane. The unsteady effects were investigated and the comparison of 2D computations and 3D experiments were performed. They reported that the steady state two-dimensional

forces underestimate the three-dimensional forces whereas the transient. And in some cases, the two-dimensional unsteady forces end out to be good approximations of three-dimensional experiments.

In 2004, Singh et al. [58] study with insect-based flapping wings for micro air vehicles in hover experimentally by using laser sheet visualization method. The result of experiments showed that at high frequencies, thrust decreases. On the contrary, for a wing held at 90° pitch angle, flapping in a horizontal stroke plane with passive pitching caused by aerodynamic and inertial forces, the thrust was found to be larger.

By Miller and Peskin in 2004 (November), to perform an idealized ‘clap and fling’ stroke and a ‘fling’ half-stroke in the smallest insects, the two-dimensional Navier-Stokes equations were solved by performing the immersed boundary method [63]. The lift coefficients were calculated for different Reynolds numbers and the changes in lift related to the relative strength and position of the leading and trailing edge vortices and the instantaneous streamlines around each wing were calculated. The results showed that during the ‘clap and fling’ of two wings, comparison of lift generation per wing and average lift generated by one wing with the same motion should be observed for two different patterns, for $Re=64$ and higher and for $Re=32$ and lower. And by observing in that way, their results suggested that the Weis-Fogh mechanism of lift production have more advantages to insects flight at lower Re . Drag coefficients calculated during fling were also substantially higher for the two-winged case than the one-winged case, especially at lower Reynolds number.

In 2005, the leading edge vortex of *Manduca sexta* has been investigated by DPIV technique by Bomphrey et al. [61]. The aim of this analysis was to explain the exact structure of the leading edge vortex and how the stability of LEV is obtained during the downstroke. The DPIV setup used in that experiment can be seen in Fig 28. This analysis used for the flow field around the wings of an insect was the first DPIV analysis and also it was the first investigation of the flow field above the thorax. The results showed that the LEV structure toward the end of the downstroke is compatible with previous studies. It means that the leading edge vortex is continuous across the thorax and runs along each wing to the wingtip.

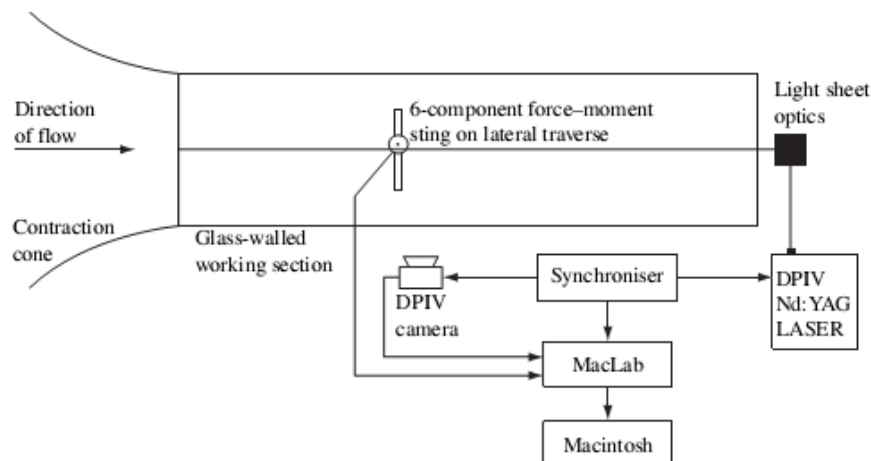


Fig 28 The experimental setup used for DPIV analysis [61]

Using DPIV technique, the measurements of the wake of rufous hummingbirds in hover mode (Fig 29) were provided by Warrick et al. in 2005 [64]. The results showed that hummingbirds generate 75% of their weight support through the downstroke and 25% throughout the upstroke. The reason of this asymmetry was probably due to inversion of their cambered wings through upstroke. Also, the LEVs formed during the downstroke showed that they can operate at Reynolds numbers sufficiently low to exploit a key mechanism typical of insect hovering.



Fig 29 The rufous hummingbird [65]

Lehmann et al. [66] used a dynamically scaled mechanical model of the small fruit fly *Drosophila melanogaster* in low Re regime (between 100–200) to investigate the effect of contralateral wing interactions throughout stroke reversal (the clap-and-fling) in 2005. 3-D DPIV technique was used to analyze clap-and-fling mechanism and it was shown that the most apparent effect of the bilateral image wing on flow occurs during the early phase of the fling, due to a strong fluid influx between the wings when they separate.

In 2005, Eldredge [60] explained the efficient computational tools for the simulation of flapping wing flow fields. The viscous vortex particle method for the simulation of flow produced by a two-dimensional rigid wing in pitching and plunging motion at a reasonable Reynolds number was employed. This method has some advantages that the correct velocity behavior at infinity is automatically accounted for and computational particles are only required in vortical regions of the flow.

The detailed vortical structure about a hovering hawkmoth were investigated and the inertial and aerodynamic forces, energetics and torques were evaluated by Aono and Liu in 2006 (July) [67]. Computational fluid dynamic study was carried out for this analysis and computations were performed by using multi-block and overset-grid-based in-house CFD solver with the geometric and kinematic model constructed based on the experimental data of a real hawkmoth. The results showed that the structure of LEV plays an important role in aerodynamic force production for hawkmoth in hover mode.

In 2006 (July), Sun and Yu [68] investigated the aerodynamic force production of a tiny insect (*Encarsia Formosa*) in hover mode (Fig 30). By solving the Navier–Stokes equations over moving overset grids, the results showed that while the fling generates a large lift peak at the beginning of the downstroke, near the end of the subsequent upstroke the clap

generates a large lift peak. And also when compared to the case of flapping without clap and fling, the lift peaks due to the clap and fling result in more than 30% increase in mean lift coefficient.



Fig 30 Encarsia Formosa [69]

The unsteady aerodynamics of a flying bumblebee (Fig 31) in hover flight were studied by using a computational fluid dynamics by Zuo et al. in 2006 (October) [70]. The kinematics data of wings documented from the measurement to the bumblebee in normal hover mode aided by the high-speed video and the Navier Stokes equations were solved numerically. The results showed that hovering flight is dominated by the unsteady aerodynamics of both the instantaneous dynamics and also the past history of the wing. Also, the simulation has shown that with the introduction of dynamic mesh model, it is possible to simulate the three-dimensional flow around flapping-wing insect to better understand the unsteady aerodynamics of insects.



Fig 31 Bumblebee [71]

In 2007, the first physical images showing the integral flow structures and their evolutions of dragonfly (Fig 32) in hover mode were shown, based on the dye flow visualization conducted on an electromechanical model in water tunnel by Lu et.al [73]. With the quantitative information derived from the images, the results showed that spanwise flow is conspicuous regardless of the large aspect ratio of the wing, the leading edge vortex

contains dual-vortex structure: the primary vortex do not develop along the leading edge but moves inboard, leaving a space for the formation of a same-sense minor vortex outside the primary vortex. Also the development of the LEV that shows a delay with respect to the translational motion of the wing was investigated and in most cases with forewing–hindwing interaction; the interaction was generally detrimental to the leading-edge vortices and was attenuated with the increase of the wing-root spacing.

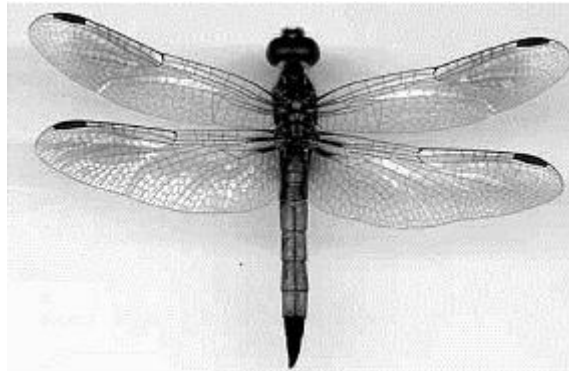


Fig 32 Dragonfly [73]

Interaction of aerodynamics with flexible wings of flapping vehicles in hover and cruise flight was studied experimentally by Mazaheri and Ebrahimi [76] in 2008. To analyze the effect of wing aeroelasticity on aerodynamic performance of a flapping motion, a flapping wing system and an experimental setup were designed and built. The setup allowed to measure the unsteady inertial and aerodynamic forces, and angular speed of the flapping wing motion for different flapping frequencies and for various wings with different chordwise flexibility. The power consumption, normal and axial forces, and inertial forces of different wings for no wind and cruise conditions were measured. Results showed how elastic deformations caused by interaction of inertial and aerodynamic forces with the flexible structure may affect specific power consumption.

Lift and drag forces associated with drag of compliant flapping wing for MAVs were measured by Mueller et al. [77] in 2008. First the compliant wing was designed by considering the effect of compliance on the production of lift and drag forces. To perform dynamic measurement of wing forces due to drag with adequate accuracy, the experimental setup (Fig 33) was used. The results showed that the detrimental influence of excessive compliance on drag forces during high frequency operation. Also, the useful effect of compliance on the formation of additional thrust at the beginning and end of upstrokes and downstrokes of the flapping motion were observed.

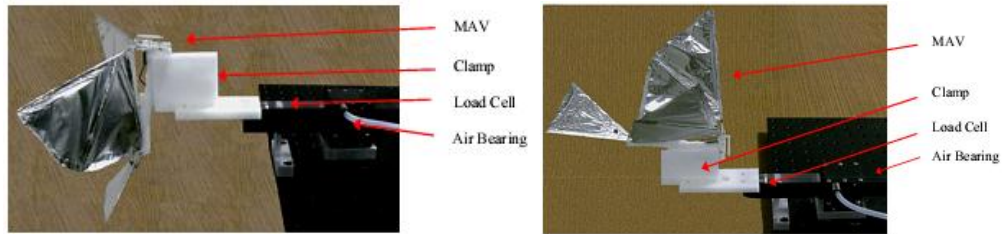


Fig 33 The experimental setup to measure thrust and lift of flapping wing MAVs [77]

The effects of stroke amplitude, flapping frequency and the inclined angle of stroke plane on lift and thrust force of a corrugated airfoil were investigated by Sun et. Al [78] in 2009. This investigation was performed with computing the flapping motion with time dependent 2D laminar Reynolds-averaged Navier-Stokes equations with the conformal hybrid mesh. The results revealed that the inclined angle is the most important factor on both the lift and thrust force.

To evaluate the unsteady vortex structures in the wake of a root-fixed piezoelectric flapping wing with the stroke amplitude, wing size and flapping frequency within the range of insect properties, the experimental investigation was carried out by Hu et al. [79] in 2010. A DPIV system was used to achieve phased-locked and time-averaged flow field measurements to quantify the transient behavior of the wake vortices in relation to the positions of the flapping wing through the upstroke and down stroke. The experimental setup can be seen in Fig 34.

The effects of the static angles of attack of the piezoelectric flapping wing were seen clearly by this system.

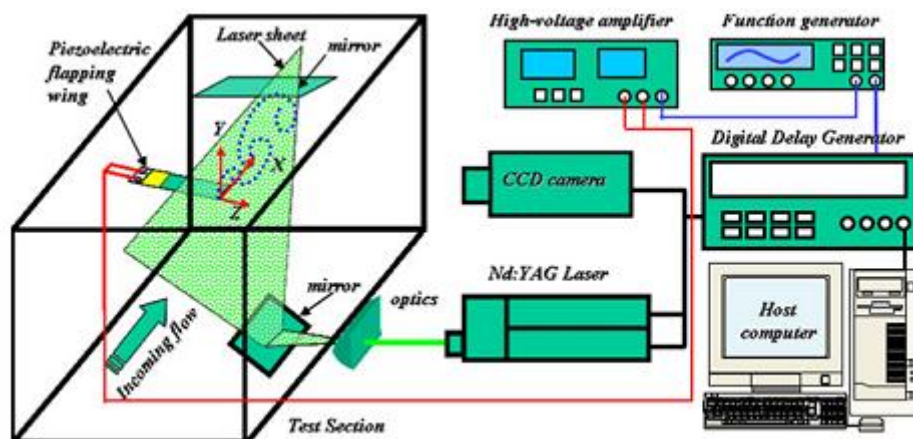


Fig 34 The experimental setup used in this study [79]

3-Dimensional (3D) wing kinematic parameters a beetle, *Trypoxylus di-chotomus*, that has a pair of elytra (forewings) and flexible hind wings (Fig 35), were provided experimentally

by Truong et al. in 2012 [81]. From a 3D reconstruction technique which includes the use of two synchronized high-speed cameras to digitize different points shown on the wings were used for investigation of the angle of attack, wing tip trajectory and camber deformation. The results showed that the dominant characteristics of deformation and flexibility of the beetle's hind wing compared with other measured insects, especially in the chordwise and spanwise directions during flapping motion. Also twisted shape showing large variation of the angle of attack from the root to the tip during the upstroke was observed.



Fig 35 Rhinoceros Beetle, Trypoxylus Dichotomus [82]

The flow field around a flapping airfoil making figure-of-eight motion and linear motion in hover was investigated numerically and these results were compared with the experimental results of linear flapping motion by Başkan [10] in 2009. Aerodynamic characteristics of these two-dimensional flapping motions were analyzed by using both the numerical (Computational Fluid Dynamics, CFD) and the experimental (Particle Image Velocimetry, PIV) tools. While the effects of parameters such as the amplitude of motion in y -direction, angle of attack, Reynolds number and camber were investigated numerically, the parameters, include angle of attack and camber, were investigated experimentally. The experimental setup used for that study is seen in Fig 36. The results indicated that relatively greater leading and trailing edge vortices are generated in figure-of-eight motion compared with linear flapping motion.

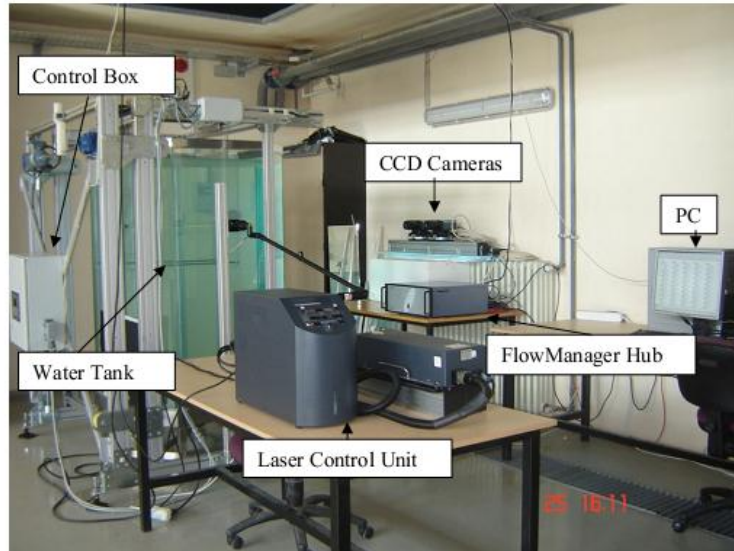


Fig 36 Experimental setup used for linear motion [10]

When the new setup (Fig 37) was designed and built after the study of Başkan, the y motion so that figure of eight motion of flapping motion was achieved experimentally. In 2012, the experiments for investigation of parameters selected and comparison with numerical results were performed by Erkmen et al [80]. The comparison the numerical results with experimental results showed that the results are compatible and can be used for design and development of MAVs.

CHAPTER 3

EXPERIMENTAL STUDY

The objective of the experimental study is to measure the leading and trailing edge vortex shedding mechanism for flapping airfoil in hover and to analyze the effects of parameters which are the vertical amplitude of the figure-of-eight flapping motion (B), initial angle of attack (α), and the shape of the airfoil. This chapter includes the experimental setup, the experimental method and the experimental procedure complied during the experiments.

3.1 Experimental Setup

The experimental setup used for this study differs from the other used in previous studies [10] carried out for the observation of flapping motion. Two dimensional motion (in the x and y direction) analysis can be obtained by the difference between the previous ones and our system. Therefore, in addition to linear type of flapping motion, the figure of eight motion can be performed.

The setup placed in Aerospace Engineering Department of Middle East Technical University, includes a water tank, a flapping motion mechanism (servo motors) placed above tank, two plexiglass endplates used for placement of the wing model, two wing model; NACA0012 (a symmetric airfoil profile) and NACA6412 (a cambered airfoil profile) and DANTEC PIV system (Fig 37).

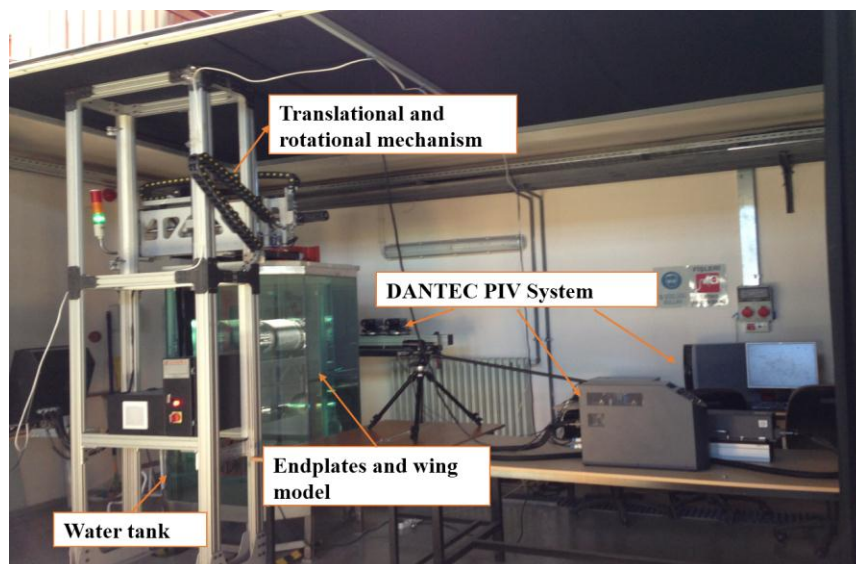


Fig 37 Experimental Setup

A small scale distilled water tank has a dimension of 1.0 m x 1.0 m x 1.5m (length x width x height) made of transparent and durable acrylic glass (altuglass).

A flapping motion mechanism controlled by computer provides the figure of eight motion of flapping motion. In order to make figure of eight motion, both vertical (up and down, y-direction) and horizontal motion (back and forward, x-direction) and whirling around can be performed by this mechanism. Fig 38 shows this mechanism.

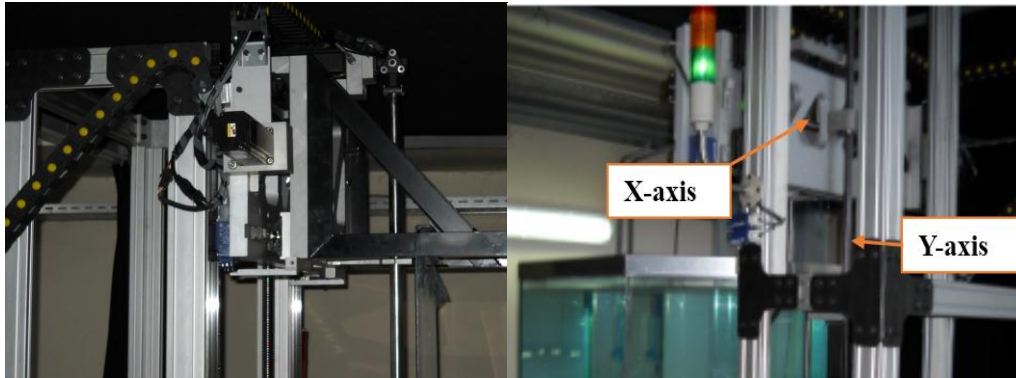


Fig 38 Flapping motion mechanism

As seen in Fig 38, this mechanism is comprised of servo motors so that the traversing system for the specified motion kinematics can be programmed easily. Also, although it is not possible to measure the exact forces acting on the airfoil during the flapping motion, it is possible to measure the torque generated by each of the servo motors which will be an indication of the forces generated by the flapping motion.

By programming the mechanism of motion, the amplitude and frequency can also be changed. The system achieves the flapping motion by the motion control program, shown in Fig 39.

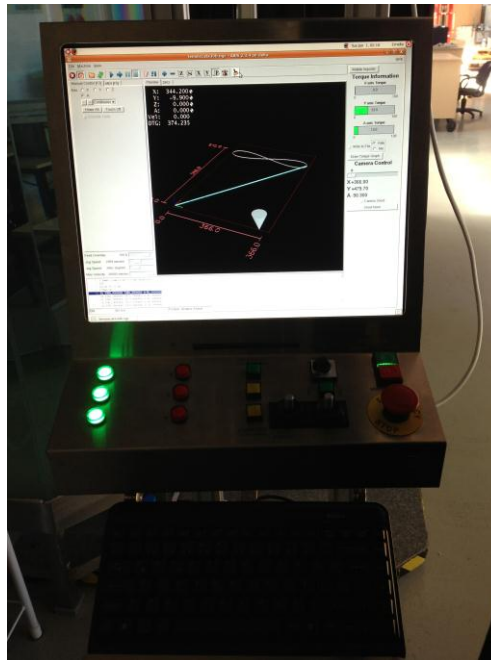


Fig 39 The motion control program

The motion control program can be run either manually or interactively and the data set keyboarded to program is converted to mechanical motion via signals which pass through the control box. Therefore, the motion can be controlled by the users. After the parameters investigated in experiments are determined, the program including these parameters is written in MATLAB. By MATLAB Importer, developed program is transferred to the system. Some parameters like velocity, start point and the period of motion are controlled by the motion control program. In this study, manual mode of this program is used.

Two plexiglass endplates are used for placement of the wing model to obtain a 2D flow and the endplates have dimensions of 90 cm x 50 cm (length x width). In experiments, while the wing model and the endplates are translated together, wing rotation is carried out freely. To investigate the effect of airfoil profile shape, the experiments are performed for two wing models; NACA 0012 and NACA 6412, shown in Fig 40.

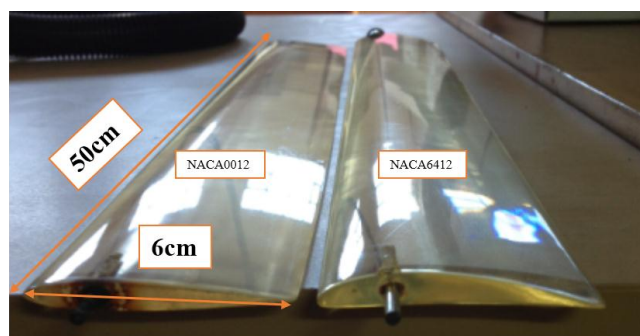


Fig 40 Two wing models (NACA0012 and NACA6412)

According to Fig 40, the wing models have a chord length of 6 cm and wing span of 50cm. The center of rotation of wing models is located at the quarter chord length of the airfoil from the leading edge. The motion of wing models is performed according to motion kinematics determined.

In this section, experimental setup used in this study is explained. Since the aim of this study is to measure leading and trailing edge vortex mechanism of flapping motion in hover (no free stream velocity), the experiments (PIV technique) are performed in water tank. Measurements are taken for after seventh periods of motion in order to achieve the periodicity of the flow.

Next section gives information about the PIV technique and DANTEC PIV system used in these experiments.

3.2 Experimental Method

Many different measurement techniques are used to measure the flow depending on the application. Flow measurement techniques can be divided into two groups; as intrusive techniques and non-intrusive techniques for measuring vector, as well as, scalar quantities in the flow. While in intrusive techniques instruments are located in the flow and affect the flow, in non-intrusive techniques instruments are located outside the flow and do not affect the flow. Therefore in non-intrusive techniques, the fluid flow to be analyzed is not affected. Intrusive and non-intrusive methods of flow velocity measurement techniques can be seen in Fig 41.

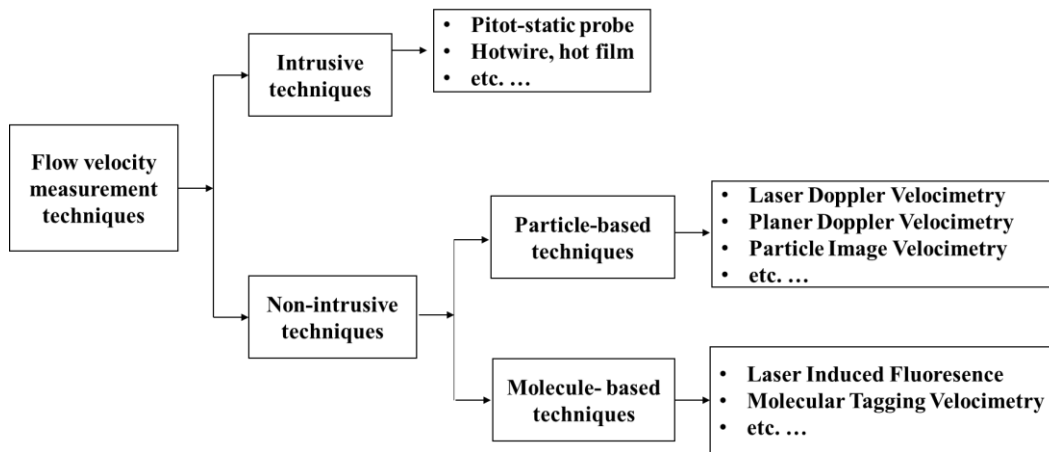


Fig 41 Flow velocity measurement techniques [83]

As shown in Fig 41, intrusive techniques include very significant methods, like hot-wire anemometers, for measurement multiple velocity components. However, both of these methods require the insertion of an instrument which disturbs the flow. Also, non-intrusive techniques consist of some common methods, like PIV, for fluid flow measurements. These techniques aim to determine flow properties from the analysis of light is either emitted or absorbed. Therefore, it can be said that these methods are mostly optically-based.

Among these measurement techniques Particle Image Velocimetry (PIV) is used for this study. Since flow can be interpreted both qualitatively and quantitatively instantaneously in contrast to other conventional methods.

In the following subsection, PIV technique, basic principles of PIV and the experimental conditions are explained.

3.2.1 Particle Image Velocimetry Technique (PIV)

PIV is a non-intrusive whole-field velocity measurement technique, which is founded on images of tracer particles seeded in the flow. In an ideal case, these tracer particles should follow the flow motion, homogeneously spread in the flow, and they should not interact with each other, alter the flow and the characteristics of flow. Fig 42 shows that inhomogeneous and homogeneous seeding, respectively.

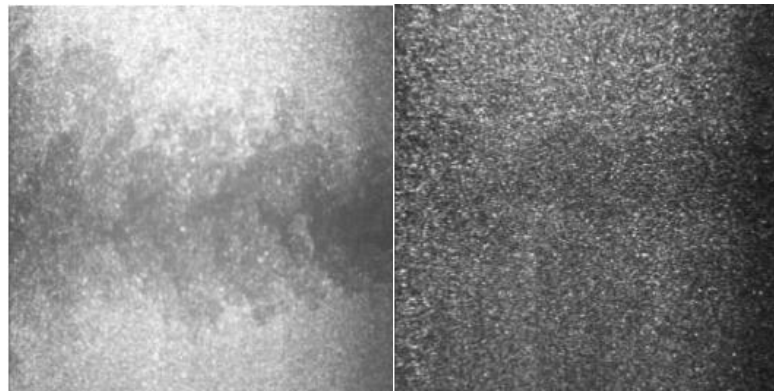


Fig 42 Inhomogeneous and homogeneous seeding [84]

In an ideal case, the velocity of the tracer particles is equal to the local fluid velocity. Therefore, the local fluid velocity ($u(X, t)$) can be evaluated indirectly, by measuring the displacement of the tracer particle ($D(X; t', t'')$) and dividing this displacement by the finite time interval $\Delta t = t'' - t'$ (Eqn3). ($U[X(t)]$ is the velocity of tracer particles).

$$D(X; t', t'') = \int_{t'}^{t''} \vartheta[X(t), t] dt \quad \text{Eqn 3 [84]}$$

However, the concept of this ideal case can only be approximated in a practical case. In addition to this, Eqn3 means that the displacement field only gives information about the average velocity along the trajectory over a time Δt . This can be shown in Fig 43.

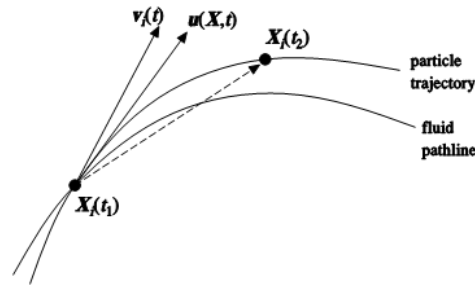


Fig 43 Determination of approximately particle displacement and its relationship to actual fluid velocity [84]

The major advantages of the PIV technique are [85]:

- Since multiple instantaneous whole flow field velocity images provide visual validation of flow patterns, it is very useful in understanding flow phenomena.
- It is nonintrusive technique, means that seed particles selected appropriately has practically no effect on the flow. In addition to this, this technique avoids the need for intrusive flow measurement probes.
- Large quantities of image pairs which can be generated in a relatively short period of time can be analyzed rapidly or later time.
- Since each vector is the statistical average for many particles within a particular tile, this technique provides high degree of accuracy.

However, there are also some limitations for using PIV [85]:

- Since the velocity vectors are measured using cross correlation of intensity distributions over small areas of the flow field, the resulting velocity field is a spatially averaged representation of the actual velocity field. This effects the accuracy of spatial derivatives of velocity field, vorticity and spatial correlation factors.
- 2D PIV does not account for the third component of the velocity field which can interfere with the 2D data.
- Due to higher density of tracer particles, flow motion cannot be exactly followed. Also, the size of the seeding particles limits the size of recordable flow field.

To summarize, although there are some disadvantages for using PIV technique, this technique is plausible for this study since it puts into evidence the vortex shedding mechanism from the leading and trailing edges of the airfoil.

3.2.2 PIV Measurement Principle

The measurement principle of PIV is quite simple: the flow is seeded with tracer particles to track the flow motion (seeding), these particles are illuminated by a light sheet (laser) in the measurement plane and the camera is used to capture the images (positions) of the

tracer particles at two successive instant time. Then, image analysis is performed for getting velocity field data of flow. Fig 44 shows the basic principle of PIV technique.

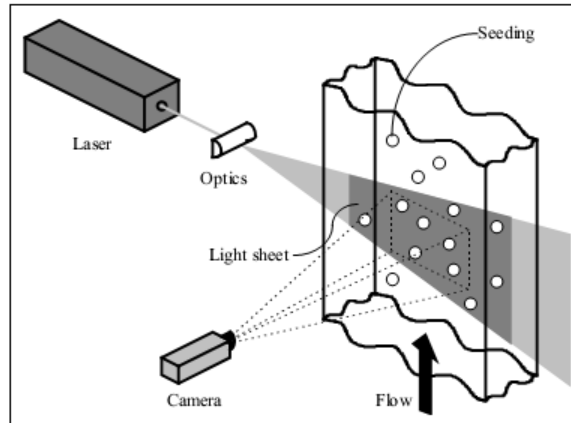


Fig 44 Basic Principle of PIV [86]

During image analysis, simply the images of the whole flow field are divided into interrogation areas (which can be seen in Fig 45) and the distance travelled by the seeding particles from the time of the first image (frame 1) to the second (frame 2) is determined. Knowing this distance travelled and the time passed, the velocity of the flow in that region is therefore measured. This is performed for each region, giving a 2-d map of the “instantaneous” velocity field at the time of the recording.

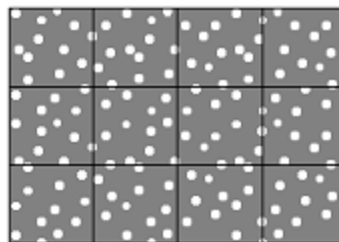


Fig 45 Interrogation areas [86]

In schematically, the measurement is based on the displacement of particles between two frames, image analysis explained above can be seen in Fig 46. This analysis will be explained in details in the following subsections.

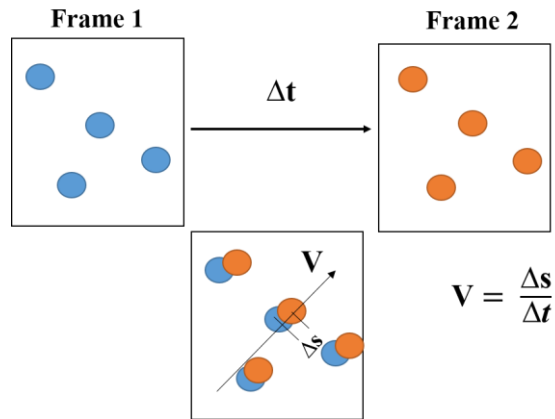


Fig 46 Image analysis (simply) [86]

To conclude it can be said that, PIV technique is based on the well-known equation as given in:

$$speed = \frac{distance}{time} \quad \text{Eqn 4}$$

In summary, a typical PIV system consists of seeding, illumination (laser), cross-correlation cameras, synchronization, correlation (processing by using software), validation and further analysis as seen in Fig 47.

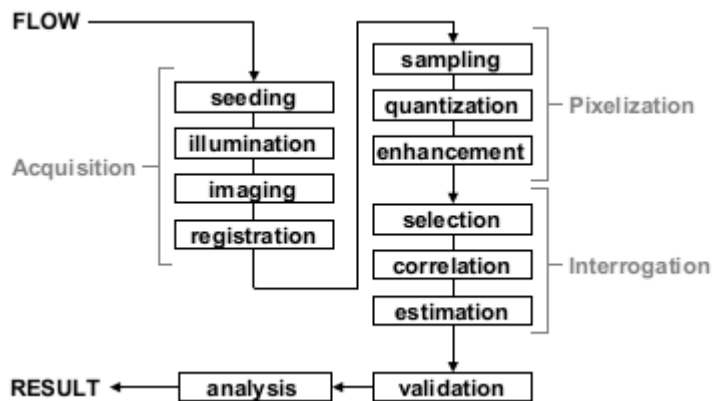


Fig 47 Flowchart of the PIV measurement and analysis process (Reprinted from Westerweel) [84]

Following sections review these components of PIV system and the steps in Fig 47 are explained in details.

3.2.2.1 Seeding

The tracer particles used in PIV technique are chosen carefully to follow the flow and provide accurate results. To select the suitable seeding, first the tracer particles should be selected by considering the interest flow, and the laser available. Then, be careful about the seeding materials must be small enough to track the fluid movement and large enough to reflect and scatter the most light for imaging. However, the particle size is limited, since too large particles cannot follow the flow properly. To summarize, particles are chosen according to [86]:

- Able to track the flow,
- Sufficient light scatterers,
- Conveniently generated,
- Cheap,
- Non-toxic, non-corrosive, non-abrasive,
- Non-volatile, or slow to evaporate,
- Chemically inactive, and
- Clean.

Therefore, different types of seeding are used depending on the nature of the flow to be investigated. When selecting the appropriate seeding particle for this study, the parameters of mean particle size, particle shape, specific gravity, surface characteristics and width of size distribution are considered.

Furthermore, Silver Coated Hollow Glass Spheres (S-HGS) which is aimed for liquid flow applications are used in this study. These are borosilicate glass particles with a spherical shape and a smooth surface. A thin silver coating further increases reflectivity. The specification of this seeding particle (S-HGS) is shown in Table 2.

Table 2 Specification of S-HGS [87]

	Mean particle size (μm)	Size distribution (μm)	Particle shape	Density (g/cm^3)	Melting point ($^{\circ}\text{C}$)	Refractive index	Material
S-HGS Silver-coated hollow glass spheres	10	2-20	Spherical	1.4	740	-	Borosilicate glass

In Fig 48, tracer particle (S-HGS) and image density of this particle in experiments carried out for this study can be seen.

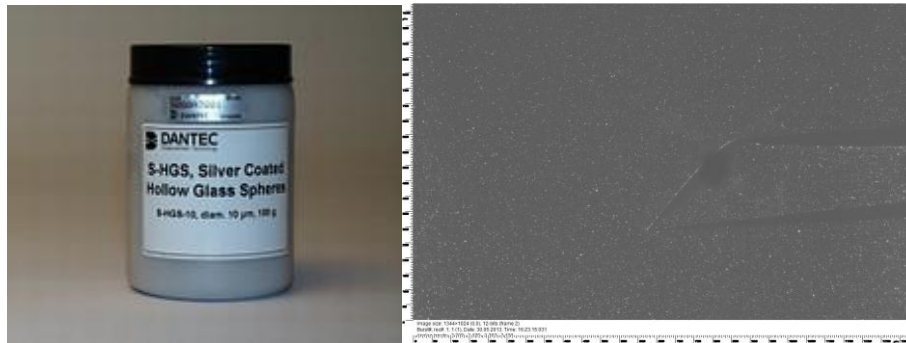


Fig 48 S-HGS [88] and image density of the particle taken from this study

Illumination step is explained in the following subsection.

3.2.2.2 Illumination

The illumination system of PIV is used for illuminating the flow field in the interest region. In the PIV technique, the light scattered by seeding materials moving in the flow field supplies a signal when it is recorded on a camera. Both the initial and final positions of the seeding particles are to be captured hence the displacement between them can be measured. Thus, the PIV illumination method should obtain the following fundamental criteria:

- The light size should be sufficiently high to ensure the intensity of scattered light from the seeding particles is such that images of them can be recorded on the PIV camera, above the optical noise level of the system,
- The endurance of the light pulse should be such that the particle does not move significantly during its exposure to the light-pulse,
- The time between successive light pulses should be such that the flow field does not move significantly,
- The location and dimensions of the measurement plane should be well-marked.

In PIV technique, there are three fundamental ways of producing a light-sheet. These are:

- By a double-cavity Q-switched Nd:YAG (neodymium-doped yttrium aluminum garnet; Nd:Y3Al5O12) laser, generation of two pulsing beams which are merged and formed into pulsing light-sheet using optics,
- By chopping a continuous wave beam from an argon-ion laser, formation of pulsing beam which is expanded into a light-sheet using optics,
- By a continuous wave beam from an argon-ion laser, generation of a pseudo-light sheet.

These illumination methods can be performed for different applications and also they have advantages and disadvantages by comparison with each other. To select the appropriate method (laser), the illumination energy density must be considered.

By using a continuous wave laser, it is impossible to provide high light intensity which is required in many PIV applications. In PIV technique, illumination is really only needed in

the short periods, when the camera is recording an image. Therefore, when most of it is actually not required, to maintain a constant high energy density would be redundant. This leads to the use of pulsed lasers such as the Nd:YAG laser, since they provide the light energy into short pulses, thereby making much better use of the energy available.

Nd:YAG PIV lasers are now being more commonly applied to the study of water flows since it offers the possibility of having the same energy size independent from the value of time between pulses.

In this study, Nd:YAG laser which provides an illumination source of sufficient energy is also used to obtain PIV images.

In Fig 49, illumination system (light source and optics) carried out for this study can be seen.



Fig 49 New Wave Solo PIV II-15, Laser Nd:YAG

The standard Solo configuration is a dual head laser with second harmonic generator body, and a room for the placement of optional attenuator. The system is given with optional items in Fig 50.

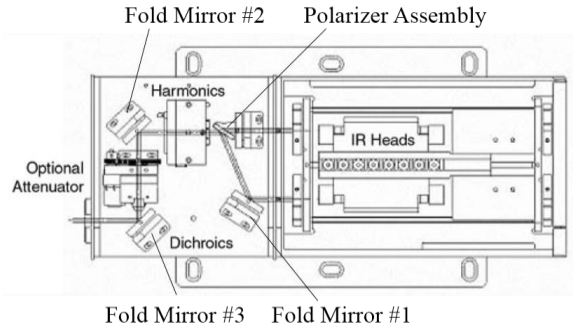


Fig 50 Laser head layout-532nm [89]

The laser includes a dual flash lamp-pumped Nd:YAG rod head in a thermally compensated resonator to generate radiation at 1064nm. In PIV applications, light in that wavelength is not suitable since most cameras get their maximum sensitivity in the blue-green part of the spectrum (~450-570nm). In addition when positioning the light sheet in the interest region, the cameras cannot see the tracer particles. Thus, the wavelength of the Nd:YAG laser is halved (532nm) by using the harmonic generator.

The resonator is very compact and, mechanically isolated from the laser housing, that makes the system relatively insensitive to vibrations and temperature change. The IR heads are placed in a separate sealed area that does not need adjustments in normal operation. The properties of Nd:YAG laser (Solo PIV II-15) used in this study is shown in Table 3.

Table 3 Specification of Solo PIV II-15 [89]

	Repetition Rate (Hz)	Energy (mJ)	Energy Stability (\pm %)	Beam Diameter (mm)	Pulse Width (ns)	Divergence (mrad)	Beam Pointing Stability (urad)	Jitter (\pm ns)
Solo II-15	15	30	4	2.5	3-5	<3	<100	1

3.2.2.3 Imaging

In PIV technique, since PIV cameras are used for capturing images of particle tracers, they are very significant parts to be selected suitable for the application. In this method, online image maps are a prerequisite to near real-time vector map processing hence CCD based recording cameras which are capable of capturing instantaneous image map of the particles are chosen. While selecting the appropriate camera, the resolution of the temporal and

spatial characteristics of the flow field, magnitude and direction of flow should be considered.

The examples of CCD cameras [86] that are currently supported as PIV cameras:

- 80C42 DoubleImage 700 camera,
- Kodak Megaplug ES1.0 camera,
- 80C60 HiSense camera.

The high-performance progressive scan interline CCD chips is used by these cameras. This chip consists of $m \times n$ light-sensitive cells and an equal number of storage cells. These are shown in Fig 51.

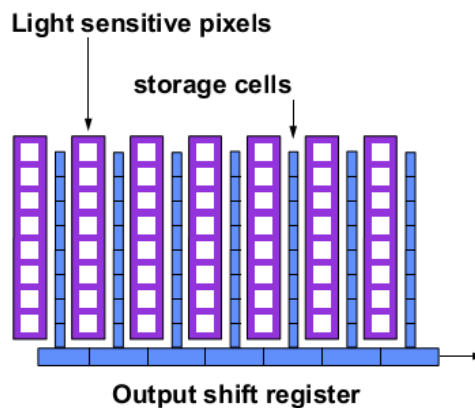


Fig 51 Schematic illustration of light-sensitive pixels and storage cells of the CCD cameras [86]

Basically, PIV camera theory can be explained as follows:

After the first image is recorded (laser pulse exposes the first frame), the charge of each pixel is moved from the light sensitive to the storage cells. Then, the second image is captured until the first image has been read out from the storage cells and is translated to the image buffer in the same way. Now, while the storage cells include the first frame, the light sensitive cells include the second. These two frames are then transferred sequentially to the digital outputs for image evaluation.

Among the features of cameras; resolution, high light sensitivity, low background noise and the high dynamic range are very significant parameters for the reasonable performance of the PIV experiments. In this study, after evaluating these parameters, HiSense MKII camera is used (Fig 52). To give an example for evaluating the parameters, when compared to Kodak ES1.0, HiSense camera in normal mode is at least 6 times more sensitive which means light size that the camera can be used in a 2x2 larger relative area. Therefore, when using the camera in the same area, the laser power required is four times less which in terms means that a much smaller and cheaper laser may be used.



Fig 52 HiSense MkII (cameras used in present study)

The specification of this camera is given in Table 4.

Table 4 Specifications of HiSense MkII [90]

	Frame rate at full resolution	Sensor resolution (pixels)	Pixel size	Min. interframe time	Peak QE	Lens Mount	Dynamic range
HiSense MkII	12.2fps	1344x1024	6.45 μ m	200ns	70%	C-mount	12bit

The cameras used in this experiment, have an objective of AF-MICRO-NIKKOR of 60 mm to maintain the flow domain and optical filters are used to block ambient light noise (Fig 53).



Fig 53 AF-MICRO-NIKKOR of 60 mm f/2.8mm and optical filter [91]

3.2.2.4 Image processing

When the images are captured successfully, it can be assumed that the images are ready for image processing. In PIV technique, to determine the displacement of tracer particles FFT (Fast Fourier Transform)/correlation techniques are performed. The images are divided into small regions called interrogation areas and by analyzing these areas of the first and second camera frames (correlation), the average displacement vector can be estimated.

Two correlation techniques can be used fundamentally for the analysis of PIV study. These are:

- Auto-correlation,
- Cross-correlation.

Basically, the determination of the degree of similarity between two images is performed by correlation. As two independent images are compared, the procedure is known as cross-correlation. And as the same image is compared to phase shifted copies of itself, the procedure is known as autocorrelation.

These techniques will be described in details in the following subsections.

3.2.2.4.1 Cross-correlation

The fundamental cross-correlation analysis is two images of flow taken from the same field in a flow separated by a time interval. Thus, the cross-correlation method can be defined as analyzing of the displacement of the tracer particles over time between the exposure of the first frame and the second. In a simplified way, cross-correlation technique can be shown as Fig 54.

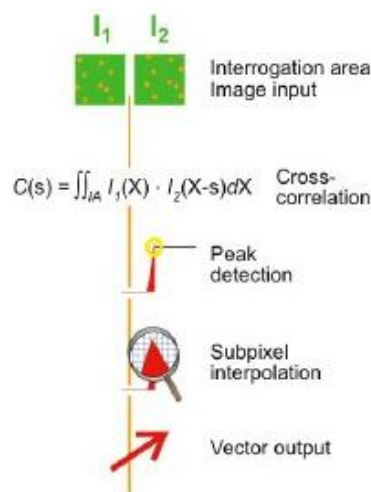


Fig 54 Cross-correlation technique [92]

Fig 54 shows that when the each light pulse is captured in separate image frames by a camera, the images recorded are divided into small regions called interrogation areas (I_1 & I_2). The interrogation areas from each frame, I_1 and I_2 , are cross-correlated with each other, pixel by pixel. This correlation analysis forms a signal peak, which identifies the common particle displacement. The displacement measurement and the velocity is obtained with sub-pixel interpolation. A velocity vector map for the whole target area is achieved by repeating the cross-correlation for each interrogation area over the two image frames captured by the camera.

Numerical processing flowchart of cross-correlation technique is shown in Fig 55.

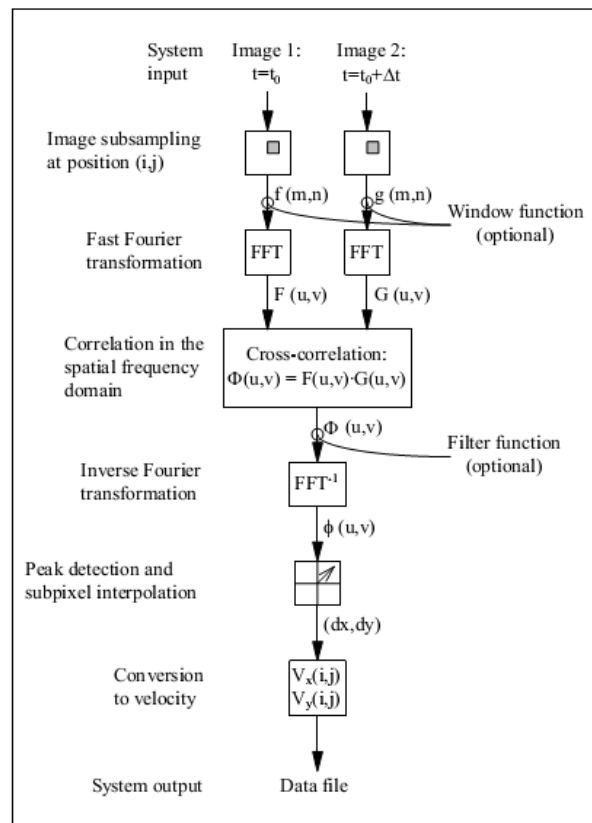


Fig 55 Numerical processing flowchart of cross-correlation technique [86]

In the Fig 55, to start image analysis, two images while one is taken at time t , second is at $t+\Delta t$, are evaluated for the system input. These images are divided into small regions (interrogation areas), this is called image subsampling at position (i,j) and results in $f(m,n)$ and $g(m,n)$ which light intensity in that interrogation area recorded at time t , and the light intensity recorded at time $t+\Delta t$ respectively. Then FFT processing is used to efficiently compute the correlation plane. $F(u,v)$ and $G(u,v)$ are the Fourier transform functions of (u,v) which are the coordinates in the spatial frequency domain. To speed up the cross correlation process in one dimensional signal processing, Fast Fourier Transforms (FFT's) are used and rather than carrying out a sum over all elements of the sampled region, the

operation can be decreased to a complex conjugate multiplication of each corresponding pair of Fourier coefficients. To obtain the cross-correlation function $\phi(u,v)$, the Fourier coefficients are inversely transformed. Final step to provide the displacement of tracer particles is peak detection and subpixel interpolation. By finding the location of highest correlation peak, the displacement can be found. However, the location peak detection will cause an uncertainty of $\pm 1/2$ pixel in the peak location. Therefore, to increase the accuracy, subpixel interpolation is performed. The ways to subpixel interpolation are three-point estimation, parabolic peak fit and peak centroid. By conversion of the displacement vector, the velocity vectors are found.

The representation of how velocity information is extracted from two images by steps explained above can be seen in Fig 56.

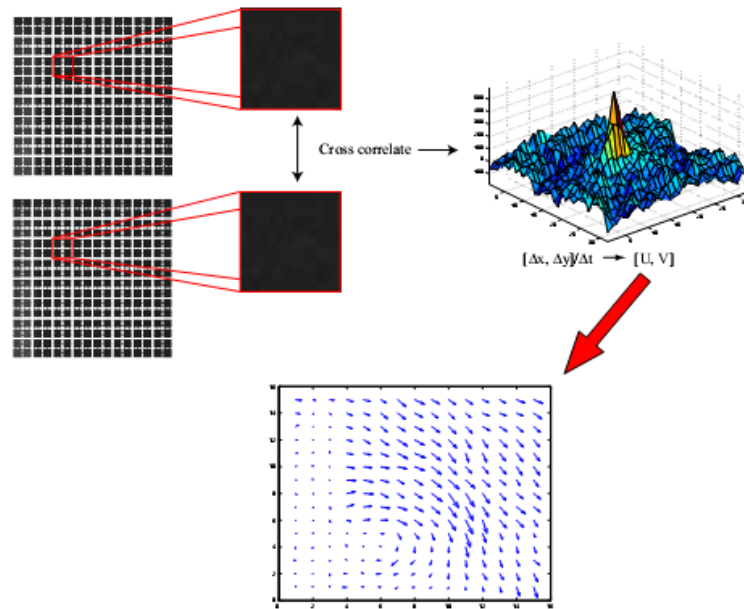


Fig 56 The illustration of how velocity information is extracted from an image pair [92]

3.2.2.4.2 Auto-correlation

Auto-correlation analysis is based on the analysis of multiple images of flow captured on a single frame. In auto-correlation technique, the first and second image so the displacement between initial and final particle cannot be correlated since only one camera frame is recorded. Instead both initial and final particle positions are captured on the same camera frame, and then the recorded image is correlated with spatially shifted versions of itself. Furthermore the calculations are similar. The auto-correlation function of multiple images has a central peak and two symmetric side peaks (Fig 57). This results in two problems:

- An uncertainty in the flow direction,
- Limiting the measurable velocity range (for very small displacements).

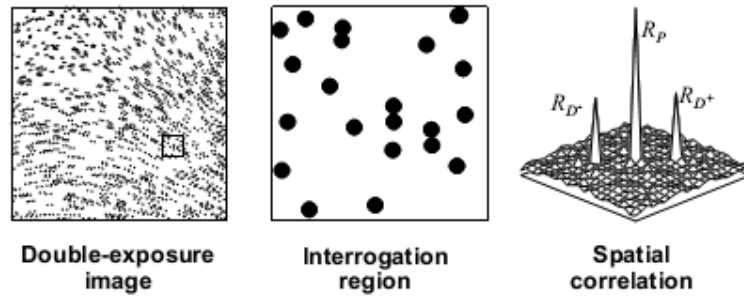


Fig 57 Auto-correlation analysis of multiple images [83]

In order to solve the uncertain flow direction problem, some techniques such as image shifting techniques using rotating mirrors and electro-optical techniques are developed. For auto-correlation analysis, larger interrogation regions are used to leave enough place for image shift added. And the uncertain flow direction problem has been overcome, by changing the place of the second image as much as the largest negative displacement. However, image shifting by rotating mirrors causes a parallax error in the velocity estimations which is as large as 11%.

To compare Cross-correlation technique and Auto-correlation technique, although auto-correlation has been the most widespread method in the past, cross-correlation is the most preferred technique in the present since it is possible to separate the initial and final particle positions on separate camera frames with new technology. Compared with auto-correlation, cross-correlation analysis is very simple and effective. The comparison of these methods can be seen briefly in Table 5.

Table 5 Auto-correlation vs Cross-correlation [94]

Auto-correlation	Cross-correlation
Single recording	Two recordings
Uncertainty in direction	No uncertainty
Problems with zero velocity	Not
Decreased spatial resolution	Not
64x64 interrogation area (suggested)	32x32 interrogation area

Among these techniques, adaptive cross-correlation method is used in this study. The main difference between the adaptive and standard cross-correlation methods, iterations are used in adaptive correlation. This method provides the capturing of “in-plane dropout” which

means that loss of particles which have left the interrogation area during the time between pulses by reducing the size of interrogation area. Therefore, signal strength increases and more successful vectors are obtained compared with standard cross-correlation.

3.2.2.5 Validation and data analysis

Validation methods are used for removing false measurements. Since PIV is an instantaneous measurement technique, all information is taken at the same time and there is a finite statistical probability that some areas include meaningless input. Thus, the validation of PIV vector map is sufficient. The software (FlowManager) used during this experiments has a validation methods based on mathematical algorithms. These are:

- Peak height ratios,
- Velocity range validation,
- Moving average,
- Manual validation,
- Masking

Validation methods recognize, reject and remove the incorrect measurements and substitute other vectors instead of wrong ones. The methods are divided into two classes. These are:

- Single point validation: Each single vector is evaluated individually by comparing with a certain velocity range.
- Whole flow field validation: All vectors in the PIV vector map or small subregion are evaluated by comparing with it neighbours.

While peak-height validation method rejects or validates individual vectors based on the values of the peak heights in the correlation plane where the vector displacement was calculated, velocity-range validation method rejects vectors, which are outside a certain range which in this method, the vectors cannot be substituted instead of the rejected vectors but by composing with another method, it is possible to be replaced the rejected vectors. The moving-average validation method rejects or validates vectors based on comparison between neighbouring vectors. And the manual vector validation method validates or rejects or vectors as outside or disabled based on the user clicking on a particular vector location.

In this study, moving average validation method, which provides that the all vectors in area have same weight and ability to set the size of the area, is used.

3.2.3 The Experimental Conditions

Before starting any of the experiments, a calibration of the whole experimental system is required. First, to provide the seeding particles spread homogeneously in water tank, the mechanism is performed a few minutes for stirring the seeding particles. Camera positioning and alignment is adjusted, means the position of camera is at 90° to the wing model placed interest region for all experiments (at the each different case of experiments, when changing the parameters of angle of attack, amplitude and the point) and then, the calibration image is taken. Also, laser alignment should be done such that the light sheet

crosses the wing model from its midspan in water tank. To ensure the periodicity of the flow around the wing model, each data of all experiments is obtained during the seventh period of motion as mentioned before.

The experimental conditions of this present study are summarized in Table 6.

Table 6 The experimental conditions of this present study

Wing model	Airfoil Type	NACA0012, NACA6412
	Chord [m]	0.06
	Span [m]	0.5
Flow	Fluid	Water
	Temperature [°C]	21
Motion	Period [s]	55(the amplitude of b) 64 (the amplitude of 2b)
Seeding particle	Type	S-HGS
	Diameter[μm]	10
	Concentration [g/cm ³]	1.4
Laser	Type	Nd:YAG
	Pulse Energy [mj/pulse]	30
Recording	Camera Type	HiSense MkII
	Number of Camera	2
	Lens Focal Length [mm]	60
	F number	2.8
	Frame Rate [fps]	12.2
	$\Delta t/T$	0.01
	Resolution [pixels]	1344x1024
	Dynamic Range [bit]	12
Exposure Delay Time[μs]	80000	
Interrogation	Method	Double Frame/Double Exposure Adaptive Cross Correlation
	Resolution	Initial: 64x64 pixels Final: 32x32 pixels each with two iterations with 50% overlap

CHAPTER 4

NUMERICAL RESULTS

The numerical study is performed for investigating the effects of some of the parameters including the angle of attack (30° and 60°), amplitude of motion in y-direction ($B=c$ and $B=2c$) and the camber (NACA0012 and NACA 6412) on the vortex formation/shedding and then these results are intended to be used for comparison with the experimental results. In addition to the present numerical study, the numerical study previously done by Başkan [10] which consists of the non-dimensional vorticity contours of NACA0012 for the cases of $B=c$ and $2c$ and for angle of attack of 45° is compared with the present experimental results.

Since the numerical cases are carried out at very low Reynolds numbers (1052) where the flow is assumed to be fully laminar, Navier Stokes equations for unsteady, incompressible flow fields are solved. This analysis is obtained with a commercially available CFD (Computational Fluid Dynamics) Package FLUENT v6.3.26.

The governing equations at zero free stream velocity (in hover) for incompressible and constant property Navier Stokes equations are described as:

$$\frac{\partial}{\partial x} U_i = 0 \quad (5)$$

$$\frac{\partial}{\partial t} U_i + \frac{\partial}{\partial x_j} U_j U_i = -\frac{1}{\rho} \frac{\partial p}{\partial x_i} + \vartheta \frac{\partial^2}{\partial x_j^2} U_i \quad (6)$$

where x_i stands for the i th component of the position vector, U_i is the velocity component in i th direction, t is the time variable, ρ is the density of the flow, p is the pressure and ϑ is the kinematic viscosity of the flow.

These equations are solved by using the second order upwind spatial discretization with SIMPLE (Semi-Implicit Method for Pressure Linked Equations) algorithm in CFD for all numerical cases and the fluid is selected as water for all numerical cases because of being same with the experiments.

A C-type structured 2-D grid domain is formed using the commercial grid generation software Gambit 2.4.6. The grid domain [96] used in the solutions includes 63000 quadrilateral cell elements and there are 256 grid points on the airfoil surface. To resolve the boundary layer, 20 grid points normal to the flow direction is placed and the first

normal grid point is located at 10^{-6} m from the airfoil surface. The boundaries of the computational grid are at 12 chords in downside direction, 8 chords in upside direction and 9 chords in downstream and upstream directions as seen in Fig 58.

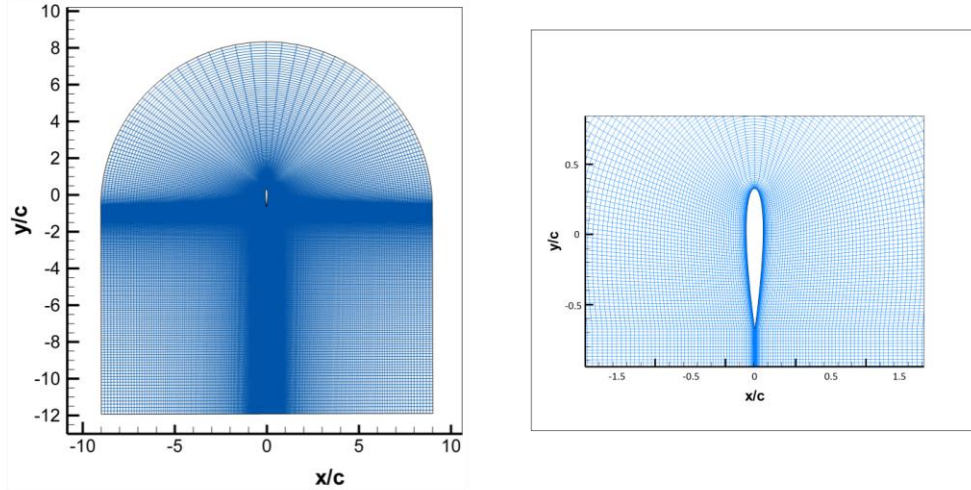


Fig 58 2-D grid domain and its distribution around the NACA0012 airfoil

The whole grid is translating with the airfoil and the outer surfaces of the grid domain is imposed as pressure-outlet boundary condition in hover mode. In all cases the airfoil surface has no-slip wall boundary condition. The information about the figure of eight motion of flapping airfoil in hover is transmitted with User Defined Functions (UDF) at each time step.

The grid size and time step are determined according to the grid and time step refinement studies of Hızlı [96]. As mentioned before, this results in the computational grid which is a C-type structured 2-D grid domain. This grid domain used in the present study has 63000 quadrilateral cell elements which is generated by Gambit 2.4.6 (grid software) and the size of grid size (cell element) is determined according to the grid independency study worked by Hızlı [96]. Three C-type 2-D structured grid domains having 63000, 128000 and 246000 cell elements are selected for the analysis in terms of C_L and C_D by Hızlı [96]. In addition to the grid independency study, the time step independency study is also carried out for four different time step sizes (Δt), 0.05s, 0.025s, 0.02s and 0.0125s, corresponding to 200, 400, 500 and 800 time-steps, over one period (T) of motion. The results for the grid independency and the time step independency studies are seen in Fig 59.

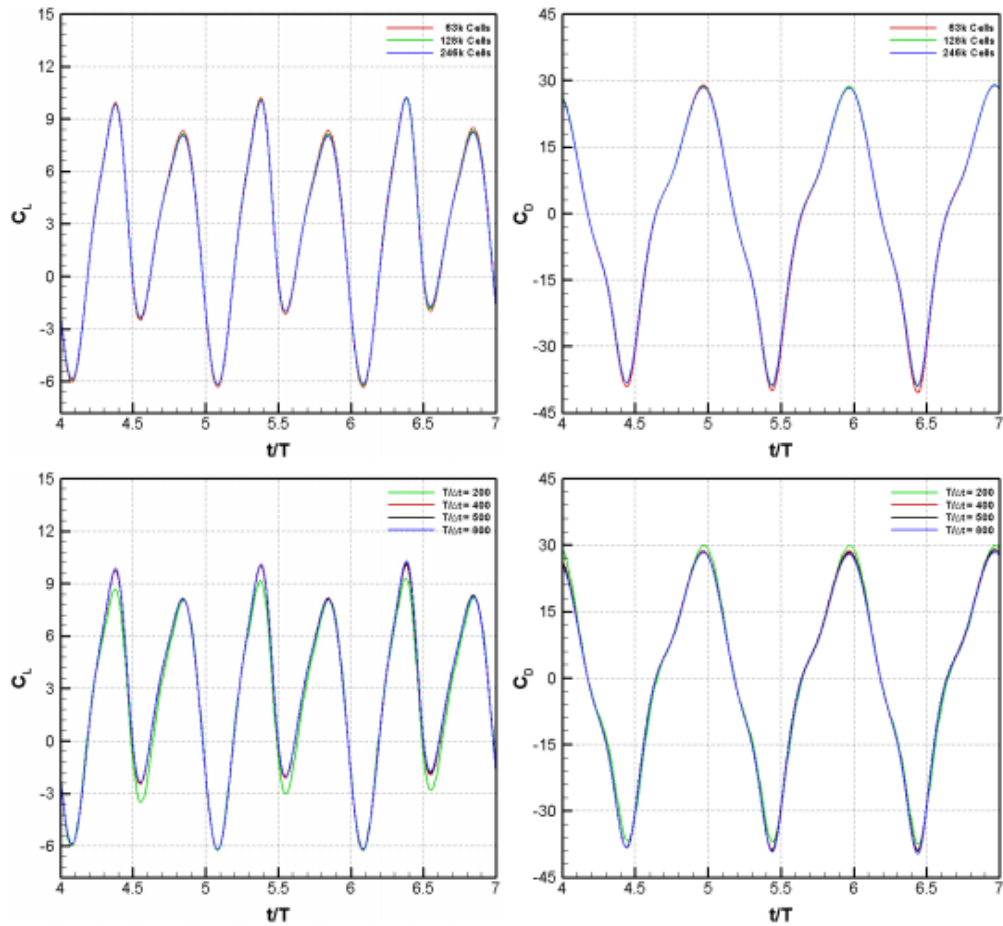


Fig 59 Time histories of lift and drag coefficients with different grids (top) and with different time- steps for NACA0012 airfoil over three periods of motion [96]

From the results of this study, since there are not significant differences between the grids having 63000 cell elements and 128000 cell elements, it is concluded that the grid size 63000 is good enough for comparing the experimental results and 400 time-step size is chosen which corresponds to 2000 over one period (T) of motion for this study is used. The numerical studies are performed on a quad-core personal computer having an Intel Core i7 processor of 2.67 GHz of CPU speed and 4 GB of RAM. For one case, about 17 hours of CPU time is spent for the calculation of 16000 iterations for a grid domain having 63000 elements and $T/\Delta t=2000$ in other words 8 period of motion is analyzed by using code FLUENT v6.3.26 as the solver.

The numerical cases determined to compare the experimental study are given in Table 7.

Table 7 The cases for numerical studies

Point	NACA0012		NACA6412		
	$\alpha=30^\circ$		$\alpha=60^\circ$	$\alpha=30^\circ$	
	B=c	B=2c	B=c	B=c	B=2c
1	√	√	√	√	√
2	√	√	√	√	√
3	√	√	√	√	√
4	√	√	√	√	√
5	√	√	√	√	√
6	√	√	√	√	√
7	√	√	√	√	√
8	√	√	√	√	√

In numerical study, flow starts plunging from right to left (downstroke) and continues its motion with upstroke (1.region), then the flow plunges from left to right (2. region) and again continues its motion with upstroke (3.region). This flow description and the 8 different points analyzed in numerical study can be seen in Fig 60. To obtain the periodicity of the flow around the airfoil, the cases for numerical studies are performed during 7th period of flapping motion and the non-dimensional time $t/T=1$ corresponds to the starting point of the motion at the beginning of seventh period.

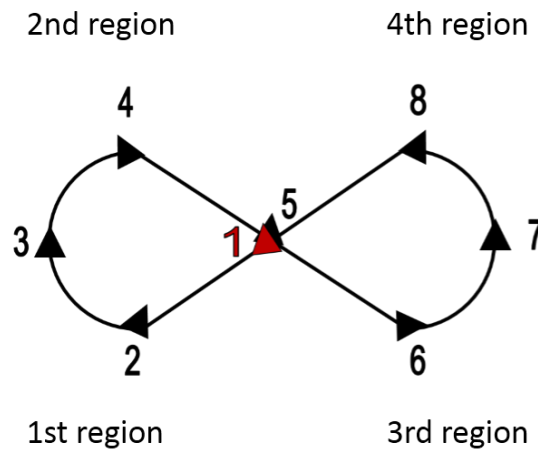


Fig 60 The flow schema

4.1 Effects of Vertical Amplitude of the Motion

The numerical studies for two different amplitude values ($B=c$ and $B=2c$, where B is given in Eqn 2, Fig 10) are performed to observe the effects of amplitude of motion. As given in Table 7, this analysis is carried out for two different angles of attack (30° and 60°). However, only the cases for NACA 0012 and NACA6412 with the initial angle of attack of 30° are presented in the current study for brevity. For these cases, time histories of the aerodynamic lift and drag coefficients versus the vertical amplitude of the figure of eight flapping motion obtained from the 2-D CFD results for NACA0012 and NACA6412 are plotted in Figures 61 and 62.

The highest and lowest lift coefficients occur between the 4th and 5th point of motion and between the 3rd and 4th point of motion, respectively. These points of motion corresponds to the translational and rotational phases as seen in Fig 60. Also, in one period of motion there are two positive and two negative peaks in time histories of the lift coefficient curves. It is observed that while the positive peaks occur at the translational phase, the negative peaks occur at the rotational phase of the motion.

To evaluate the minimum and maximum values of lift coefficient, the minimum values are obtained while the airfoil is translating in the upward direction with a relatively small horizontal velocity. The maximum values of lift coefficient are attained while the airfoil is moving with a constant angle of attack, constant x velocity and a negative y velocity. It is also observed that there is an increase in lift coefficient for $B=2c$ case when compared with $B=c$ case. The reason for this increase is attributed to the lack of interaction between the recently formed trailing edge vortex and the counter-rotating trailing edge vortex which is formed and shed during the previous stroke (Fig 61).

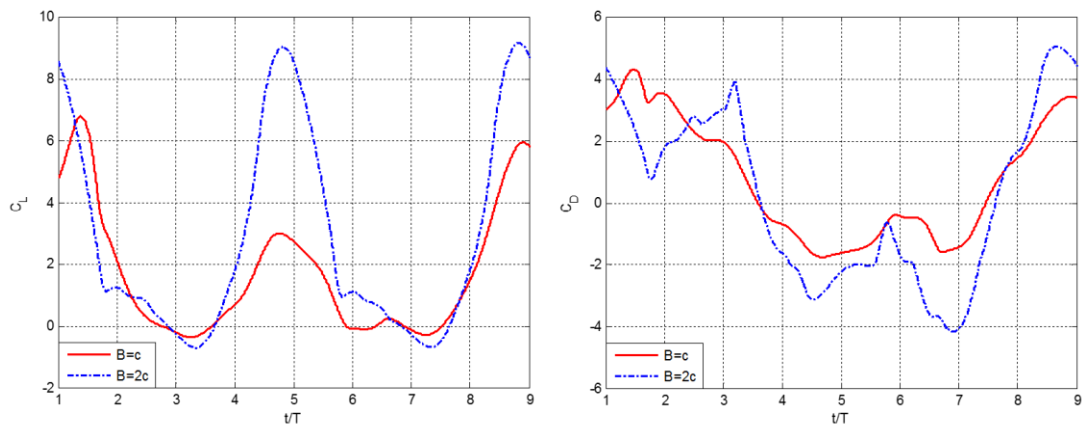


Fig 61 Time histories of the aerodynamic lift and drag coefficients versus the vertical amplitude of the figure of eight flapping motion for NACA 0012 with $\alpha=30^\circ$ and $B=c$, $B=2c$

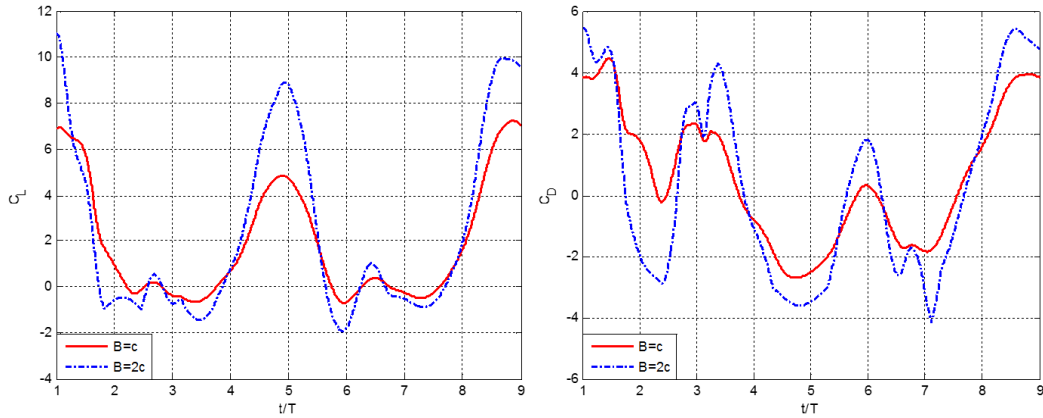


Fig 62 Time histories of the aerodynamic lift and drag coefficients versus the vertical amplitude of the figure of eight flapping motion for NACA 6412 with $\alpha=30^\circ$ and $B=c$, $B=2c$

The highest and lowest drag coefficients occur between the 3rd and 4th point of motion and between the 4th and 5th point of motion, respectively. Again, these points of motion correspond to the rotational and translational phases as seen in Fig 60. Also, just the opposite of the lift coefficient, there are two positive and two negative peaks in the time histories of the drag coefficient curves. It is observed that while the positive peaks occur at the rotational phase, the negative peaks occur at the translational phase of the motion. Therefore, it can be said that same type of vortex interaction mechanism is responsible for providing the minimum and maximum drag coefficients.

To evaluate the minimum and maximum values of drag coefficient, the minimum values occur since the leading and trailing edge vortices create a suction region in the opposite direction of motion. And the maximum values of drag coefficient are obtained while the airfoil is moving in the vertical direction. In this situation, the drag coefficient increases in positive direction.

The variation of lift and drag forces during a period of figure of eight flapping motion for both NACA 0012 and NACA 6412 airfoils at $\alpha=30^\circ$ and $B=c$, $B=2c$ are presented in Fig 63. As mentioned before, the maximum and minimum values for the lift and the drag forces are obtained for the case of $B= 2c$. The reason for having the maximum lift and drag for the case of $B=2c$ can be due to the formation of massive leading and trailing edge vortices and the lack of interaction between the recently formed and the previously formed vortices as the amplitude of motion is increased.

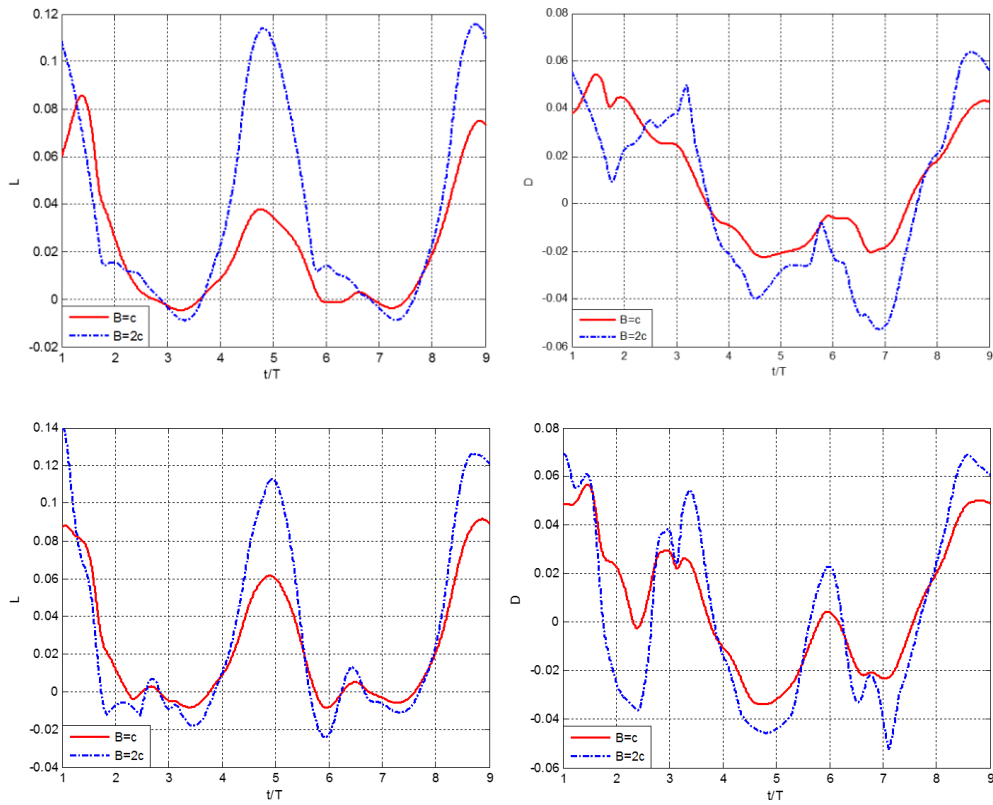


Fig 63 Lift and drag versus the the vertical amplitude of the figure of eight flapping motion for NACA0012 (top) and NACA6412 (bottom) with $\alpha=30^\circ$ and $B=c$, $B=2c$

L/D ratio for NACA0012 and NACA6412 with $\alpha=30^\circ$, $B=c$ and $B=2c$ are obtained from Fig 65 and is given in Fig 66. A higher L/D ratio is obtained between the third and the fourth points and between the seventh and the eighth points which correspond to the positions of translational phases for both of the airfoils. The extremely large values observed for the L/D ratios are due the zero crossing values of the drag coefficient during the motion. When the lift value is divide by zero and infinitely large value for the L/D ratio is obtained.

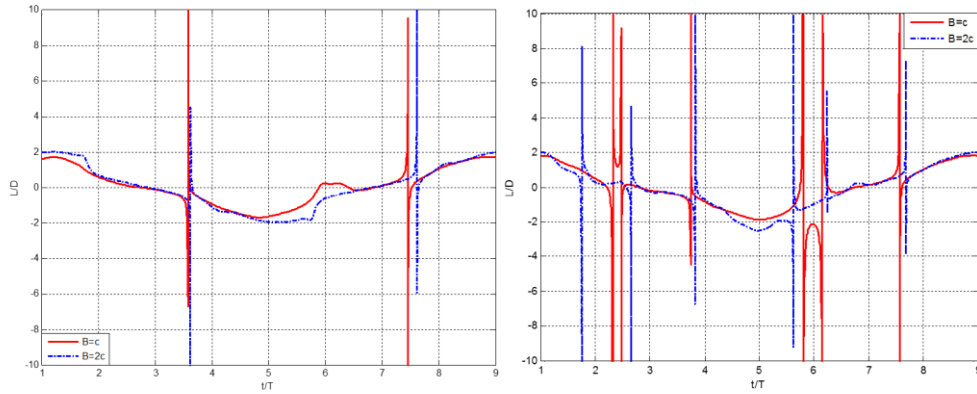


Fig 64 L/D ratio versus the the vertical amplitude of the figure of eight flapping motion for NACA 0012 (right) and NACA6412 (left) with $\alpha=30^\circ$ and $B=c, B=2c$

Fig 64 shows the variation of L/D ratios versus the amplitude of the figure of eight flapping motion for NACA 0012 (right) and NACA6412 (left) with $\alpha=30^\circ$ and $B=c, B=2c$.

Figures 65 and 66 present the sequence of images captured at different points along the flapping motion of the airfoils during a period. From these images one can easily interpret the vortex shedding mechanism as:

- for 1st region of the motion ($1 < \text{point} < 3$), it can be said that while the leading edge vortices are rotated in clockwise direction, the trailing edge vortices are generated in counterclockwise direction. These vortices translate with the airfoil and the trailing edge vortices in counterclockwise direction extend and interact with the leading edge vortices. Therefore, the strength of trailing edge vortices decrease.
- In the second region ($3 < \text{point} < 5$) after the airfoil reaches the maximum angle of attack, the leading edge vortices are rotating in CCW direction and as the airfoil moves in a vertical direction, the leading edge vortices extend over the airfoil and the strength of the trailing edge vortices have increased which is formed in the 2nd region.
- Same vortex formation and interaction mechanism is apparent in the 3rd and 4th regions of the motion.
- As the amplitude of flapping motion is increasing, the interaction between the vortices which are formed in the 1st and 2nd region of the motions deteriorates. The absence of interaction between the vortices results in the formation of stronger leading and trailing edge vortices which contribute significantly to the generation of lift.

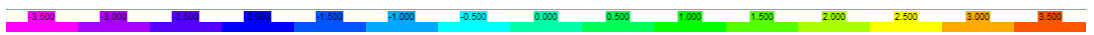
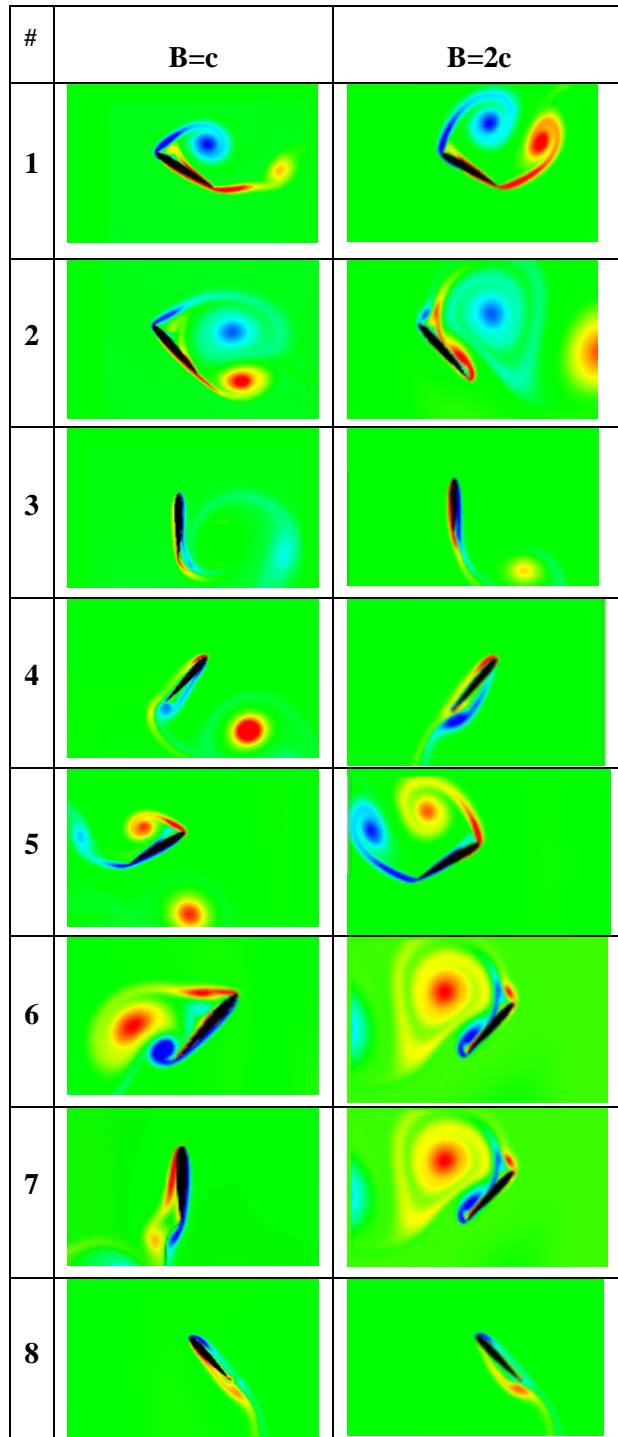


Fig 65 Instantaneous vorticity contours of NACA 0012 during the 7th period for $\alpha=30^\circ$, B=c, B=2c and Re=1052

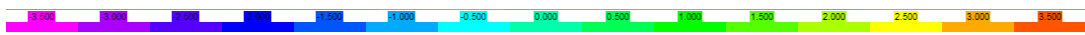
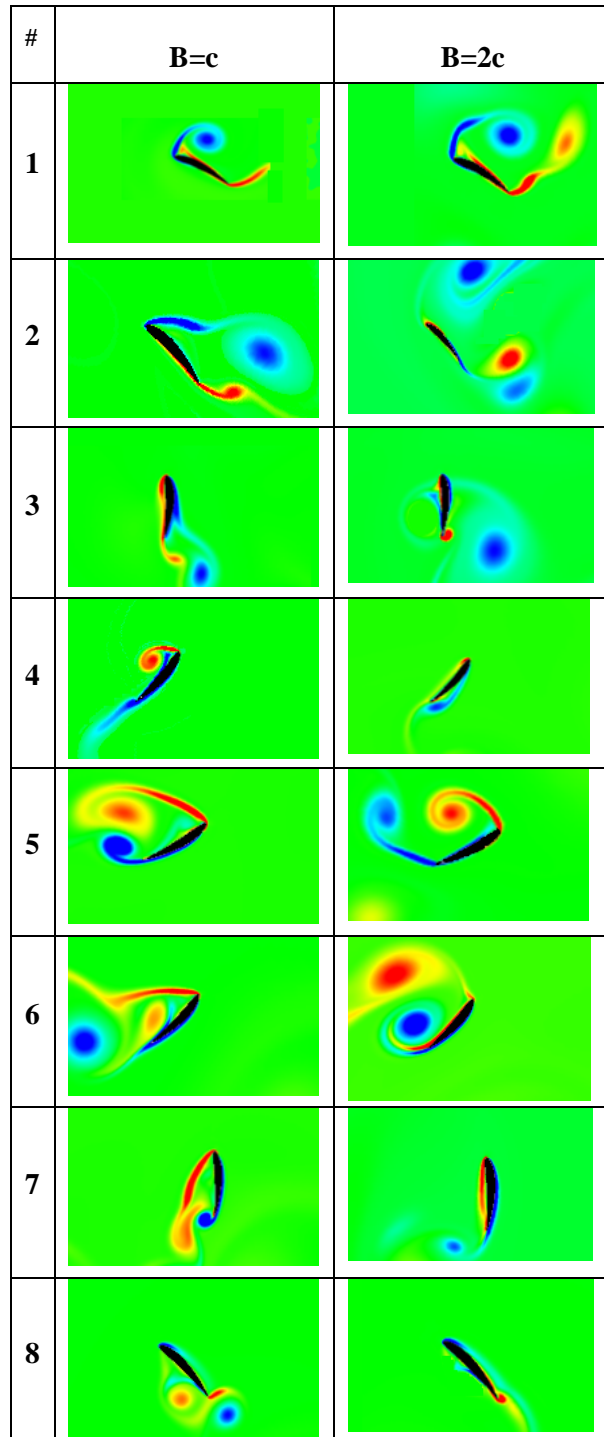


Fig 66 Instantaneous vorticity contours of NACA 6412 during the 7th period for $\alpha=30^\circ$, $B=c$, $B=2c$ and $Re=1052$

4.2 Effects of Initial Angle of Attack

The second parameter investigated in this study is the initial angle of attack for the airfoils investigated. The numerical study is performed for two different initial angles of attack, 30° and 60° . Although the calculations were carried out for two different amplitudes and for two different airfoils for each initial angle of attack, only the results for NACA 0012 with $B=c$ are given in Fig 67. Also, the instantaneous vorticity contours of NACA 0012 during the 7th period for $\alpha=30^\circ$, 60° and $B=c$ are given in Fig 68.

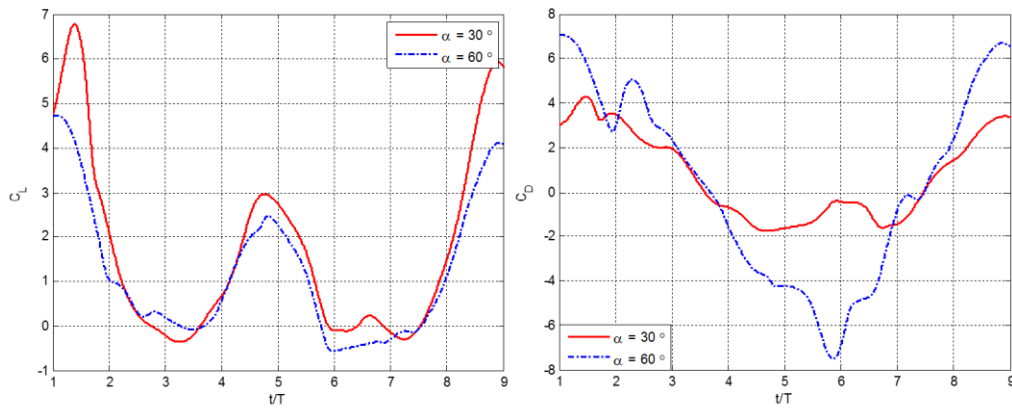


Fig 67 Time histories of the aerodynamic lift and drag coefficients versus the initial angle of attack ($\alpha=30^\circ$, $\alpha=60^\circ$.) for NACA 0012 and $B=c$

During the rotational phase, the higher rotational velocity plays a significant role for obtaining larger lift coefficients. Hence, as seen in Fig 67, the minimum lift coefficient is provided for $\alpha=30^\circ$ because of the increased rotational velocity. Since the increased rotational velocity causes the formation of a suction region near the trailing edge which increases the strength of the trailing edge vortex, the presence of which effect the previously formed leading edge vortex. For other cases the previously formed leading edge vortex is elongated and convected towards the downwards direction. These effects cause a reduction in mean lift coefficient. During the translational phase, since the airfoil surface which faces the flow is increased for a smaller angle of attack, which in turn increases the lift coefficient. For the drag coefficient, because of the relatively massive leading and trailing edge vortices placed on the opposite side of the motion, a decrease in drag coefficient is observed.

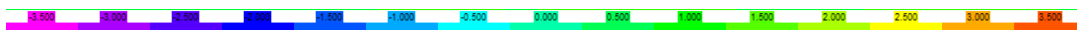
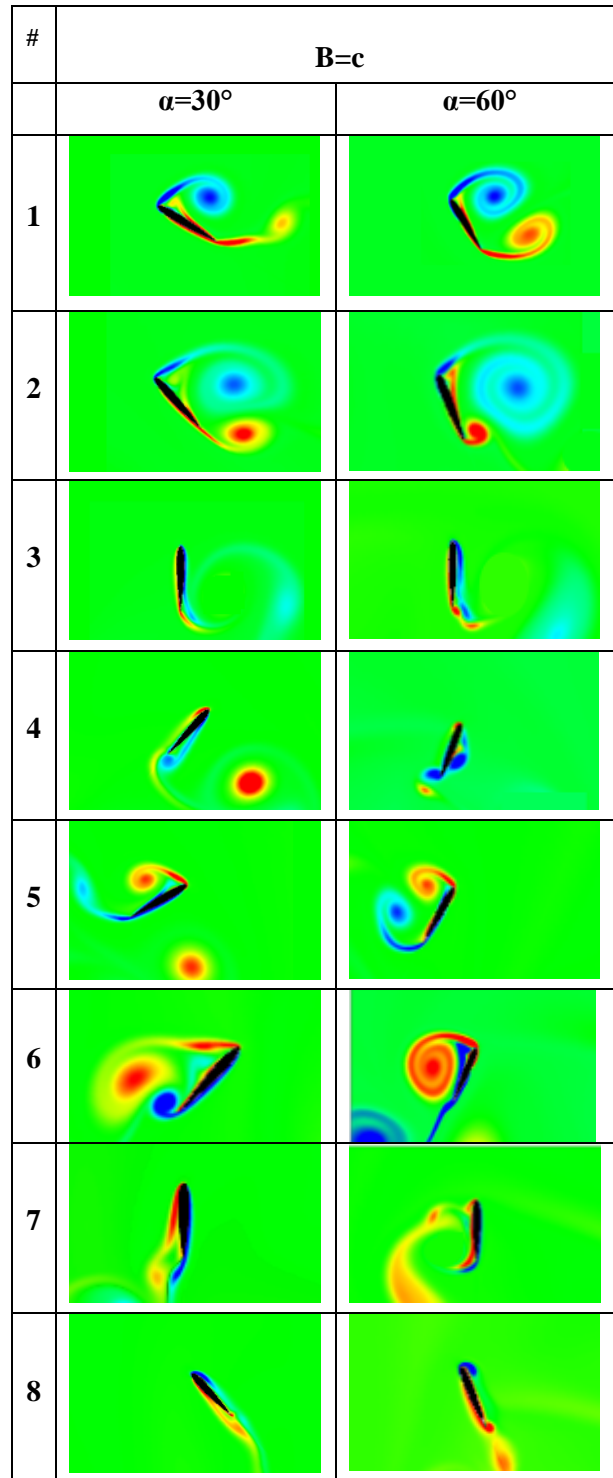


Fig 68 Instantaneous vorticity contours of NACA 0012 during the 7th period for $\alpha=30^\circ$, $\alpha=60^\circ$ and B=c, Re=1052

4.3 Effects of Airfoil Profile Shape

The last parameter investigated for numerical study is the airfoil profile shape, for this investigation two airfoil profiles, NACA0012 and NACA6412 are used. Fig 69 shows the lift and drag coefficients for NACA 0012 and NACA 6412 airfoil profiles for $B=2c$, $\alpha=60^\circ$. To compare the airfoil profiles as seen in Fig 69, the results show that there is not much difference for minimum and maximum aerodynamic force coefficient values of NACA0012 and NACA6412 airfoils. The observation shows that while the positive peak values of lift coefficients are higher for the symmetric (NACA 0012) profile in downstroke, the drag coefficients are higher for cambered (NACA 6412) profile in the upstroke. In downstroke lower surface of the cambered airfoil becomes the upper surface and this results in additional pressure increment on the suction side of the airfoil and lower vertical force coefficient values.

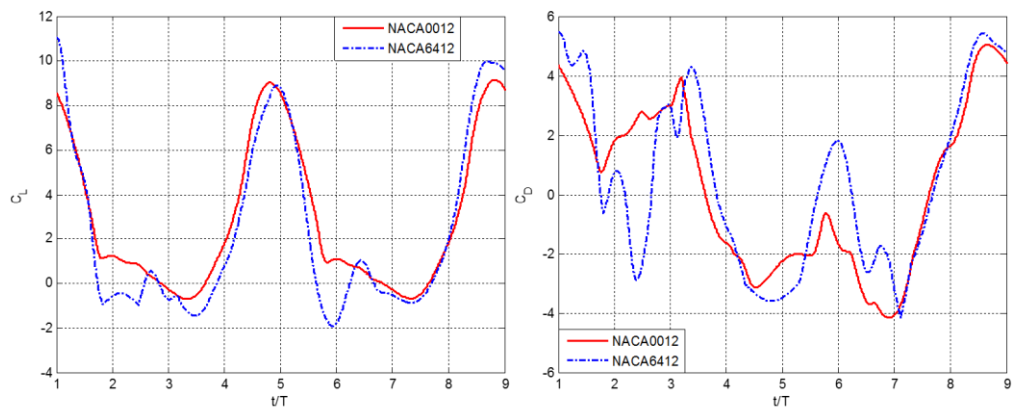


Fig 69 Time histories of the aerodynamic lift and drag coefficients for NACA 0012& NACA 6412 airfoil profiles for $B=2c$, $\alpha=60^\circ$

CHAPTER 5

EXPERIMENTAL RESULTS

In this chapter, the experimental results of the figure of eight flapping motion in hover carried out for analyzing the effect of different parameters on the vortex shedding mechanism are discussed and the results are compared with the previous study ([10]) and the present numerical study.

In the experiments as in the numerical studies, flow starts plunging from right to left (downstroke) and continues its motion with upstroke (1.region), then the flow plunges from left to right (2. region) and again continues its motion with upstroke (3.region). This flow description and the 8 different points analyzed in the experiments can be seen in Fig 60. To obtain the periodicity of the flow around the airfoil, the experiments are performed during the 7th period of flapping motion and the non-dimensional time $t/T=1$ corresponds to the starting point of the motion at the beginning of the seventh period.

The different parameters investigated in the experiments are the amplitude of the figure of eight flapping motion (B), the initial angle of attack (α) and the shape of the airfoil. The test cases for investigating the effect of these parameters are given in Table 8. The PIV experiments are performed for two different airfoils, NACA0012 and NACA6412, and as seen in Table 8, 48 experiments are performed and analyzed only for one airfoil shape.

Table 8 Test cases for the airfoil

Point	$\alpha=30^\circ$		$\alpha=45^\circ$		$\alpha=60^\circ$	
	B=c	B=2c	B=c	B=2c	B=c	B=2c
1	√	√	√	√	√	√
2	√	√	√	√	√	√
3	√	√	√	√	√	√
4	√	√	√	√	√	√
5	√	√	√	√	√	√
6	√	√	√	√	√	√
7	√	√	√	√	√	√
8	√	√	√	√	√	√

5.1 NACA 0012 airfoil in figure of eight motion pattern in hover

To analyze the effects of some parameters, the experiments are performed for NACA0012 airfoil first. In this section, the experimental results of NACA0012 airfoil with different amplitudes for the figure of eight flapping motion and different initial angles of attack are discussed. First, the numerical results and the experimental results of the instantaneous vorticity contours for NACA 0012 during the 7th period for $\alpha=30^\circ$, $B=c$ and $B=2c$ are compared (Fig 71). Then, the numerical results previously obtained by Başkan [10] and the experimental results of the present investigation are compared in terms of the instantaneous vorticity contours for NACA 0012 airfoil during the 7th period for $\alpha=45^\circ$, $B=c$ and $B=2c$ (Fig 72).

In Fig 71, the experimental results and the numerical results for the 7th period of flapping motion are compared for two different amplitudes of figure of eight motion at $\alpha=30^\circ$. As stated before, the vortex shedding mechanism (Fig 71) can be explained as,; for 1st region of the motion (1<point<3) it can be said that while the leading edge vortices are rotated in clockwise direction, the trailing edge vortices are generated in counterclockwise direction. These vortices translate with the airfoil and the trailing edge vortices which rotate in counterclockwise direction extend and interact with the leading edge vortices. Therefore, the strength of the trailing edge vortices is decreased. In the second region (3<point<5) after it reaches the maximum angle of attack, the leading edge vortices are formed in CCW direction and as the airfoil moves in a vertical direction, the leading edge vortices extend over the airfoil and the strength of the trailing edge vortices are increased which is formed in the 2nd region. Same vortex formation and interaction mechanism is apparent in the 3rd and 4th regions of the motion. This fact can easily be seen in Fig 70.

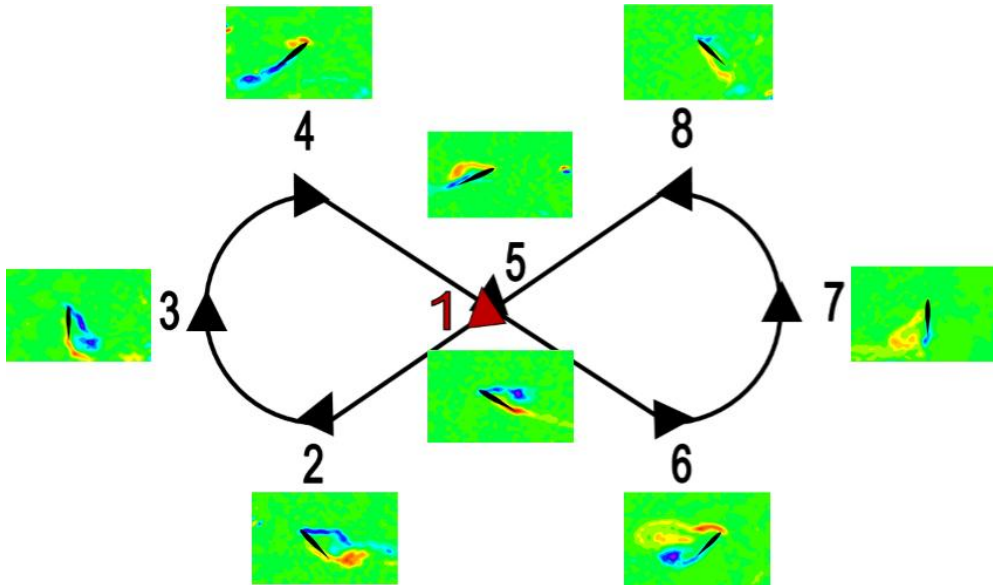


Fig 70 The flow schema of NACA0012 for $\alpha=30^\circ$, $B=c$ and $Re=1052$

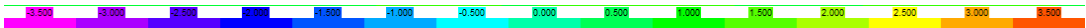
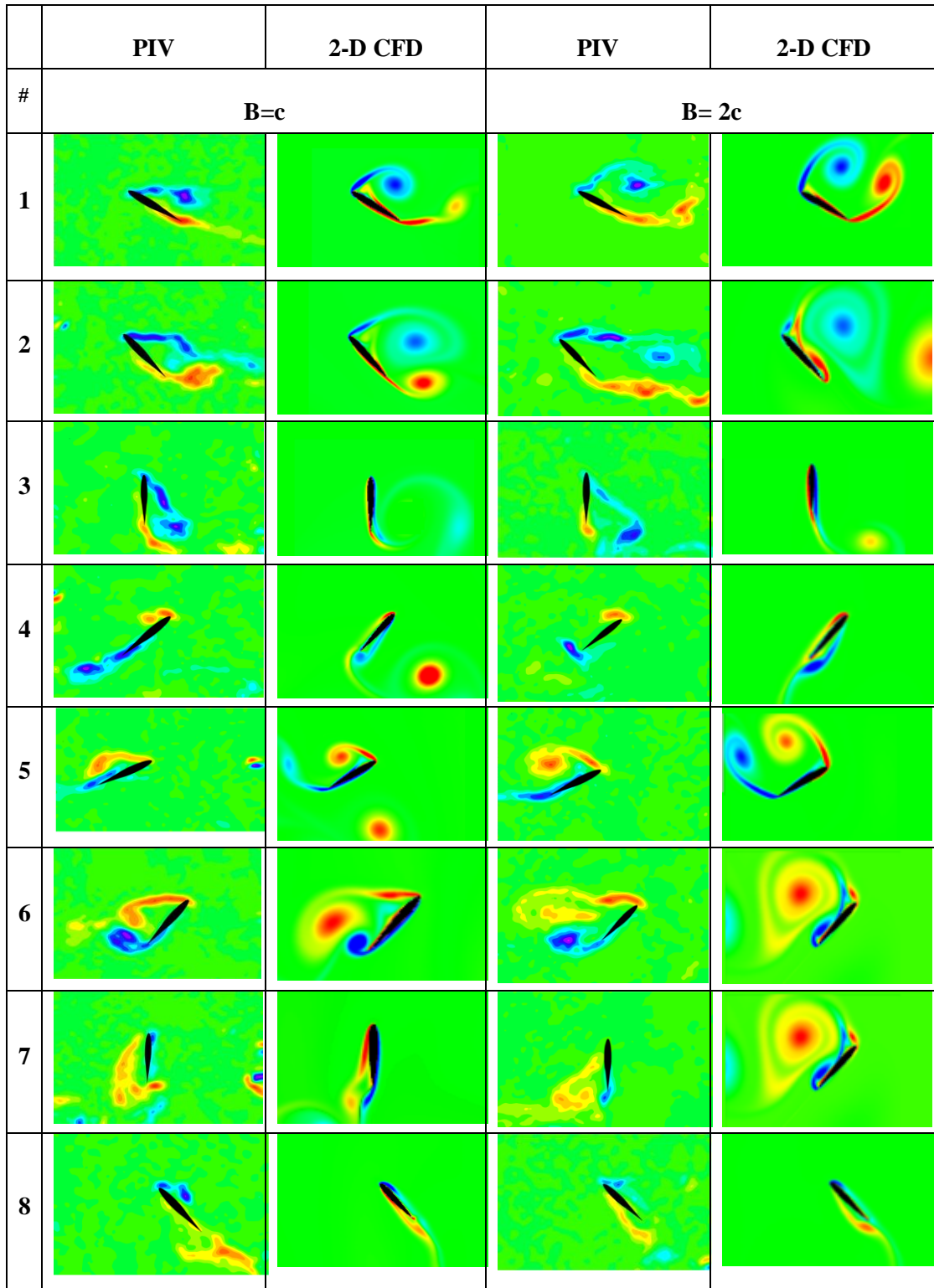


Fig 71 Instantaneous vorticity contours of NACA 0012 during the 7th period for $\alpha=30^\circ$, B=c, B=2c and Re=1052

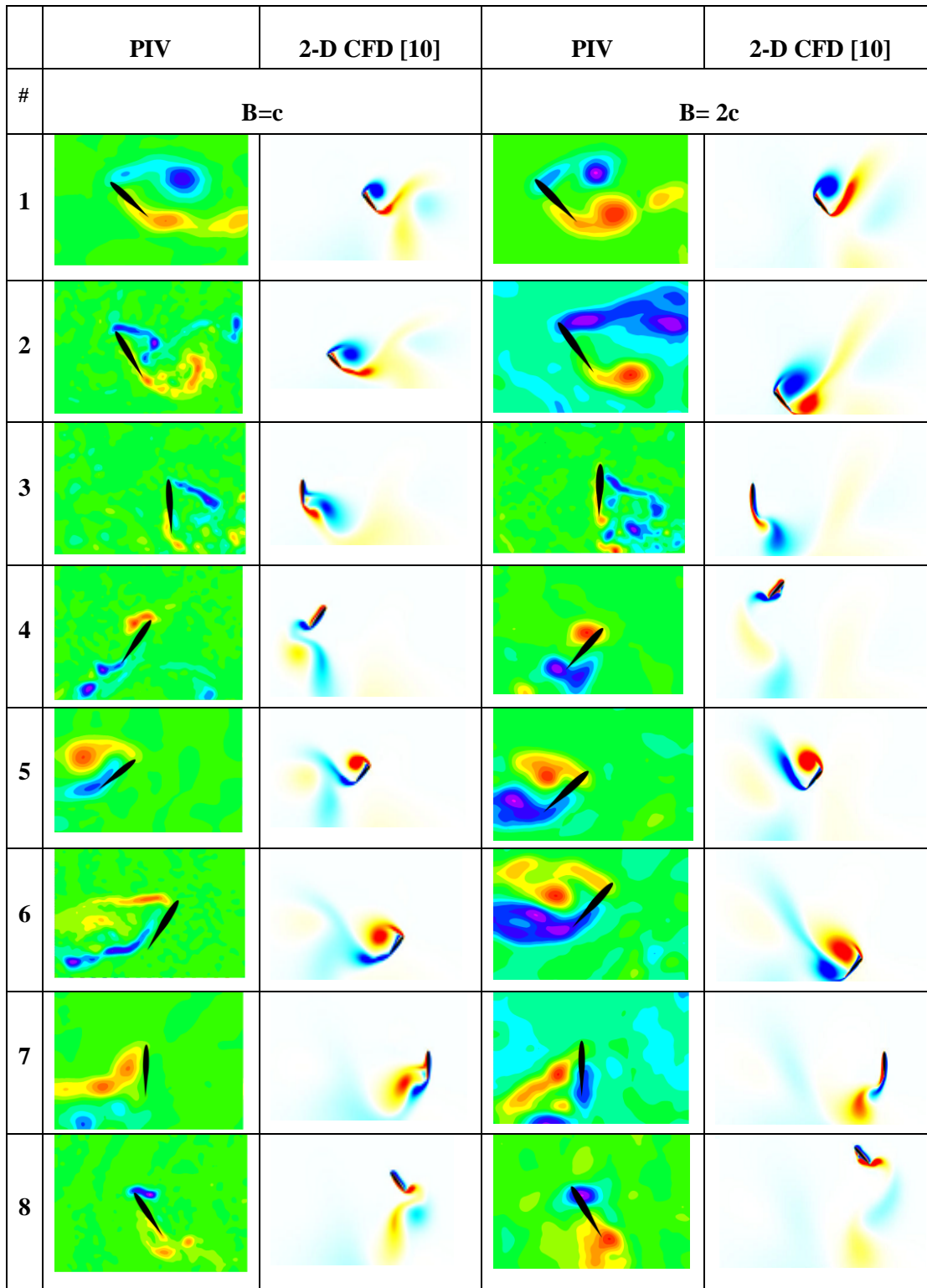


Fig 72 Instantaneous vorticity contours of NACA 0012 during the 7th period for $\alpha=45^\circ$, $B=c$, $B=2c$ and $Re=1052$

To compare the experimental and numerical results, the formation of the leading edge vortices and the trailing edge vortices are closer for the present numerical results than the previous numerical results done by Başkan. For the present numerical results when compared with the experimental (PIV) results (Fig 71), it is observed that the vortices which remain from the previous stroke and the vortices that are formed during the present stroke interact with each other and this interaction can dominate the flow field. As an example, the vortices remaining from the previous stroke can easily be seen in Fig 71 for points 4 and 5. Comparing the previous numerical results performed by Başkan and the experimental PIV results (Fig 72), the size of leading and trailing edge vortices is a bit different since the fluid was selected to be air for the numerical solutions whereas water is used for the experiments. However, the formation of leading edge and trailing edge vortices and their interactions are validated with the experimental results. From the comparison it can be said that the interaction between the vortices which are formed in the 1st and 2nd regions of the motion becomes weaker in the case of $B=c$ when compared to the case of $B=2c$. Because of this fact, the leading and trailing edge vortices become stronger which results in higher lift.

The experimental results for different amplitudes of the flapping motion, $B=c$ and $B=2c$, at 30° , 45° and 60° are given in Appendix A.

The second parameter investigated in this study is the initial angle of attack of the airfoil. The experiments are performed for three different initial angles of attack, 30° , 45° and 60° . The comparison of the experimental results with the numerical results, were done for NACA0012, and for $\alpha=60^\circ$ and $B=c$. The instantaneous vorticity contours obtained from the experiments and the numerical studies for NACA0012 airfoil with initial angle of attack of 30° and 60° for $B=c$ are given in Fig 73. As seen in Fig 73, the leading edge and trailing edge vortices are stronger for $\alpha=60^\circ$ than for $\alpha=30^\circ$ case. Therefore, it can be said that the massive vortices are generated at higher angles of attack.

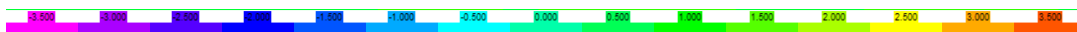
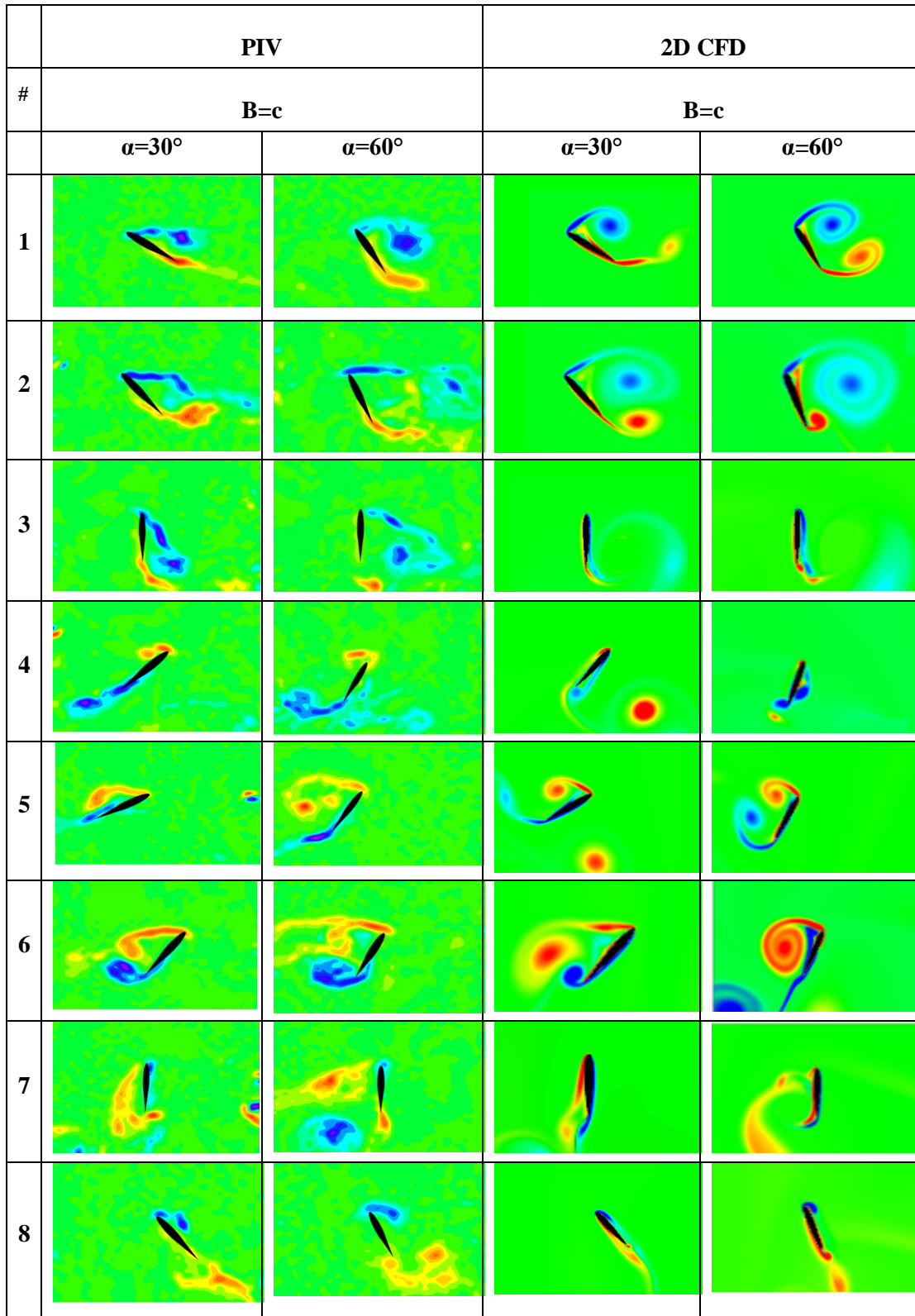


Fig 73 Instantaneous vorticity contours of NACA 0012 during the 7th period for $\alpha=30^\circ$, $\alpha=60^\circ$ and B=c, Re=1052

5.2 NACA6412 airfoil in figure of eight pattern in hover

Finally, the same experiments and numerical studies are performed for NACA6412 airfoil (cambered airfoil) with changing the values of the same parameters as mentioned before for NACA0012 (symmetric airfoil) case. First, the effect of amplitude of the figure of eight flapping motion is analyzed. Again, this analysis is performed for two cases, $B=c$ and $B=2c$, where B is given in Eqn 2, Fig 10.

In Fig 75, the instantaneous vorticity contours obtained from the experiments and numerical studies for NACA6412 airfoil with initial angle of attack of 30° for $B=c$ and $B=2c$ are presented. The vortex shedding mechanism can be explained in the same manner as we have done for the NACA0012 airfoil. As seen in Fig 75, for the 1st region of the motion ($1 < \text{point} < 3$), while the leading edge vortices are rotated in clockwise direction, the trailing edge vortices are generated in counterclockwise direction. These vortices translate with the airfoil and the trailing edge vortices which rotate in counterclockwise direction extend and interact with the leading edge vortices so that the strength of trailing edge vortices are decreased. In the second region ($3 < \text{point} < 5$), the leading edge vortices are formed in counterclockwise direction and as the airfoil moves in a vertical direction, the leading edge vortices extend over the airfoil and the strength of the trailing edge vortices are increased which are formed in the 2nd region. Same vortex formation and interaction mechanism is apparent in the 3rd and 4th regions of the motion. Fig 74 shows this fact.

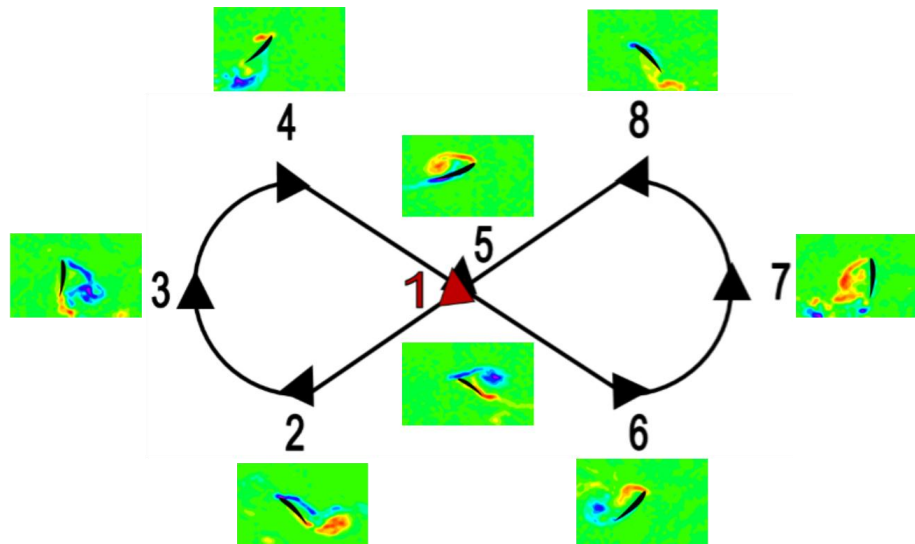


Fig 74 The flow schema of NACA6412 for $\alpha=30^\circ$, $B=c$ and $Re=1052$

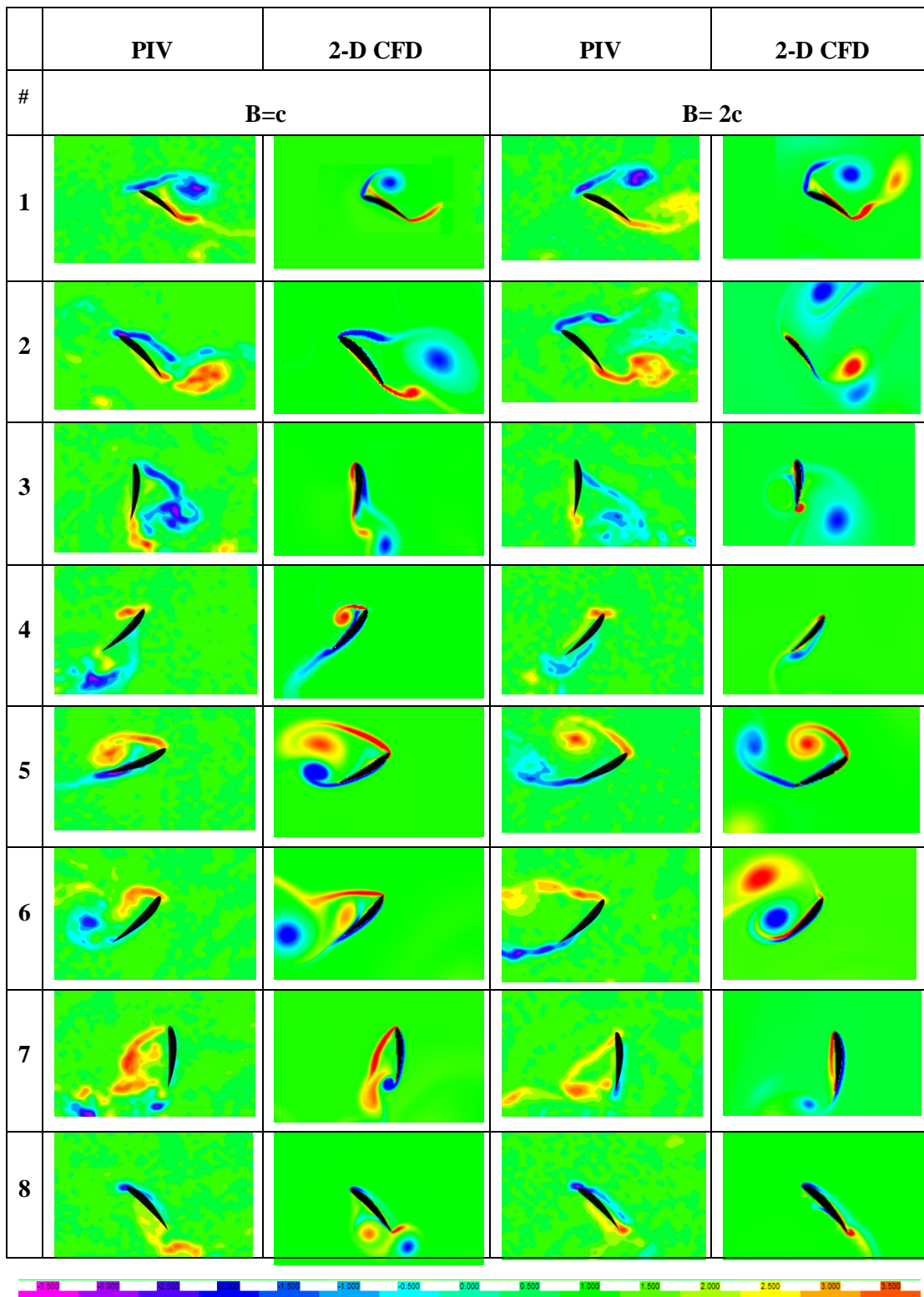


Fig 75 Instantaneous vorticity contours of NACA 6412 during the 7th period for $\alpha=30^\circ$, B=c, B=2c and Re=1052

When we compare the experimental and numerical results, we observe that the formation of leading edge vortices and trailing edge vortices are similar. Therefore it can be concluded that the formation of leading edge and trailing edge vortices and their interactions are validated with the experimental results.

Further experimental results obtained for different amplitudes of flapping motion, $B=c$ and $B=2c$, and different angles of attack 30° , 45° and 60° are given in Appendix A.

The other important parameter that is investigated in this study is the initial angle of attack. The experiments are performed for three different initial angles of attack, 30° , 45° and 60° . The instantaneous vorticity contours obtained from the experiments of NACA6412 airfoil with initial angle of attack of 30° and 60° for $B=c$ are given in Fig 76. The leading edge and trailing edge vortices are stronger for $\alpha=60^\circ$ case than $\alpha=30^\circ$ case as seen in Fig 76 and it can be said that the massive vortices are generated at higher angles of attack. In summary, the effect of the initial angle of attack for NACA6412 is same as for NACA0012 airfoil. Therefore, the conclusion for NACA0012 airfoil in subsection 5.1 is acceptable for NACA6412 airfoil as well.

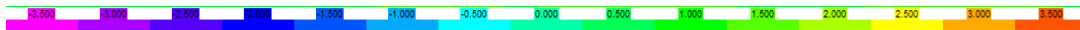
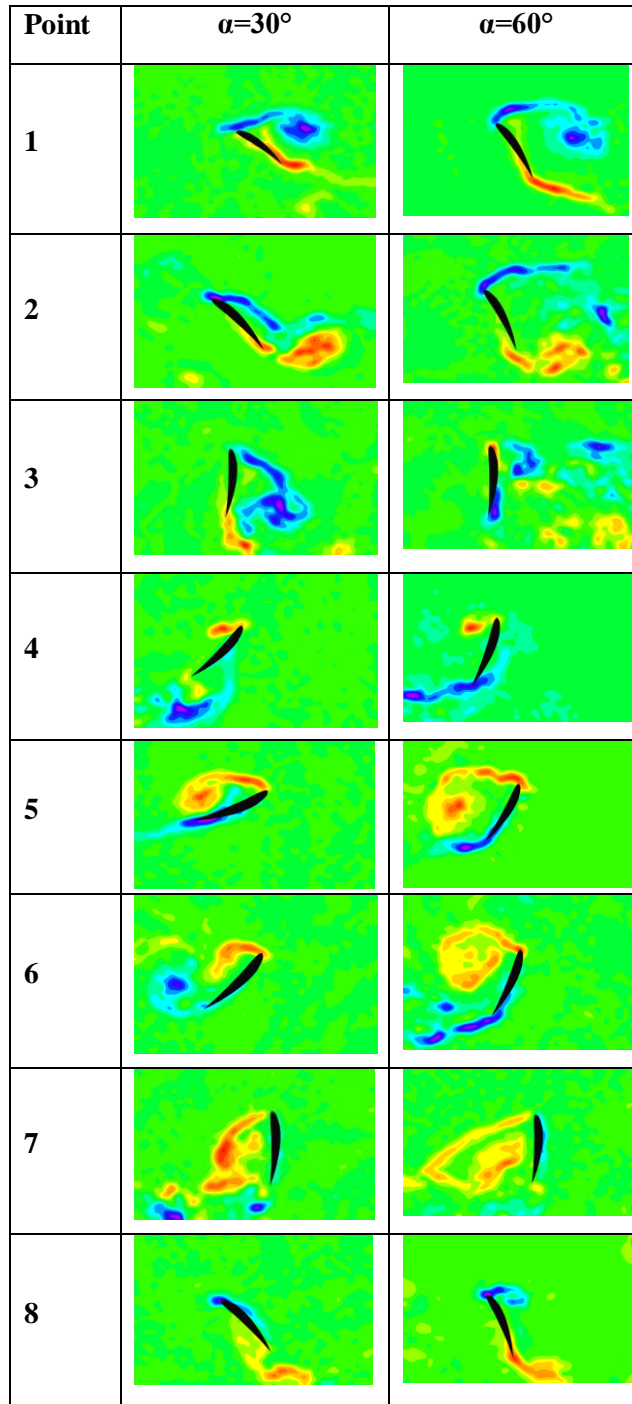


Fig 76 Instantaneous vorticity contours of NACA6412 during the 7th period for $\alpha=30^\circ$, $\alpha=60^\circ$ and $B=c$, $Re=1052$

CHAPTER 6

CONCLUSION

In this thesis, vortex shedding mechanism for flapping airfoil making the figure of eight motion in hover (no free stream velocity) is analyzed. In order to experience the vortex shedding mechanism from the leading and trailing edges of the airfoil experimentally, Particle Image Velocimetry (PIV) technique is used. For the experiments, a new flapping mechanism is designed and implemented to the existing water tank so that the path of the motion follows exactly the figure of eight. The experiments with different parameters which are the amplitude of the figure of eight flapping motion, the initial angle of attack and the shape of the airfoil are investigated by using this motion mechanism and the experimental set up. 96 experiments are performed and analyzed for this investigation. Also, the vortex shedding mechanism from the leading and trailing edges of the airfoil is also analyzed numerically.

Then, the experimental results are compared with previous and present numerical studies. Comparing the experimental results with the previous numerical results and the present experimental results, it is concluded that the results are similar. Hence, it can be said that the numerical results are validated with present experimental results.

First, the experimental results for NACA 0012 airfoil during the 7th period for $\alpha=30^\circ$, $B=c$, and $B=2c$ are compared and then the numerical results are compared with these experimental results to analyze the effects of amplitude of motion in y-direction. The comparison shows that larger vortical structures are formed in the case of $B=2c$ and more interactions of the leading and trailing edge vortices with the vortices generated in the previous stroke occur for $B=c$ when compared with $B=2c$ case. Therefore, it can be said that the vortices sustain their strength for a longer time period in the case of $B=2c$ when compared with the case of $B=c$. The results show also that the leading and trailing edge vortices are stronger which results in generation of higher lift. The comparison of the experimental and numerical results indicates that both methods indicates the same mechanism of formation of leading and trailing edge vortices.

The second parameter investigated in the experiments and in the numerical studies is the initial angle of attack of the airfoil. The results show that the lower initial angle of attack ($\alpha=30^\circ$) (higher rotational velocities) results in lower lift coefficients at the end of the rotational phase and higher values at the beginning of the rotational phase. The same investigation is performed for a cambered airfoil, NACA 6412. The results indicate further that the airfoil shape has no significant effect on the formation of the leading and the trailing edge vortices and the aerodynamic coefficients.

To summarize, from the results of the numerical and experimental studies, it can be concluded that the numerical results can be a dependable alternative to experiments since the results provided from the numerical and experimental results are similar.

As a future work, the lift and the drag forces acting on the airfoil in experiments can be measured by using load cells and this will be a major contribution to the research of unsteady lift and drag forces generated during the flapping motion. Further, since such force measurements employing load cells will be a continuous measurement, this will provide direct evidence for comparison with the numerically calculated forces.

3D PIV experiments can also be performed with the present system since it is a stereo PIV system. However for 3D measurements the model must be shorter in span and there should be no end plates. The results of 3D measurements can be compared with the experimental results obtained from 2D PIV experiments to investigate the effects of three dimensionality for the generation of lift and drag by flapping motion.

Another concept that needs to be investigated in the future is the aeroelastic behavior of the flapping wings. So far in all the experimental investigations performed in our laboratory we have considered only rigid wings and no elastic behavior was taken into consideration. However we know for sure that in actual life the flapping wings of birds and insects are flexible and possess aeroelastic behavior. During the flapping motion birds change the shape of their wings either by changing the camber distribution and/or the span length of their wings. Hence the wings of birds are subject to continuous morphing during flapping motion. Incorporation of a continuously morphing wing shape during flapping motion is an extremely difficult task to realize in these experiments. But it may be easier to include some elasticity for the wing structure and in the near future we may consider to perform some experiments with flexible wings.

Another concept that merits to be investigated in these experiments is the generation of thrust by flapping motion. Thus investigation of this concept requires the flying of the flapping wing in the medium. Therefore we must enlarge the tank and make it more appropriate for investigation of flying by flapping motion. This also requires the translation of the measurement system with the flying wing. Therefore this investigation needs a completely new test set-up.

REFERENCES

- [1] T.J. Mueller, “Aerodynamic Measurements at Low Reynolds Numbers for Fixed Wing Micro-Air Vehicles”, RTO AVT/VKI Special Course on Development and Operation of UAVs for Military and Civil Applications, 1999
- [2] Micro Air Vehicles toward a New Dimension in Flight, http://www.fas.org/irp/program/collect/docs/mav_auvsi.htm, Last accessed: 07.07.2013
- [3] William R. Davis, Jr., Bernard B. Kosicki, Don M. Boroson, and Daniel F. Kostishack, “Micro Air Vehicles for Optical Surveillance”, the Lincoln Laboratory Journal No:2, 1996
- [4] Anbarcı K., “Investigation of Flow Field around Flapping Wings”, M.Sc. thesis, ITU Aerospace Engineering Department, June 2007
- [5] An Introduction to MAVs (Miniature UAVs), The Development of MAVs, <http://www.draganfly.com/news/2008/08/26/an-introduction-to-mavs-miniature-uavs/>, Last accessed: 07.07.2013
- [6] MicroBat, <http://touch.caltech.edu/research/bat/bat.htm>, Last accessed: 07.07.2013
- [7] Shyy W., Lian Y., Tang J., Viiiru D., and Liu H., “Aerodynamics of Low Reynolds Number Flyers”, Cambridge University Press, 2008
- [8] Guerrero J., “Numerical Simulation of the Unsteady Aerodynamics of Flapping Flight”, PhD. Thesis, University of Genoa, Department of Civil, Environmental and Architectural Engineering, 2009
- [9] Kurtulus, D. F., Numerical and Experimental Analysis of Flapping Motion in Hover: Application to Micro Air Vehicle, Joint Ph.D thesis Poitiers University/ENSMA (Poitiers France) and METU (Ankara-Turkey), Poitiers, France, 17 June 2005
- [10] Başkan Ö., “Experimental and numerical investigation of flow field around flapping airfoils making figure-of-eight in hover”, M.Sc. thesis, METU Aerospace Engineering Department, September 2009.
- [11] Micro Micro flying robots can fly more effectively than flies, <http://phys.org/news168354449.html>, Last accessed: 27.06.2013
- [12] Breitenstein O., “Development of a Flapping Wing Mechanism.”, Autonomous Systems Lab (ASL) Swiss Federal Institute of Technology (ETH) Zurich, 2009
- [13] Yılmaz A., “Design and Development of Flapping Wing Micro Air Vehicle”, Autonomous Systems Lab (ASL) Swiss Federal Institute of Technology (ETH) Zurich, October 2009- April 2010

- [14] Codex on the Flight of Birds, http://en.wikipedia.org/wiki/Codex_on_the_Flight_of_Birds, Last accessed: 19.06.2013
- [15] “Il Codice Sol Volo Degli Uccelli”, Di Leonardo in Transfert a Mosca, Tra le Eccellenze del Made in Italy, <http://www.arte.it/notizie/italia/il-codice-sul-volo-degli-uccelli-di-leonardo-in-trasferta-a-mosca-tra-le-eccellenze-del-made-in-italy-8065>, Last accessed: 19.06.2013
- [16] Otto Lilienthal, <http://www.carnetdevol.org/Otto/gliding.html>, Last accessed: 19.06.2013
- [17] Wright Brothers, http://en.wikipedia.org/wiki/Wright_brothers, Last accessed: 19.06.2013
- [18] R. Katzmayr, “Effect of periodic changes of angles of attack on behavior of airfoils”, Technical Report No. 147, 1922
- [19] T. Theodorsen, “General theory of aerodynamic instability and the mechanism of flutter”, Technical Report No. 496, 1935
- [20] T. von Karman and J. Burgers, “General aerodynamic theory perfect fluids.”, *Aerodynamic Theory*, 2, 1935
- [21] R. Godoy-Diana, C. Marais, J. L. Aider & J. E. Wesfreid, “A model for the symmetry breaking of the reverse Bénard-von Kármán vortex street produced by a flapping foil.”, *Journal of Fluid Mechanics*, 622:23-32 (2009)
- [22] I. Garrick, “Propulsion of a flapping and oscillating airfoil.”, Technical report, NACA, Technical Report No. 567, 1936
- [23] A. Silverstein and U. Joyner. “Experimental verification of the theory of oscillating airfoils.”, Technical report, NACA, Technical Report No. 673, 1939
- [24] M. Lighthill, “Aquatic animal propulsion of high hydromechanical efficiency.”, *Journal of Fluid Mechanics*, 44:265-301, 1970
- [25] J. P. Giesing, “Nonlinear two-dimensional unsteady potential flow with lift.”, *Journal of Aircraft*, 5:135-143, 1968
- [26] Weis-Fogh, T. and Jensen, M., “Biology and physics of locust flight: I. Basic principles in insect flight: A critical review”, *Philosophical Transactions of the Royal Society of London, Series B* 239, 415–58, 1957
- [27] Desert Locust, <http://www.superstock.com/stock-photos-images/4201-81096>, Last accessed: 19.06.2013
- [28] J. Bratt., “Flow patterns in the wake of an oscillating airfoil.”, Technical report, Aeronautical Research Council, Report R2773, 1950
- [29] Maxworthy, T., “The Fluid Dynamics of Insect Flight.”, *Ann. Rev. Fluid. Mech.*, Vol. 13, pp. 329-350, 1981

- [30] Ellington, C. P., “The aerodynamics of hovering insect flight: I. The quasi-steady analysis”, *Philosophical Transactions of the Royal Society of London, Series B* 305, 1–15, 1984
- [31] Ellington, C. P., “Morphological parameters, II: The aerodynamics of hovering insect flight”, *Philosophical Transactions of the Royal Society of London, Series B* 305, 17–40, 1984
- [32] Ellington, C. P., “The aerodynamics of insect flight: III. Kinematics”, *Philosophical Transactions of the Royal Society of London, Series B* 305, 41–78, 1984
- [33] Ellington, C. P., “The aerodynamics of hovering insect flight: IV. Aerodynamic mechanisms”, *Philosophical Transactions of the Royal Society of London, Series B* 305, 79–113, 1984
- [34] Ellington, C. P., “The aerodynamics of hovering insect flight: V. A Vortex theory”, *Philosophical Transactions of the Royal Society of London, Series B* 305, 115–44, 1984
- [35] Ellington, C. P., “The aerodynamics of hovering insect flight: VI. Lift and Power Requirements”, *Philosophical Transactions of the Royal Society of London, Series B* 305, 145–181, 1984
- [36] Freymuth, P., “Thrust Generation by an Airfoil in Hover Modes.”, *Experiments in Fluids*, Vol. 9, pp. 17-24, 1990
- [37] Kurtuluş, F. D., “Unsteady Aerodynamics and Aeroelasticity Calculations of Flapping Motion for Micro Air Vehicle Applications”, EOARD Report 2, 2009
- [38] Dickinson, M.H. and Götz, K., “Unsteady Aerodynamic Performance of Model Wings at Low Reynolds Numbers”, *J. Exp. Biol.*, 174, pp.45-64, 1993
- [39] Dickinson, M.H., Lehmann, F.O. and Götz, K.G., “The active control of wing rotation by *Drosophila*”, *J. Exp. Biol.* 182, pp.173-189, 1993
- [40] Ellington, C. P., Van den Berg, C., Willmott, A. P., and Thomas, A. L. R., “Leading-edge vortices in insect flight”, *Nature (London)* 384, 626–30, 1996.
- [41] *Manduca sexta*, http://commons.wikipedia.org/wiki/File:Manduca_sexta_female, Last accessed: 19.06.2013
- [42] Van Den Berg, C. and Ellington, C.P., “The vortex wake of a ‘hovering’ model hawkmoth”, *Phil. Trans. R. Soc. Lond. B* 352, pp.317-328, 1997
- [43] Willmott, A.P. and Ellington, C.P., *The Mechanics of Flight in the Hawkmoth Manduca Sexta I. Kinematics of Hovering and Forward Flight*, *Exp. Biol.*, 200, pp.2705-2722, 1997
- [44] Willmott, A.P. and Ellington, C.P., *The Mechanics of Flight in the Hawkmoth Manduca Sexta II. Aerodynamic Consequences of Kinematic and Morphological Variation*, *Exp. Biol.*, 200, pp.2723-2745, 1997
- [45] Dickinson, M. H., Lehmann, F.-O., and Sane, S. P., “Wing rotation and the aerodynamic basis of insect flight”, *Science* 284, 1954–60, 1999

- [46] Drosophila M., <http://whyevolutionistrue.wordpress.com/2011/03/20/whos-related-to-fruit-flies/mwedrosophilamelanogaster00001/>, Last accessed: 19.06.2013
- [47] The Dickinson Lab in New Dress, <http://animalfightlab-lund.blogspot.com/2012/01/dickinson-lab-website-in-dress.html>, Last accessed: 19.06.2013
- [48] Birch, J. M. and Dickinson, M. H., Spanwise flow and the attachment of the leading-edge vortex on insect wings, *Nature (London)* 412, 729–33, 2001
- [49] Wang, Z. J., “Two Dimensional Mechanism for Insect Hovering”, *Physical Review Letters*, Vol. 85, No. 10, September 2000
- [50] Usherwood, J.R. and Ellington, C.P., “The Aerodynamics of revolving wings: I Model Hawkmoth wings”, *J. Exp. Biol.*, 205, pp.1547–1564, 2002
- [51] Sane, S. P. and Dickinson, M. H., “The aerodynamic effects of wing rotation and a revised quasi-steady model of flapping flight”, *Journal of Experimental Biology* 205, 1087– 96, 2002
- [52] Ramamurti, R. and Sandberg, W.C., “A three-dimensional computational study of the aerodynamic mechanisms of insect flight”, *J. Exp. Biol.*, 205, pp.1507-1518, 2002
- [53] Sun, M. and Tang, J., “Lift and power requirements of hovering flight in *Drosophila virilis*”, *J. Exp. Biol.*, 205, pp.2413-2427, 2002
- [54] Srygley, R. B. and Thomas, A. L. R., “Unconventional lift-generating mechanisms in free-flying butterflies”, *Nature (London)* 420, 660–4, 2002.
- [55] Per Farfalle... nella Valle, <http://valledellanava.wordpress.com/2007/11/30/per-farfalle-nella-valle-del-pegorino/>, Last accessed: 19.06.2013
- [56] Fry, S. N., Sayaman, R., and Dickinson, M. H., “The aerodynamics of free-flight maneuvers in *Drosophila*”, *Science* 300, 495–8, 2003
- [57] Wang, Z.J., Birch, J.M. and Dickinson, M.H., “Unsteady forces and flows in low Reynolds number hovering flight: two-dimensional computations vs. robotic wing experiments”, *J. Exp.Biol.*, 207, pp.449-460, 2004
- [58] Singh, B., Ramasamy, M., Chopra, I., and Leishman, G.J., “Experimental Studies on Insect-Based Flapping Wings for Micro Hovering Air Vehicles”. *AIAA*, Vol. 20742, 2004.
- [59] Birch, J.M., Dickson, W.B. and Dickinson, M.H., “Force production and flow structure of the leading edge vortex on flapping wings at high and low Reynolds numbers”, *J. Exp. Biol.*, 207, pp.1063-1072, 2004.
- [60] Wu, J.H. and Sun, M., “Unsteady aerodynamic forces of a flapping wing, *J. Exp. Biol.*, 207”, pp.1137-1150, 2004
- [61] Bomphrey ,R. J., Lawson, N. J., Harding, N.J. ,Taylor, G.K., and Thomas, A.L.R., “The aerodynamics of *Manduca sexta*: digital particle image velocimetry analysis

- of the leading-edge vortex”, *The Journal of Experimental Biology* 208, pp.1079-1094, 2005
- [62] Miller, L.A. and Peskin, C.S., “When vortices stick: an aerodynamic transition in tiny insect flight”, *J. Exp. Biol.*, 207, pp.3073-3088, 2004.
- [63] Miller, L.A. and Peskin, C.S., “A computational fluid dynamics of ‘clap and fling’ in the smallest insects”, *J. Exp. Biol.*, 208, pp.195-212, 2005
- [64] Warrick, D. R., Tobalske, B. W., and Powers, D. R., “Aerodynamics of the hovering hummingbird, *Nature (London)* 435”, 1094–7, 2005.
- [65] Hovering H., <http://www.flickr.com/photos/22904000@N07/7944360138/>, Last accessed: 19.06.2013
- [66] Lehmann, F.-O., Sane, S. P., and Dickinson, M. H., “The aerodynamic effects of wing–wing interaction in flapping insect wings”, *Journal of Experimental Biology* 208, 3075–92, 2005
- [67] Aono, H. and Liu, H., “Vortical Structures and Aerodynamics of Hawkmoth Hovering”, *Journal of Biomechanical Science and Engineering*, Vol. 1, No.1, pp.234-245, 2006
- [68] Sun, M. and Yu, X., “Aerodynamic force generation in hovering flight in a tiny insect”, *AIAA Journal*, Vol. 44, No.7, pp.1532-1540, 2006
- [69] Encarsia Formosa, <http://www.nuetzlinge.de/produkte/unter-glas/encarsia-formosa/>, Last accessed: 19.06.2013
- [70] Zuo, D., Peng, S., Chen, W. and Zhang, W., “Numerical simulation of flapping-wing insect hovering flight at unsteady flow”, *Int. J. Numer. Meth. Fluids*, 2006
- [71] <http://www.skyscrapercity.com>, Last accessed: 19.06.2013
- [72] Bos, F.M., Lentink, D., van Oudheusden, B.W: and biji, H., “Numerical study of kinematic wing models of hovering insect flight”, 45th AIAA Aerospace Sciences Meeting and Exhibit, 8-11 January 2007, Reno-Nevada
- [73] Lu, Y., Shen, G.X. and Su, W.H., “Flow visualization of dragonfly hovering via electromechanical model”, *AIAA Journal*, Vol.45, No.3, pp. 615-623, 2007
- [74] Lehmann, F.O., and Pick, S., “The Aerodynamic Benefit of Wing–Wing Interaction Depends on Stroke Trajectory in Flapping Insect Wings.”, *The Journal of Experimental Biology*, Vol. 210, pp.1362-1377, 2007
- [75] Guerrero J., “Numerical simulation of the Unsteady aerodynamics of flapping flight.”, Ph.D. Dissertation, Department of Civil, Environmental and Architectural Engineering University of Genoa, April 2009
- [76] Mazaheri K., and Ebrahimi A., “Experimental study on interaction of aerodynamics with flexible wings of flapping vehicles in hovering and cruise flight”, *Arch Appl Mech* (2010) 80: 1255–1269, 2008
- [77] Mueller D., Bruck H.A., and Gupta S.K., “Measurement of thrust and lift forces associated with drag of compliant flapping wing for micro air vehicles using a new test stand design”, *Experimental Mechanics* (2010) 50:725–735, 2008

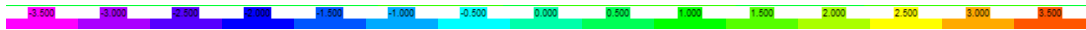
- [78] Sun W., Miao J., Tai C., Hung C., Hsu U., “Low reynolds number unsteady aerodynamic characteristics of flapping corrugated airfoil”, Seventh International Conference on CFD in the Minerals and Process Industries, 9-11 December 2009, Melbourne, Australia
- [79] Hu H., Clemons L., Igarashi H., “An experimental study of the unsteady vortex structures in the wake of a root-fixed flapping wing”, *Exp Fluids* (2011) 51:347–359, 2010
- [80] Erkmén N.O., Çekinmez A., Alemdaroğlu N., “Havada asılı konumda sekiz figürü (lemniskat) çizen çırpan kanat hareketinin aerodinamiğinin deneysel yöntemlerle incelenmesi”, IV. Ulusal Havacılık Ve Uzay Konferansı, 12-14 Eylül 2012, Hava Harp Okulu, İstanbul
- [81] Truong T.V., Le T.Q., Byun D., Park H.C., Kim M., “Flexible wing kinematics of a free-flying beetle (Rhinoceros Beetle *Trypoxylus Dichotomus*)”, *Journal of Bionic Engineering* 9 (2012) 177–184, 2012
- [82] <http://www.museum.osakafu-u.ac.jp/html/en/material/detail.php?id=213>, Last accessed: 20.06.2013
- [83] Jensen K. D., “Flow measurements”, 10th Brazilian Congress of Thermal Sciences and Engineering, November 29- December 03, 2004
- [84] Westerweel J., “Fundamentals of digital particle image Velocimetry”, *Meas. Sci. Technol.* 8 (1997) 1379–1392, 1997
- [85] Okçay M., and Öztekin U., “Educational Particle Image Velocimetry interactive experiment studies”, Meeting of the American Society of Engineering Education, 2008
- [86] FlowManager software and Introduction to PIV Instrumentation, Software’s User Guide
- [87] Seeding materials, <http://www.dantecdynamics.com/Default.aspx?ID=731>, Last accessed: 20.06.2013
- [88] S-HGS-10, <http://shop.dantecdynamics.com/product.asp?product=95>, Last accessed: 20.06.2013
- [89] Solo PIV Nd:YAG Laser System, Operator’s Manual, December 2003
- [90] HiSense 11M, 4M and MkII Cameras, Dantec Dynamics
- [91] Nikon 60mm f/2.8, <http://www.kenrockwell.com/nikon/60mm-afd.htm>, Last accessed: 20.06.2013
- [92] Measurement Principles of PIV, <http://www.dantecdynamics.com/Default.aspx?ID=1049>, Last accessed: 20.06.2013
- [93] Törnblom, O., “Introduction course in particle image velocimetry”, March 31, 2004
- [94] Bastiaans R.J.M., “Cross- correlation PIV; theory implementation and accuracy”, EUT Report 99-W-001

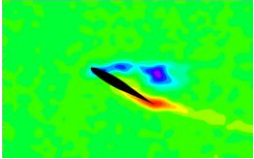
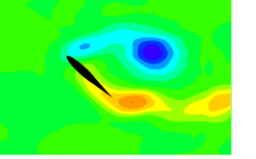
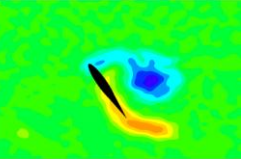
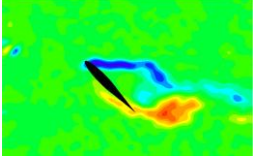
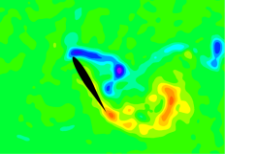
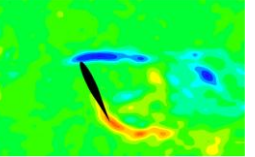
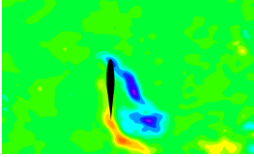
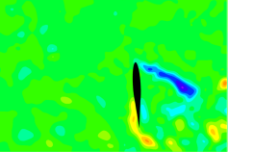
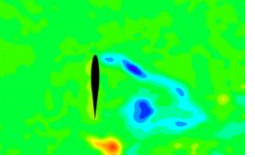
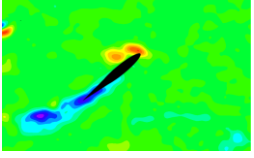
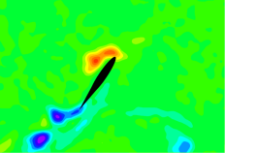
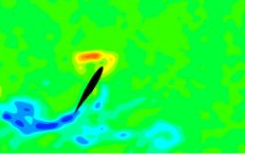
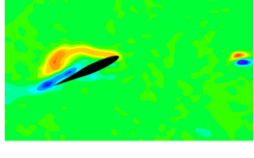
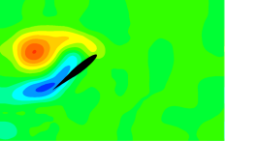
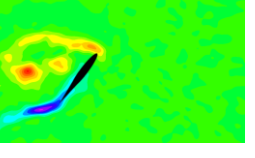
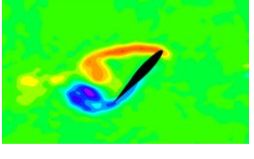
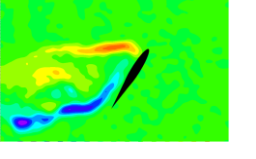
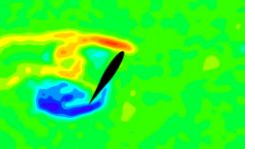
- [95] K.D. Jones and M.F. Platzer, “On the use of vortex flows for the propulsion of micro-Air and sea Vehicles.”, RTO-MP-069(I), 2001
- [96] Hızlı H., “Numerical and Experimental Investigation of Pitching/Plunging Airfoils in Hover”, M.Sc. thesis, METU Aerospace Engineering Department, December 2012.

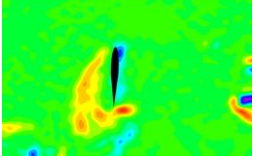
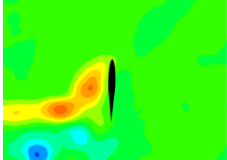
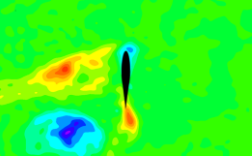
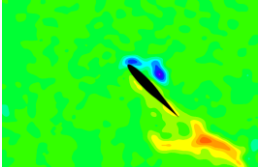
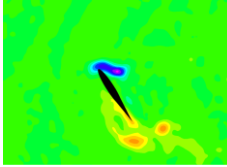
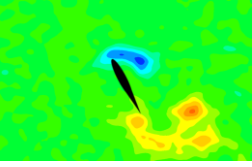
APPENDIX A

EXPERIMENTAL RESULTS

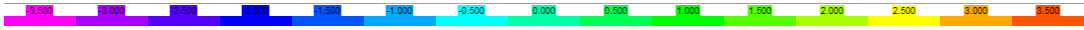
Instantaneous Vorticity Contours of NACA0012 during the 7th Period for $B=c$



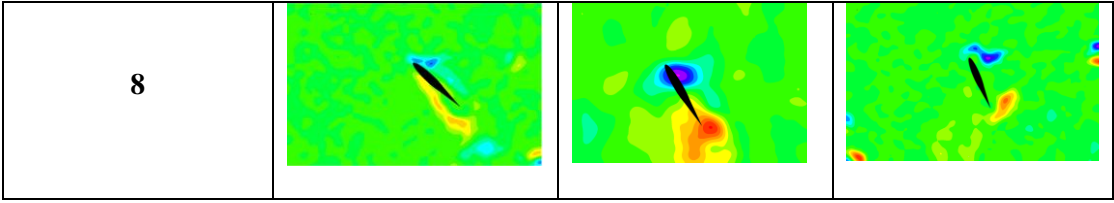
POINT	30B	45B	60B
1			
2			
3			
4			
5			
6			

7			
8			

Instantaneous Vorticity Contours of NACA0012 during the 7th Period for B=2c



POINT	30 2B	45 2B	60 2B
1			
2			
3			
4			
5			
6			
7			

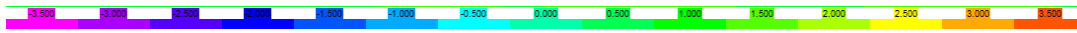


Instantaneous Vorticity Contours of NACA6412 during the 7th Period for $B=c$



POINT	30B	45B	60B
1			
2			
3			
4			
5			
6			
7			
8			

Instantaneous Vorticity Contours of NACA6412 during the 7th Period for B=2c

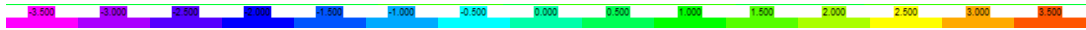


POINT	30 2B	45 2B	60 2B
1			
2			
3			
4			
5			
6			
7			
8			

APPENDIX B

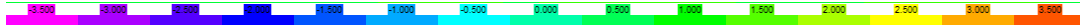
NUMERICAL RESULTS

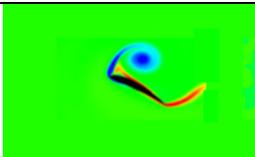
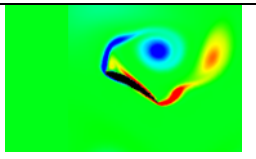
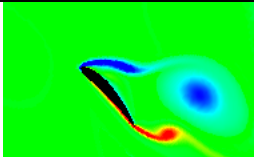
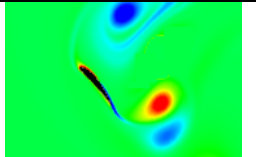
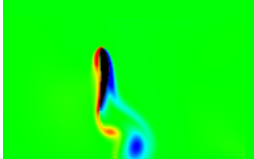
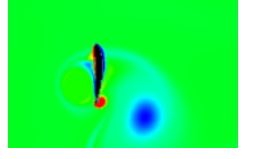
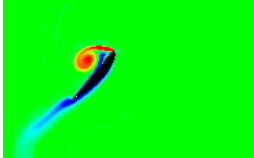
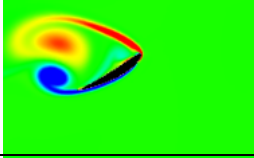
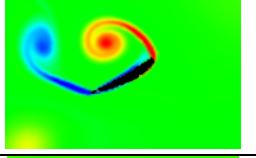
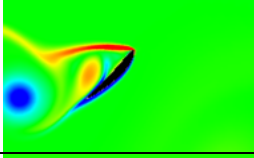
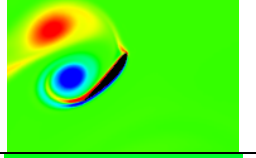
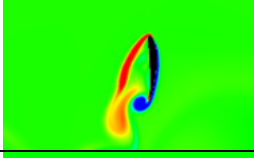
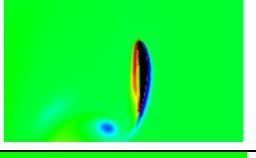
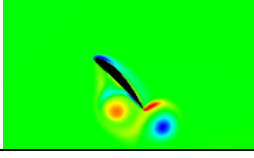
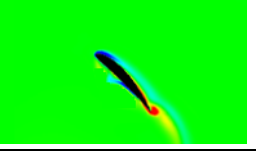
Instantaneous Vorticity Contours of NACA0012 during the 7th Period



POINT	30B	30 2B	60 B
1			
2			
3			
4			
5			
6			
7			
8			

Instantaneous Vorticity Contours of NACA6412 during the 7th Period



POINT	30 B	30 2B
1		
2		
3		
4		
5		
6		
7		
8		

APPENDIX C

NUMERICAL RESULTS PREVIOUSLY DONE [10]

Instantaneous vorticity contours of NACA 0012 during the 7th period for $\alpha=45^\circ$, $B=c$ & $B=2c$ and $Re=1052$

